**Title**
UNCOVERING SPATIAL AND TEMPORAL VARIABILITY IN THE PAST, PRESENT, AND FUTURE RESPONSE OF SOUTHERN CALIFORNIA'S WETLANDS TO ENVIRONMENTAL CHANGE



**Author**
Doughty, Cheryl

**Publication Date**
2020

Peer reviewed|Thesis/dissertation

UNIVERSITY OF CALIFORNIA

Los Angeles

# UNCOVERING SPATIAL AND TEMPORAL VARIABILITY IN THE PAST, PRESENT, AND FUTURE RESPONSE OF SOUTHERN CALIFORNIA'S WETLANDS TO ENVIRONMENTAL CHANGE

A dissertation submitted in partial satisfaction of the

requirements for the degree Doctor of Philosophy

in Geography

by

Cheryl Lynn Doughty

2020

ABSTRACT OF THE DISSERTATION

# UNCOVERING SPATIAL AND TEMPORAL VARIABILITY IN THE PAST, PRESENT, AND FUTURE RESPONSE OF SOUTHERN CALIFORNIA'S WETLANDS TO ENVIRONMENTAL CHANGE

by

Cheryl Lynn Doughty

Doctor of Philosophy in Geography

University of California, Los Angeles, 2020

Professor Kyle C. Cavanaugh, Chair

Climate change threatens the future of coastal wetlands, one of the most ecologically important, economically valuable ecosystems on earth. Changes to normal climatic and environmental conditions could throw off the delicate balance of these ecosystems with negative consequences to wetland biological response, productivity, and ultimately, resilience. Wetland response is controlled by biogeomorphic feedbacks relating plant productivity to environmental conditions, a complex interaction that can vary over space, within and among marshes, and over time, with tidal cycles and seasons. Wetland biomass serves as an important measure of spatially-explicit and temporally-variable changes that could ultimately impact wetland resiliency to climate change. Southern California's coastal wetlands are especially threatened by climate change due to other anthropogenic forces like coastal squeeze by urban development. The combination of threats

to these wetlands render them at-risk and call for improved understanding of how wetland response will vary across the region or within a given site as sea levels, precipitation, and temperatures change.

Remote sensing, fieldwork, and habitat response modeling approaches were combined to gain a holistic perspective of wetland vulnerability and resiliency at scales ranging from plant response to regional overviews of habitat change. This approach also spans temporal scales to investigate climate-related changes over time by predicting future impacts, capturing current, high-resolution patterns of biomass production, and uncovering decades of past patterns and drivers of wetland health. In chapter one, we develop a sea level rise (SLR) response model that addresses the scale-dependent factors controlling SLR response and accommodates different levels of data availability to improve regional predictions of SLR vulnerability. In chapters two and three, we test the application of Unmanned Aerial Vehicles (UAVs) in remotely estimating aboveground biomass in coastal saltmarshes and how such hyperspatial insights can aid in satellite-based approaches to biomass estimation. Lastly, chapter four reveals temporal patterns of productivity in salt marshes spanning the region, allowing us to determine the importance of regional versus local climatic controls on saltmarsh productivity. By quantifying impacts across time and space, we gain a better understanding of how climate change will determine the fate of wetlands throughout southern California.

The dissertation of Cheryl Lynn Doughty is approved

Richard Ambrose

Gregory Okin

Glen MacDonald

Kyle C. Cavanaugh, Committee Chair

University of California, Los Angeles

2020

**TABLE OF CONTENTS**

**LIST OF FIGURES ..... viii**

**LIST OF TABLES ..... xi**

**ACKNOWLEDGMENTS ..... xiii**

**INTRODUCTION ..... 1**

References ..... 7

**CHAPTER 1: Evaluating regional resiliency of coastal wetlands to sea level rise through hypsometry-based modeling ..... 9**

1.1 Abstract ..... 9

1.2 Introduction ..... 10

1.3 Materials and Methods ..... 14

1.4 Results ..... 24

1.5 Discussion ..... 32

1.6 Acknowledgements ..... 39

1.7 References ..... 40

1.8 Supplemental Materials ..... 45

**CHAPTER 2: Mapping Coastal Wetland Biomass from High Resolution Unmanned Aerial Vehicle (UAV) Imagery ..... 46**

2.1 Abstract ..... 46

2.2 Introduction ..... 47

2.3 Materials and Methods ..... 51

2.4 Results ..... 58

2.5 Discussion ..... 62

2.6 Conclusions ..... 67

2.7 Acknowledgements ..... 68

2.8 References ..... 69

2.9 Supplemental Materials ..... 76

**CHAPTER 3: Characterizing spatial variability in coastal wetland biomass across multiple scales using UAV and satellite imagery ..... 79**

3.1 Abstract ..... 79

3.2 Introduction ..... 80

3.3 Methods ..... 86

3.4 Results ..... 95

3.5 Discussion ..... 105

3.6 Acknowledgements ..... 111

3.7 References ..... 111

3.8 Supplemental Materials ..... 117

**CHAPTER 4: High local variability in coastal wetland response to macroclimatic drivers in a region exhibiting long term greening trends ..... 121**

4.1 Abstract ..... 121

4.2 Introduction ..... 121

4.3 Methods ..... 127

4.4 Results ..... 140

4.4.1 Long-term Greening Trends and Changing Environmental Conditions ..... 140

4.4.2 Variability in Intra-Annual NDVI Patterns Among Wetland Types ..... 142

4.4.3 Site-Based Correlations Show Spatial Variability in Key Drivers of Wetland NDVI .. 144

4.4.4 The Influence of Regional Controls on Wetland Greenness Vary in Space and Time .. 145

4.5 Discussion ..... 146

4.6 References ..... 150

4.7 Supplemental Materials ..... 157

**CONCLUSION ..... 160**

References ..... 161

**LIST OF FIGURES**

Figure 1-1. Conceptual diagram of the SLR response habitat change model. Model drivers (sea level rise, accretion, and mouth dynamics) represent the processes inducing change in water levels and elevation. Elevation change (ΔEt) raises the current marsh hypsometry (t0, light brown) to future hypsometry ((tx), dark brown). Water level changes (Δηt) alter the marsh zones (subtidal, mudflat, and vegetated marsh) delineated by elevation (horizontal lines). Habitat change is calculated as the difference in area under the curve for each marsh zone under current and future conditions. ..... 13
Figure 1-2. Archetype classification and projected percent difference in combined wetland habitat (vegetated marsh and unvegetated mudflat) for individual wetland sites for 1.7 m SLR (2100) in the southern California region. ..... 17
Figure 1-3. Current and predicted habitat change for wetland archetypes under two sea level rise scenarios when wetlands are confined to existing boundaries. ..... 27
Figure 1-4. Inter- and intra-archetype variability in percent difference in combined wetland habitat (vegetated marsh and unvegetated mudflat) predicted with 1.7 m SLR by 2100. Boxplots indicate the distribution of percent difference for each archetype including the median, first and third quartiles. Points indicate each site within the archetype class and the availability of accretion data for that site: data was either available from our literature review (measured, closed circle), extrapolated using the archetype framework (extrapolated, plus) or unavailable (none, open circle). For sites where accretion data was unavailable (small creeks and lagoons), estimates were made using a bathtub model assuming no accretion. ..... 29
Figure 1-5. Relationship between predicted percent difference in wetland habitat with 1.7 m SLR by 2100 and existing (2016) percent wetland areas (vegetated marsh and unvegetated mudflat) for all 105 sites. Site symbology reflects the archetype classification (color) and data availability of accretion inputs for that site (shape). Accretion data was either available from our literature review (closed circle, solid trendline), extrapolated using the archetype framework (plus, dashed trendline) or unavailable (open circle, long-dash trendline). For sites where accretion data was unavailable (small creeks and lagoons), estimates were made using a bathtub model assuming no accretion. ..... 30
Figure 1-6. Bookended range of the potential area for each wetland habitat when error is propagated through the model. Black lines represent the area of each habitat originally predicted by the model. Floating bars represent the range of possible values when model input errors are considered. ..... 31
Figure 1-7. Percent change in habitat area caused by sensitivity to model inputs. Percent change is calculated based on the area of each habitat (subtidal (light grey), unvegetated mudflat (grey), and vegetated marsh (dark grey)) originally predicted by the model. Sensitivity was analyzed by varying model parameters Accretion, Mouth Dynamics, SLR by ±50% and Initial Elevation by ±50 cm. Note varying y-axis scales in plot panels. ..... 32
Figure 2-1. The Carpinteria Salt Marsh Reserve located in Santa Barbara County, CA, USA. Landsat-8 (a) and UAV imagery (b) is shown in true color for a basin of the study site for comparison. Basemap is courtesy of ESRI. ..... 51
Figure 2-2. Overview of data collection and processing workflow. ..... 53
Figure 2-3. Reflectance validation of UAV reflectance using in situ canopy reflectance for (a) blue, (b) green, (c) red, (d) rededge and (e) NIR bands. ..... 57

Figure 2-4. Correlation between vegetation indices and dry aboveground biomass for the vegetation indices (a) CIgreen, (b) CIrededge, (c) EVI2, (d) GNDVI, (e) NDRE and (f) NDVI..... 59
Figure 2-5. Biomass maps based on NDVI biomass estimation model for (a) winter, (b) spring, (c) summer and (d) fall. ..... 60
Figure 2-6. Seasonal comparison of NDVI-based aboveground biomass by elevation for (a) winter, (b) spring, (c) summer and (d) fall. Pixel values (green circles) were extracted along an elevational gradient for vegetated wetland areas. Parabolic relationship shown in gray with standard error shaded light gray. ..... 61
Figure S2-1. Radiomatric performance of UAV orthomosaic (a) without and (b) with the inclusion of downwelling light sensor (DLS) data in image processing. Reflectance derived from UAV orthomosaics were compared to spectrometer reflectance of the vegetation canopy measured *in situ*. ..... 77
Figure 3-1. Conceptual hierarchy of factors related to wetland biomass in space and time. (A) Biological processes (green) occurring at fine scales give rise to patterns (blue) in wetland vegetation. The organizational levels at which processes and patterns manifest are labeled in italics. (B) Physical abiotic drivers (grey) influence biological processes and patterns across scales. Scale determines which factors can be remotely assessed using UAVs and Landsat (dashed lines)..... 81
Figure 3-2. Study site locations in southern California, USA with site symbology indicating wetland archetypes (A). Overviews of wetland areas and UAV survey areas (red outline) for (B) Carpinteria Salt Marsh Reserve, (C) San Dieguito Lagoon, (D) Los Peñasquitos Lagoon, and (E) Kendall-Frost Mission Bay Marsh Reserve. Gray basemap ©ESRI. Satellite imagery basemap ©Google..... 85
Figure 3-3. Overview of site sampling design, biomass sampling locations, elevation, true-color UAV imagery and modelled aboveground biomass maps for (A – C) Carpinteria Salt Marsh Reserve, (D – F) San Dieguito Lagoon, (G – I) Los Peñasquitos Lagoon, and (J – L) Kendall-Frost Mission Bay Marsh Reserve. ..... 90
Figure 3-4. Biophysical survey data on (A) species realized niches, (B) vegetation height and (C) aboveground biomass according to elevation. Dominant species reflect the highest percent cover within plots: Salicornia pacifica (Sp), Arthrocnemum subterminale (As), Jaumea carnosa (Jc), Salicornia bigelovii (Sb), Batis maritima (Bm), Frankenia salina (Fs), Distichlis littoralis (Dl), Distichlis spicata (Ds), Limonium californicum (Lc) and Spartina foliosa (Sf). ..... 95
Figure 3-5. Linear models between in situ aboveground biomass and NDVI derived from UAV imagery: (A) by site, Los Peñasquitos Lagoon (LPL, green squares), Carpinteria Salt Marsh Reserve (CSMR, orange circles), Kendall-Frost Mission Bay Marsh Reserve (KFMR, light blue triangles) and San Dieguito Lagoon (SDL, dark blue cross); and (B) by dominant cover classes, succulents (navy squares), grass-herbs (green circles), and soil (brown triangles). Linear model for all data is shown in grey..... 99
Figure 3-6. Correlations of aboveground biomass and NDVI when (A) in situ biomass is compared to NDVI derived from UAV imagery, (B) in situ aboveground biomass is compared to NDVI derived from Landsat imagery, and (C) modeled aboveground biomass (using models in panel (A)) is compared to NDVI derived from Landsat imagery. Symbology represents different sites: Los Peñasquitos Lagoon (LPL, green squares), Carpinteria Salt Marsh Reserve (CSMR, orange circles), Kendall-Frost Mission

Bay Marsh Reserve (KFMR, light blue triangles), and San Dieguito Lagoon (SDL, dark blue cross). ..... 102
Figure 3-7. Semivariograms showing the effect of image resolution on detectable variation in aboveground biomass for (A) Carpinteria Salt Marsh Reserve, (B) San Dieguito Lagoon, (C) Los Peñasquitos Lagoon, and (D) Kendall-Frost Mission Bay Marsh Reserve. Semivariance ($\gamma$(h)) for AGB presented as units in g2 m-4. ..... 103
Figure 3-8. True-color UAV imagery (6-cm resolution) showing spatial patterns in coastal wetland vegetation in relation to field sampling plots (red) and Landsat pixels (white) in the Carpinteria Salt Marsh Reserve. ..... 109
Figure S3-1. Profiles of aboveground biomass estimated from UAV (circles) and Landsat (squares) imagery along elevational transects (black lines) for (A) Carpinteria Salt Marsh Reserve, (B) San Dieguito Lagoon, (C) Los Peñasquitos Lagoon, and (D) Kendall-Frost Mission Bay Marsh Reserve. Profiles of AGB and elevation were extracted from within the same area designated as the elevational transects used in field sampling design and semivariogram analysis for each site. ..... 120
Figure 4-1. Monthly time series (1984 – 2019) of A) mean sea level for 5 regional NOAA Stations, B) mean stream discharge for 11 regional USGS gauges C) regional means of temperature (black) and precipitation (blue), D) regional means of drought indices, and E) regional means of climate indices. Note dual axes for temperature and precipitation data (C)..... 133
Figure 4-2. Long-term trends in NDVI of wetland sites in southern California. Trend direction (color) and magnitude (size) are indicated for significant trends. Nonsignificant trends are shown in gray. ..... 140
Figure 4-3. Time series of annual NDVI for focal wetland sites in southern California. Sites are ordered latitudinally from North to South. ..... 141
Figure 4-4. Trends related to site characteristics of A) latitude, B) size, C) archetype classification, D) habitat, E) percent area of watershed development, and F) number of restoration projects. Archetypes include Small Creeks and Lagoons (SCL), Intermediate Estuaries (IE), Large Lagoons (LL), Large River Valley Estuaries (LRVE), and Fragmented River Valley Estuaries (FRVE). ..... 142
Figure 4-5. Intra-annual NDVI patterns according to wetland archetypes and assigned k-means clusters. ..... 143
Figure 4-6. Top explanatory variables per site determined from univariate regression analyses. ..... 145
Figure S4-1. Sources of environmental datasets on NOAA sea levels (red diamonds) and USGS stream discharge (blue circles)..... 157
Figure S4-2. Average count of clear land pixels per year (mean ± standard deviation). Simple linear trends over the study period are shown in blue. Note that y-axis varies per panel. ..... 158
Figure S4-3. GTWR model selection based on A) corrected AIC and B) a stepwise procedure ranking model variable combinations (colors, symbols, combinations joined by lines) by AIC..... 159

**LIST OF TABLES**

Table 1-1. Data inputs required to inform and parameterize the SLR habitat change model..... 15
Table 1-2. Archetype accretion rates estimated from the literature review..... 18
Table 1-3. Mouth Dynamics Analysis results. Increased likelihood of high closure risk and the resultant increases in water levels when a system is presumed to be closed..... 25
Table 1-4. Predicted percent change in wetland (vegetated marsh and unvegetated mudflat) habitat area for the southern California region and individual wetland archetypes. ..... 26
Table S1-1. Records of published accretion data from the literature review. This supplemental info is provided as an excel file: ..... 45
Table S1-2. Example z* bin range upper limits corresponding to wetland habitats under current, 2050 and 2100 conditions. Changes to z* are determined by site-specific changes in water level estimated in our analysis. Example values shown for the Aliso Canyon estuary in San Diego county. Z* for this site is based on the Newport Beach, CA NOAA tidal station..... 45
Table 2-1. Broad band vegetation indices used in UAV remote sensing. ..... 56
Table 2-2. Aboveground biomass estimation equations for vegetation indices. ..... 58
Table 2-3. Seasonal NDVI-Aboveground biomass estimation equations. ..... 59
Table 2-4. Seasonal biomass estimates from field sampling and UAV biomass maps. ..... 61
Table S2-1. Site conditions and flight data for seasonal field surveys. ..... 76
Table S2-2. Live aboveground biomass estimation equations for vegetation indices. ..... 78
Table S2-3. Seasonal NDVI-Live aboveground biomass estimation equations. ..... 78
Table 3-1. Common species present in field biomass assessment plots (25 x 25 cm). Frequency provides the count of plots where each species was present. Mean percent cover is the average across all plots in which a species was present. ..... 87
Table 3-2. Mean height and aboveground biomass (± standard deviation) of dominant vegetation classes per site. Superscripts denote means differ significantly within each row ($P < 0.05$). ..... 96
Table 3-3. Linear models of aboveground biomass derived when (A) in situ biomass is compared to NDVI derived from UAV imagery, (B) in situ aboveground biomass is compared to NDVI derived from Landsat imagery, and (C) modeled aboveground biomass from UAV imagery is compared to NDVI derived from Landsat imagery. Site abbreviations: Los Peñasquitos Lagoon (LPL), Carpinteria Salt Marsh Reserve (CSMR), Kendall-Frost Mission Bay Marsh Reserve (KFMR), and San Dieguito Lagoon (SDL). ..... 100
Table S3-1. Descriptions of remote sensing data and tidal levels during acquisition ..... 117
Table S3-2. Linear models of aboveground biomass for all UAV vegetation indices per site (A – D) and for all sites combined (E). Vegetation indices selected based on band combinations possible for UAV or Landsat imagery. ..... 118
Table S3-3. Linear models of aboveground biomass for vegetation types and archetypes based on UAV imagery..... 119
Table 4-1. Regional summary of environmental conditions over the 1984 – 2019 study period. ..... 135
Table 4-2. Spearman's ranked correlation coefficients among environmental data. Bold numbers indicate significance levels of $p < 0.05$..... 137
Table 4-3. Geographically weighted local summary statistics for environmental variables used in Geographically and Temporally Weighted Regression (GTWR)..... 139

Table 4-4. Comparison of multivariate models used to explain NDVI using geographically and temporally weighted regression (GTWR)..... 146

## ACKNOWLEDGMENTS

The work conducted for this dissertation was partly funded by grants from the U.S. Fish and Wildlife Service Landscape Conservation Cooperative (LCC) Program, the California State Coastal Conservancy, the USC Sea Grant Trainee Program, and the NASA New Investigator Program (NNX16AN04G). During the course of this work, I was also supported by UCLA's Graduate Research Mentorship Award and Summer Graduate Research Mentorship Awards. Other awards from the Wetland Foundation 2018 Travel Grant and the Santa Monica Bay Audubon Society Field Study Grant provided additional funding for conference travel and fieldwork.

Thank you to my advisor, Kyle Cavanaugh, for introducing me into the world of remote sensing and giving me another toolset for investigating important ecological questions in what I would argue are some of the world's coolest ecosystems. Thank you for giving me both support and independence throughout this process, a delicate balance that helped me grow as a researcher in many ways. You lead by great example in your science, your writing, and your mentoring.

I am very grateful to my other committee members for their wide range of perspectives and expertise that contributed to this dissertation. To Glen MacDonald, whose work on climate change on geologic time scales reminds me that the world existed long before the advent of Landsat. To Gregory Okin, for your expertise in remote sensing and for showing me that scale is also an important consideration in understanding the science behind remote sensing and building a UAV from scratch. To Richard Ambrose, who threw me right into the deep end with the opportunity to work with and learn directly from regional experts like him working to save southern California's wetlands.

I would like to thank Eric Stein for his mentorship during the first years of my dissertation working as a USC Sea Grant Trainee on the Southern California Wetlands Recovery Project. I learned so many valuables lessons on working with a coordinated regional management effort.

Thank you to the other scientists that have guided my way, especially Andrea Quattrini, Samantha Chapman, and Candy Feller. And to all those who helped me in the field, in the lab, and in the department.

My personal thank you's must begin with my parents, David and Mary. Having your support throughout my life has given me the privilege to follow my dreams and the opportunities presented to me along the way. Mom and Dad, you instilled in me both a love of plants and seeing the world from above. I'll forever cherish early Springs with mom in the greenhouse and days flying in gliders with dad. Clearly, you've both had a tremendous impact on my research interests. To my sisters, Diane and Chrissy, who turned the outside world into a schoolroom where the only required texts were Golden Guides on ants, bees, and clouds. And to everyone who has joined the family tree since those days.

Lastly, to Mike, for making the coffee 90% of the time and for being there every day to help me keep perspective of what really matters in life. I wouldn't have made it without you.

# VITA

## *Education*

**PhD in Geography,** University of California, Los Angeles, CA — Expected 2020
Committee: Dr. Kyle Cavanaugh (chair), Dr. Richard Ambrose, Dr. Glen MacDonald, and Dr. Gregory Okin

**MS in Biology,** Villanova University, Villanova, PA — 2015

**BS in Biology with Distinction and Honors**, Temple University, Philadelphia, PA — 2012

## *Awards and Fellowships*

| | |
|---|---|
| NASA Postdoctoral Program Fellowship | 2020 |
| Graduate Summer Research Mentorship Award, *UCLA* | 2018, 2016 |
| The Wetland Foundation 2018 Travel Grant | 2018 |
| Santa Monica Bay Audubon Society Field Study Grant | 2017 |
| Graduate Research Mentorship Award, *UCLA* | 2017 – 2018 |
| Student Travel Award, *Coastal and Estuarine Research Federation* | 2015 |
| USC Sea Grant Traineeship, *University of Southern California, Dornsife* | 2015 – 2017 |
| Link Fellowship, *Smithsonian Institution* | 2014 |
| Rachel Carson Memorial Award, *Temple University* | 2012 |

## *Outreach*

- "Bolsa Chica Site Exemplifies Need to Protect California's Wetlands." Spectrum 1 News, Christopher Gee.
- "New hope for Southern California's besieged wetlands." UCLA Newsroom, David Colgan.
- "Walking trees terrorize marshes." Hakai Magazine, Asher Elbein.
- "Could mangrove northern expansion temper global warming?" Florida Today, Jim Wayner.

## *Publications*

**Doughty, CL** , RF Ambrose, GS Okin, and KC Cavanaugh. (*Submitted to Remote Sensing in Ecology and Conservation*). Characterizing spatial variability in coastal wetland biomass across multiple scales using UAV and satellite imagery.

Stein, ED, **CL Doughty**, J Lowe, M Cooper, E Borgnis Sloane, and DL Bram. 2020. Establishing Targets for Regional Coastal Wetland Restoration Planning Using Historical Ecology and Future Scenario Analysis: The Past, Present, Future Approach. *Estuaries and Coasts*. DOI: 10.1007/s12237-019-00681-4

Cavanaugh, KC, EM Dangremond, **CL Doughty**, AP Williams, JD Parker, MA Hayes, W Rodriguez, and IC Feller. 2019. Climate-driven regime shifts in a mangrove–salt marsh ecotone over the past 250 years. *Proc. Natl. Acad. Sci. U. S. A.* 116: 21602–21608. DOI: 10.1073/pnas.1902181116

**Doughty, CL** and KC Cavanaugh. 2019. Mapping coastal wetland biomass from high resolution unmanned aerial vehicle (UAV) imagery. *Remote Sensing* 11(5): 540. DOI: 10.3390/rs11050540 *Special Issue Satellite-Based Wetland Observation

**Doughty, CL**, 2019. Batch processing Micasense images to reflectance (batch-imageprocessing), GitHub repository: github.com/cldoughty/batch-imageprocessing

**Doughty, CL**, KC Cavanaugh, RF Ambrose, and ED Stein. 2018. Evaluating regional resiliency of coastal wetlands to sea level rise through hypsometry-based modeling. *Global Change Biology* 25(1):78-92. DOI: 10.1111/gcb.14429.

**Doughty, CL**, 2018. Southern California Wetlands Recovery Project Regional Strategy Update - Sea Level Rise Model (scwrp-rsu-slr-model), GitHub repository: github.com/cldoughty/scwrp-rsu-slr-model

Southern California Wetlands Recovery Project. 2018. Wetlands on the Edge: The Future of Southern California's Wetlands: Regional Strategy 2018. Prepared by the California State Coastal Conservancy, Oakland, Ca.

**Doughty, CL**, KC Cavanaugh, CR Hall, IC Feller, and SK Chapman. 2017. Impacts of mangrove encroachment and mosquito impoundment management on coastal protection services. *Hydrobiologia* 803(1):105–120. DOI: 10.1007/s10750-017-3225-0

Kelleway, JJ, KC Cavanaugh, K Rogers, IC Feller, E Ens, **CL Doughty**, and N Saintilan. 2017. Review of the ecosystem service implications of mangrove encroachment into salt marshes. *Global Change Biology* 23:3967–3983. DOI: 10.1111/gcb.13727

**Doughty, CL**, JA Langley, WS Walker, IC Feller, R Schaub, and SK Chapman. 2016. Mangrove range expansion rapidly increases wetland carbon storage. *Estuaries and Coasts* 39:385–396. DOI: 10.1007/s12237-015-9993-8

**Doughty, CL**. 2015. Carbon storage and coastal protection: Uncovering the potential impacts of mangrove range expansion. MS Thesis, Villanova University. ProQuest (UMI 1587224).

Chapman, SK, H Tran, and **CL Doughty**. 2014. Climate adaptation at Kennedy Space Center: How Can Wetlands Help NASA Adapt to Warming Temperature and Rising Seas? *Wetland Science and Practice* 31(2): 6-8.

**Doughty, CL**, AM Quattrini, and EE Cordes. 2014. Insights into the population dynamics of the deep-sea coral genus *Paramuricea* in the Gulf of Mexico. *Deep Sea Research Part II: Topical Studies in Oceanography* 99 (0):71-82. DOI: 10.1016/j.dsr2.2013.05.023

Quattrini, AM, PJ Etnoyer, **CL Doughty**, L English, R Falco, N Remon, M Rittinghouse and EE Cordes. 2014. A phylogenetic approach to octocoral community structure in the deep Gulf of Mexico. *Deep Sea Research Part II: Topical Studies in Oceanography* 99 (0):92-102. DOI: 10.1016/j.dsr2.2013.05.027

## INTRODUCTION

The dynamic nature of coastal wetlands has long been recognized as a cornerstone trait of the world's economically valuable and ecologically important ecosystems (Barbier et al. 2011). Coastal ecosystems, such as salt marshes and mangrove forests, occupy ~70% of the worlds coastlines and support 10.9% of the world's population in low-elevation coastal zones (Neumann et al. 2015; McOwen et al. 2017; Bunting et al. 2018) with many services and benefits including water filtration, storm protection, recreation, and carbon storage (Zedler and Kercher 2005). Situated at the interface of land and sea, coastal wetlands are well-adapted to high environmental variability caused by both oceanic and terrestrial forces. Coastal wetlands have persisted for millennia through changes in past climatic conditions and sea levels (Jones and Mann 2004; Kemp et al. 2011; Fagherazzi 2013). Yet in the Anthropocene, the fate of coastal wetlands will not only be determined by their ability to react dynamically to the surrounding environment, but also to climate change and other direct human impacts (Kirwan and Megonigal 2013).

Climate change has already affected coastal wetlands worldwide (Wong et al. 2014) and impacts are predicted to worsen in coming decades (Scavia et al. 2002; Church et al. 2013). Globally, temperatures will increase 2 – 6°C by the end of the century (Coumou et al. 2013), while precipitation events may become more intense (Trenberth 2011), and extreme events like storm surges and coastal flooding may also worsen (Mitchell et al. 2006). Sea levels are projected to rise anywhere from 0.26 – 0.82 m globally depending on Representative Concentration Pathway (RCP) scenarios of increasing atmospheric $CO_2$ concentrations (Church et al. 2013; IPCC 2013). Although a future of global climate change is certain, the impacts of these global drivers to wetlands will be highly variable, as changes in temperature, precipitation, and sea level, will be locally and regionally variable (Muller and O'Gorman 2011; Gregory et al. 2013). Therefore,

uncertainty also plays a key role in the threat of climate change, which will inevitably disrupt and alter the normal climatic and environmental conditions that have direct impacts to coastal wetlands.

Wetland response to climate change will be spatially and temporally variable, but emerging evidence suggests that changes to environmental drivers like temperature, rainfall, CO2 concentration, sea levels, and extreme events will have cascading effects on wetland plant productivity, biomass, health, and resilience (Langley et al. 2009; Mckee et al. 2012; Kirwan and Megonigal 2013; Osland et al. 2016). For example, in response to rising seas wetlands can migrate laterally or vertically, the first depending on available upland migration space, and the second determined by accretion and elevation capital (Schuerch et al. 2018; Cahoon et al. 2019; Fagherazzi et al. 2020). These two generalized types of response, however, are founded on complex biogeomorphic feedbacks that exist between marsh vegetation and their surrounding environment. Biogeomorphic feedbacks describe how wetland macroflora bioengineer surrounding elevations to optimize productivity in relation to physical factors like inundation levels, nutrients, and soil salinity that are often correlated with elevation (Pennings et al. 2005; Traut 2005; Morris 2007; Moffett et al. 2012). By optimizing productivity, wetland plants are able to allocate aboveground and belowground biomass, which directly contributes to vertical accretion of soil organic matter through the decomposition of roots and detritus, and also indirectly by trapping inorganic sediments (Morris et al. 2002; Duarte et al. 2013). Net productivity in coastal wetlands represents the generation of plant biomass as the result of these complex interaction with the surrounding environment. Ultimately, plants and associated biological processes are important controls to wetland resilience (Cahoon et al. 2020). However, these biological plant-environment

feedbacks are variable in space, among species and along environmental gradients, and in time, with daily and seasonal fluctuations in sea levels, temperature, and precipitation.

The complex biogeomorphic feedbacks that allow coastal wetland plants to remain productive will likely be altered or disrupted as environmental conditions change. The full extent of impacts from warming temperatures, rising seas, altered precipitation patterns, and intensifying extreme events remains to be seen (Osland et al. 2016), and the consequences to bioproductivity will be highly variable among wetland sites, zones and species (Boesch et al. 2000; Scavia et al. 2002; Janousek et al. 2016). Temperature and precipitation have documented mixed linear and nonlinear impacts to wetland vegetation height, biomass, productivity, decomposition, soil carbon density, and soil carbon accumulation (Feher et al. 2017). Spatially-explicit and temporally-variable changes to productivity could ultimately impact wetland resiliency to climate change by altering plant productivity and biomass (Fagherazzi et al. 2012; Kirwan and Megonigal 2013). Therefore, biomass may serve as an important indicator of the complex, fine-scale interactions occurring within wetlands that will determine overall response to environmental changes (Kirwan et al. 2016). Possible negative outcomes of changing environmental conditions on coastal wetlands can range from widespread wetland loss, local diebacks, to disruptions in annual phenological patterns and reductions in productivity (Mckee et al. 2012; Buffington et al. 2018).

In order to preserve these valuable systems into the future, coastal management and adaptation efforts need a holistic perspective that accounts for spatial and temporal variability in both drivers and response across scales. Coordinated regional efforts are essential for developing a landscape-level understanding of current baselines and future impacts (Zedler 1996; Zedler and Callaway 1999). This is important as coastal wetlands also face direct and indirect human impacts like urban development, conversion from agriculture, coastal squeeze, altered freshwater inputs,

and eutrophication that will need to be managed to improve resiliency (Kennish 2001). Successful regional strategies must account for wetland ecology and dynamism (Boesch 2006; Armitage 2014), and be designed based on understanding of past, present, and future conditions (Stein et al. 2019). Ideally, regional efforts must reflect the sum of the parts, i.e., all wetlands must be accounted for and site-based management efforts must be conducted in light of the regional context (Simenstad et al. 2006). Fortunately, restoration efforts can be guided by the increasing amounts of publicly available data that can help inform past, present, and future conditions of coastal wetlands across spatial scales in a region.

Many of the impacts to coastal wetlands can be observed using remote sensing. Remotely sensed imagery of the Earth's surface has been useful in many wetland applications including mapping distributions, classifying habitats, estimating biomass and carbon storage, and valuing ecosystem services (Silva et al. 2008; Kuenzer et al. 2011; Klemas 2013b; De Araujo Barbosa et al. 2015; Klemas 2015a; Mahdavi et al. 2018). Data used in these wide-ranging applications can be acquired through several different types of platforms and sensors. Satellite remote sensing offers repeat, coverage of the globe suitable for investigating large geographic areas or monitoring changes through time (Ozesmi and Bauer 2002; Pettorelli et al. 2014). Landsat satellite imagery is often used for ecosystem monitoring because it provides the longest running archive of continuous global data (Pasquarella et al. 2016). Manned aircraft have also been used to collect data at regional and subregional scales and at temporal scales appropriate for capturing the dynamic responses in wetlands, although this option can be costly (Klemas 2013a). More recently, unmanned aerial vehicles (UAVs) have been recognized as valuable tools for site-based applications due to their relatively low cost, and great flexibility in spatial and temporal data resolutions, and customization of payload sensors (Hugenholtz 2012; Anderson and Gaston 2013;

Whitehead et al. 2014a; Whitehead et al. 2014b; Klemas 2015b; Manfreda et al. 2018). In addition to these platforms, many types of sensors exist that can passively or actively acquire different data types, ranging from multispectral and hyperspectral optical imagery to radar and Light Detection and Ranging (LiDAR) data (Schmidt and Skidmore 2003; Adam et al. 2010; Guo et al. 2017). Care must be taken in selecting the appropriate data for coastal wetlands applications (Gallant 2015), as there are tradeoffs among the spatial, temporal, and spectral resolutions of remotely sensed data that determine what ecological properties can be observed (Kennedy et al. 2014).

Remote sensing provides an approach for estimating wetland characteristics specifically related to productivity and biomass that may inform resiliency to climate change across spatial and temporal scales. Biophysical and biochemical properties of vegetation measured via remote sensing are important indicators of plant productivity (Hardisky et al. 1984; Hardisky et al. 1986; Klemas 2013b). Using vegetation indices to summarize the reflective properties of wetland plants is key to inferring the state of wetland systems from optical imagery (Mutanga and Skidmore 2004; Mishra and Ghosh 2015; Xue and Su 2017). Commonly used indices like the normalized difference vegetation index (NDVI; Rouse et al. 1974), tasseled cap greenness (TCG; Kauth and Thomas 1976), and enhanced vegetation index (EVI; Jiang et al. 2008) can assess wetland health across a range of scales, from biophysical plant properties to large-scale ecosystem change (Adam et al. 2010; Xue and Su 2017). Examples capitalizing on the information that can be gleaned from remotely sensed data include estimations of biomass and carbon storage (Klemas 2013b; Byrd et al. 2014; Byrd et al. 2018; Mo et al. 2018) and identification of patterns and drivers of wetland biomass, health, phenology, and overall greenness in both salt marsh and mangrove wetlands (Kearney et al. 2002; Mo et al. 2015; O'Donnell and Schalles 2016; Brooke et al. 2017; Wu et al. 2017; Buffington et al. 2018; Cavanaugh et al. 2018; Mo et al. 2019). NDVI in particular has been

useful in assessing ecological response to environmental change (Pettorelli et al. 2005). From these examples, it is clear that the data derived from remote sensed imagery can offer insights into the status of wetland distributions, greenness, biomass, productivity, and health. Time series of remotely sensed data could further inform a more synoptic understanding of coastal wetland ecology (Shanmugam 2013) and provide an invaluable view of ecological patterns and processes over space and time (Kennedy et al. 2014).

In southern California, climate change and other globally relevant anthropogenic forces threaten coastal wetlands and warrant investigations into past response, current conditions, and future resiliency. The southern California region ranges from Point Conception to the US-Mexico border and is home to a diverse network of coastal and estuarine wetlands that range in size, setting, ecology and wetland type, or archetype (SCWRP 2018). Almost 48% of coastal wetlands in this region have been lost since ca. 1850 to habitat conversion (Stein et al. 2014; Stein et al. 2019). The remaining wetlands are remnants of larger historical wetlands, reduced in size and constrained by human development (Zedler 1982; Grossinger et al. 2011; Stein et al. 2014; Stein et al. 2019). Wetlands experiencing such "coastal squeeze", or a lack of migration space due to ocean encroachment against the human-built environment (Pontee 2013), are especially vulnerable to climate change impacts (Torio and Chmura 2013; Borchert et al. 2018). The combined threats to southern California wetlands render them at-risk and call for improved understanding of how wetland response will vary across the region or within a given site as sea levels, precipitation, and temperatures change. Ultimately, our understanding of how vulnerable, or resilient, wetlands in this region may be to climate change requires consideration of the spatial and temporal variability of drivers and impacts across a large, diverse region.

The overarching goal of this work is to uncover spatial and temporal patterns and variability in the past response of wetlands to environmental change, in the current state of wetland biomass, an important link to resilience, and in the future predictions of climate change impacts across the southern California region. In the following chapters, I rely on fieldwork for insights straight from the wetland plants, UAV remote sensing for detailed, bird's-eye views of individual wetlands, the Landsat archive for decades of satellite images across a large geographic region, and many other publicly available datasets. In chapter 1, I predict future regional losses in wetland habitats by developing a SLR response model that is suitable for large geographic regions containing diverse wetland types. This effort directly informed regional management strategies (SCWRP, 2018), but also highlighted data and knowledge gaps in our understanding of future response of wetlands to climate change in southern California. Chapters 2 and 3 aim to fill some of these gaps, by using UAVs to map seasonal and spatial patterns in aboveground biomass and comparing this method of remote biomass estimation against Landsat imagery for a few select sites in the region. These chapters provide valuable insights into how the scale of remotely sensed imagery can influence the detection of patterns and variability of wetland aboveground biomass. Chapter 4 uncovers decades of past patterns in wetland greenness and identifies correlations with changing environmental condition. Together, these chapters use insights from the past, present, and future to gain a holistic regional perspective of wetland vulnerability and resiliency to climate change.

**References**

Barbier, Edward B, Sally D Hacker, Chris J Kennedy, Evamaria W Koch, Adrian C Stier, and Brian R Silliman. 2011. The value of estuarine and coastal ecosystem services. *Ecological Monographs* 81: 169–193.

Barnes, Em, TR Clarke, Se Richards, PD Colaizzi, J Haberland, M Kostrzewski, P Waller, et al. 2000. Coincident detection of crop water stress, nitrogen status and canopy density using ground-based multispectral data. In *Proceedings of the Fifth International Conference on*

*Precision Agriculture, Bloomington, MN, USA. Vol. 1619. 2000.*

Doughty, Cheryl, and Kyle Cavanaugh. 2019. Mapping Coastal Wetland Biomass from High Resolution Unmanned Aerial Vehicle (UAV) Imagery. *Remote Sensing* 11: 540. https://doi.org/10.3390/rs11050540.

Doughty, Cheryl L., Richard F. Ambrose, Gregory S. Okin, and Kyle C. Cavanaugh. Characterizing spatial variability in coastal wetland biomass across multiple scales using UAV and satellite imagery. *Remote Sensing in Ecology and Conservation*.

Doughty, Cheryl L., Kyle C. Cavanaugh, Richard F. Ambrose, and Eric D. Stein. 2019. Evaluating regional resiliency of coastal wetlands to sea level rise through hypsometry-based modeling. *Global Change Biology* 25: 78–92. https://doi.org/10.1111/gcb.14429.

Gitelson, Anatoly A., Yoram J. Kaufman, and Mark N. Merzlyak. 1996. Use of a green channel in remote sensing of global vegetation from EOS-MODIS. *Remote Sensing of Environment* 58. Elsevier: 289–298. https://doi.org/10.1016/S0034-4257(96)00072-7.

Gitelson, Anatoly A., Mark N. Merzlyak, and Hartmut K. Lichtenthaler. 1996. Detection of Red Edge Position and Chlorophyll Content by Reflectance Measurements Near 700 nm. *Journal of Plant Physiology* 148. Urban & Fischer: 501–508. https://doi.org/10.1016/S0176-1617(96)80285-9.

Gitelson, Anatoly A., Andrés Viña, Verónica Ciganda, Donald C. Rundquist, and Timothy J. Arkebauer. 2005. Remote estimation of canopy chlorophyll content in crops. *Geophysical Research Letters* 32. John Wiley & Sons, Ltd: L08403. https://doi.org/10.1029/2005GL022688.

Jiang, Zhangyan, Alfredo R. Huete, Kamel Didan, and Tomoaki Miura. 2008. Development of a two-band enhanced vegetation index without a blue band. *Remote Sensing of Environment* 112. Elsevier: 3833–3845. https://doi.org/10.1016/J.RSE.2008.06.006.

Rouse, JW, RH Haas, JA Schell, and DW Deering. 1974. Monitoring vegetation systems in the Great Plains with ERTS. *NASA Spec. Publ.*: 351, 309.

Spencer, Thomas, Mark Schürch, Robert J. Nicholls, Jochen Hinkel, Daniel Lincke, A.T. T. Vafeidis, Ruth Reef, et al. 2016. Global coastal wetland change under sea-level rise and related stresses: The DIVA Wetland Change Model. *Global and Planetary Change* 139. Elsevier B.V.: 15–30. https://doi.org/10.1016/j.gloplacha.2015.12.018.

# CHAPTER 1: Evaluating regional resiliency of coastal wetlands to sea level rise through hypsometry-based modeling[1]

## 1.1 Abstract

Sea level rise (SLR) threatens coastal wetlands worldwide, yet the fate of individual wetlands will vary based on local topography, wetland morphology, sediment dynamics, hydrologic processes, and plant-mediated feedbacks. Local variability in these factors makes it difficult to predict SLR effects across wetlands or to develop a holistic regional perspective on SLR response for a diversity of wetland types. To improve regional predictions of SLR impacts to coastal wetlands, we developed a model that addresses the scale-dependent factors controlling SLR response and accommodates different levels of data availability. The model quantifies SLR-driven habitat conversion within wetlands across a region by predicting changes in individual wetland hypsometry. This standardized approach can be applied to all wetlands in a region regardless of data availability, making it ideal for modeling SLR response across a range of scales. Our model was applied to 105 wetlands in southern California that spanned a broad range of typology and data availability. Our findings suggest that if wetlands are confined to their current extents, the region will lose 12% of marsh habitats (vegetated marsh and unvegetated flats) with 0.6 m of SLR (projected for 2050) and 48% with 1.7 m of SLR (projected for 2100). Habitat conversion was more drastic in wetlands with larger proportions of marsh habitats relative to subtidal habitats and occurred more rapidly in small lagoons relative to larger sites. Our assessment can inform management of coastal wetland vulnerability, improve understanding of the SLR drivers relevant to individual wetlands, and highlight significant data gaps that impede SLR

[1] This chapter was published as Doughty CL, Cavanaugh KC, Ambrose RF, Stein ED. Evaluating regional resiliency of coastal wetlands to sea level rise through hypsometry-based modeling. Glob Chang Biol. 2019; 25(1): 78–92. It is reproduced here with minor formatting changes to comply with University of California dissertation specifications.

response modeling across spatial scales. This approach augments regional SLR assessments by considering spatial variability in SLR response drivers, addressing data gaps, and accommodating wetland diversity, which will provide greater insights into regional SLR response that are relevant to coastal management and restoration efforts.

## 1.2 Introduction

Sea level rise (SLR) and its impacts to coastal areas have been documented throughout the world (Wong et al. 2014) and are predicted to worsen in the coming decades (Church et al. 2013). Global sea levels are increasing, yet our ability to predict SLR impacts to coastal systems is complicated by variability in the factors driving SLR and system response (Stammer et al. 2013). The climatic, geologic and hydrologic processes that contribute to the relative SLR experienced along a coast are highly variable in time and space (Cazenave and Cozannet 2013). At continental or regional scales, these factors include the gravitational properties and movement of the earth's surface (Bamber and Riva 2010; King et al. 2012; Riva et al. 2010), and the circulation and volume of the ocean due to shifting surface winds, melting land ice contributions, and the thermal expansion of seawater (Church et al. 2013; Rhein et al. 2013). Sub-regional and local processes include tectonics, coastal geomorphology, and hydrology (Behrens et al. 2015; Cahoon et al. 2006; Rich and Keller 2013).

The variability associated with these SLR drivers makes it difficult to predict how SLR will affect coastal wetlands across broad spatial scales. The fate of individual wetlands will be determined by local rates of SLR, local topography and wetland morphology, but SLR response will be further mediated by biogeomorphic feedbacks among inundation, plant growth, organic matter accretion and sediment deposition (Kirwan et al. 2010; Mueller et al. 2016). Biogeomorphic feedbacks control vertical accretion and wetland elevation, and so are important in determining

response to SLR (Morris et al. 2002). These complex interactions determine which wetland sites may be able to keep pace with rising sea levels and which will not (Kirwan et al. 2016). Consideration of the spatial variability in both SLR drivers and SLR response mechanisms is necessary to compare SLR effects across individual wetlands.

The ability of SLR assessments to accommodate spatial variability in driver and response mechanisms is determined by data availability and computational modeling capability. Large-scale assessments, i.e., regional, national, continental, or global (Gornitz 1991; Klein and Nicholls 1999; Spencer et al. 2016), are purposefully designed to provide synoptic insights to SLR impacts by lowering computational expense and simplifying representation of the processes driving SLR (Fagherazzi et al. 2012). Large-scale assessments are often conducted at spatial resolutions of 1 km2 or greater (Passeri et al. 2015) or characterize sites or segments of coastline under a broad classification scheme (Lentz et al. 2016; Nicholls 2004; Spencer et al. 2016). Using broad classes and coarse spatial scales can obscure entire systems and some wetland types within a region, potentially biasing overall conclusions of wetland change.

Conversely, fine-scale assessments are better equipped to capture spatial variability at local scales (meters to 10s of meters) within individual wetlands. For example, process-based models such as the Wetland Accretion Rate Model for Ecosystem Resilience (WARMER) (Swanson et al. 2014), the Sea Level Affecting Marshes Model (SLAMM) (Clough et al. 2012), the Marsh Equilibrium Model (MEM) (Morris et al. 2002), and the integrated Hydro-MEM (Alizad et al. 2016) incorporate biogeomorphic feedbacks associated with inundation, plant growth, organic matter accretion and sediment deposition. When used in conjunction with site-specific data on vegetation and/or elevation, the results can provide insights into SLR response at high spatial resolutions (e.g., Alizad et al. 2016; Thorne et al. 2018). However, such comprehensive modeling

efforts are often specific to a single wetland site and are difficult to replicate over broad geographic ranges for a variety of wetlands due to time and resource constraints.

The limitations inherent to large-scale and fine-scale assessments have led to geographical gaps in our understanding of SLR response. The availability and accessibility of relevant data, as well as bias in assessment design caused by stakeholder incentives and resource availability, also contribute to these gaps (Preston et al. 2011). As a result, modeling efforts are normally conducted in well-studied and data-rich regions, wetland types or specific sites. The remaining, less-studied areas warrant attention, given that SLR response is highly context dependent. However, coastal wetland types with similar origin, geomorphology, dynamics, sediment balance, biogeochemistry and ecology will respond similarly to SLR and can therefore be grouped into a typology to provide a framework for the transfer of knowledge from data-rich to data-poor wetlands (Vafeidis et al. 2008). Here, coastal wetland typology reflects general classes like small deltas, tidal systems, lagoons, large rivers, estuaries and bays (Dürr et al. 2011). Inclusion of all wetlands and wetlands types would provide a more holistic regional perspective on SLR response that is required by both local and regional management efforts to ensure the resiliency of coastal ecosystem networks in the future (Gilmer et al. 2012; Stralberg et al. 2011).

This study aims to develop a nested SLR response assessment model that can be used to estimate SLR-induced habitat change across large geographic regions containing diverse wetland types. Our work augments current regional SLR assessments, bridging the gap between coarse regional and detailed site-specific models by addressing 1) the spatial variability of SLR drivers and response, 2) the ability to assess wetlands of different sizes and typologies using a common approach and 3) the need to accommodate differences in data availability across sites. We conducted our assessment in the southern California region, which has a diverse range of wetland

typologies representing many of the wetland types found globally, including Mediterranean areas, which have often been overlooked by previous SLR assessments. In addition, data availability varies a great deal for wetlands across southern California. Model outputs provide relative estimates of change in habitat composition for local (site-specific) and regional scales, which are necessary to inform regional SLR adaptation efforts in southern California. Our goal is to estimate overall wetland losses for the region due to future SLR and explore how relative losses would vary among wetland types. The modeling approach is also highly relevant to other coastal regions throughout the world where predicting future SLR response is complicated by habitat heterogeneity and limited data availability.

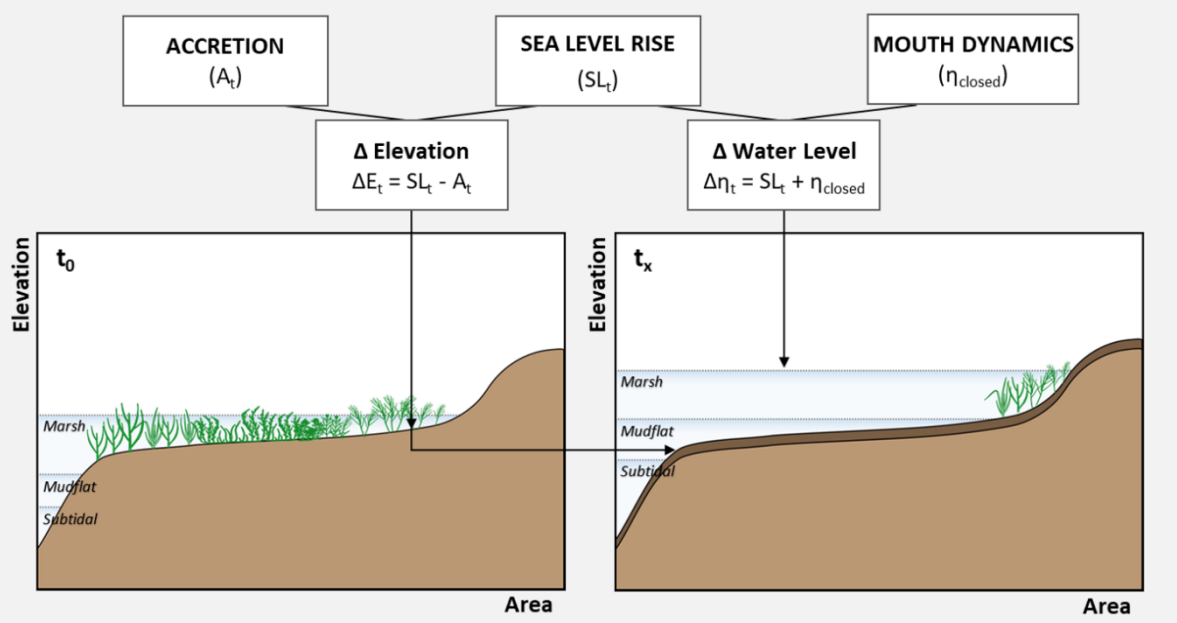


**Figure 1-1. Conceptual diagram of the SLR response habitat change model. Model drivers (sea level rise, accretion, and mouth dynamics) represent the processes inducing change in water levels and elevation. Elevation change (ΔEt) raises the current marsh hypsometry (t0, light brown) to future hypsometry ((tx), dark brown). Water level changes (Δηt) alter the marsh zones (subtidal, mudflat, and vegetated marsh) delineated by elevation (horizontal lines). Habitat change is calculated as the difference in area under the curve for each marsh zone under current and future conditions.**

## 1.3 Materials and Methods

### *1.3.1 Model Overview*

We developed a rule-based model that quantifies SLR-driven habitat conversion caused by the combined effects of SLR, accretion, and changes in water levels due to estuary mouth dynamics (Figure 1-1). The model uses hypsometric data, the measure of land elevation in relation to sea level, as a standardized basis for quantifying habitat change within individual wetlands across a region. Data gaps are addressed by incorporating the best available data at local to regional scales and by developing a wetland archetype framework to extrapolate data across similar wetland types. We conducted our assessment in southern California, and parameterized our model using data collected for the 105 coastal wetlands found in the region (Table 1-1). The model was executed for two SLR projections, 0.6 m by 2050 and 1.7 m by 2100, based on regional guidelines (California Coastal Commission 2015; Griggs et al. 2017; National Research Council 2012). Wetlands were constrained to their current boundaries, i.e., no upland migration was allowed, due to the uncertainties associated with predicting wetland migration (Anisfeld et al. 2017). Modeling was conducted in R (R Foundation for Statistical Computing, Vienna, Austria).

### *1.3.2 Regional Background*

Southern California is emblematic of many coastal regions worldwide in that it contains a large number of wetlands of various sizes and types. Historically, this region contained over 300 coastal wetlands occupying approximately 19,591 ha of wetland habitat (Stein et al. 2014). Since ca. 1800, close to 50% of wetland areas in this region have been converted to open water or non-estuarine habitat, i.e., developed, agricultural, or open space land uses (Stein et al. 2014). The existing wetland remnants are geographically isolated and constrained due to human modification

**Table 1-1. Data inputs required to inform and parameterize the SLR habitat change model.**

| Input | Scale | Value (units) | Source |
|---|---|---|---|
| **Relative Sea Level Rise** | | | |
| SLR 2050 Projection | Regional | 12.2 (mm $yr^{-1}$) | NRC 2012, Griggs et al., 2017 |
| SLR 2100 Projection | Regional | 16.6 (mm $yr^{-1}$) | NRC 2012, Griggs et al., 2017 |
| $t_0$, $t_1$, $t_2$ | | 2016, 2050, 2100 (yr) | |
| **Accretion** | | | |
| Measured Accretion ± Error | Site, Archetype | mm $yr^{-1}$ | SCCWRP Literature Review |
| **Mouth Dynamics** | | | |
| Daily Water Levels | Sub-regional | m | NOAA |
| Daily Wave Height, Period, Direction | Sub-regional | m, s, degrees | CDIP |
| Watershed Run-off Estimates | Sub-regional | $m^3$ $s^{-1}$ | SCCWRP |
| Estuary Mouth Width | Site | m | SCCWRP |
| Estuary Closure Estimates | Site | % | SCCWRP |
| Estuary Area | Site | $km^2$ | SCCWRP |
| **Habitat Change** | | | |
| Current Habitat Extent | Site | $m^2$ | SFEI/SCCWRP |
| Habitat Elevation Relationships | Sub-regional | | SCCWRP/SFEI Literature Review |
| LiDAR-derived DEM | Regional | $m^2$ | 2009-2011 CA Coastal Conservancy Coastal Topobathy Project |
| Estuary Hypsometry | Site | $km^2$ / z* | This study |

Abbreviations: National Resource Council (NRC), Southern California Coastal Water Research Project (SCCWRP), National Oceanic and Atmospheric Association (NOAA), Coastal Data Information Program (CDIP), San Francisco Estuary Institute (SFEI)

of the landscape to serve urban development, military uses, industrial and agricultural expansion, recreation and tourism (Zedler 1982).

### *1.3.3 Wetland Archetype Classification*

We have grouped wetlands in this region into archetypes to facilitate extrapolation of data between wetlands to fill the gaps in our knowledge of the region. Archetypes represent wetlands with similar physical structure and ecosystem drivers that are expected to react in similar ways to SLR. To develop the archetypes, we compiled data on the physical structure and processes for

each wetland in the region; these variables fell into five general categories including catchment properties, wetland dimensions (e.g., size and slope), proportion of subtidal to intertidal areas, inlet dimensions and area, and wetland volume and capacity. Of the 105 wetlands, 46 had sufficient data to be included in a K-Means cluster analysis where cluster numbers ranging from 4 – 8 were tested to maximize separation and minimize misclassification rates.

The resulting archetypes were further refined using a discriminant function analysis to identify the key predictor variables that generated the greatest accuracy of classification. Key predictors included wetland area, erosion area (area/depth), slope from mouth to head, integrated slope, mouth elevation, mean mouth width, total area inundated at spill height, percent wetland at low tide and total percent subtidal. Finally, we mapped habitat data from the National Wetlands Inventory (NWI) and the Classification and Assessment with Landsat of Visible Ecological Groupings (CalVeg) system onto the clusters to produce habitat associations for each archetype. Validity of the resulting archetypes were tested by performing a bias analysis on the key predictor variables and the remaining 59 systems not included in the cluster analysis. Archetypes were also qualitatively assessed by regional experts who were allowed to add modifiers to each wetland based on mouth armoring, mouth migration potential, and/or presence of engineered channels.

The resulting archetypes include small creeks, small lagoons, intermediate estuaries, large lagoons, large river valley estuaries, fragmented river valley estuaries, and open bays and harbors (SCWRP 2018). Intermediate estuaries, commonly referred to as intermittently opening and closing estuaries or bar-built estuaries, are note-worthy because they represent a significant component of coastal wetlands in southern California (Zedler 1996). Each of the 105 wetlands in the analysis was classified as one of the seven archetypes (Figure 1-2).

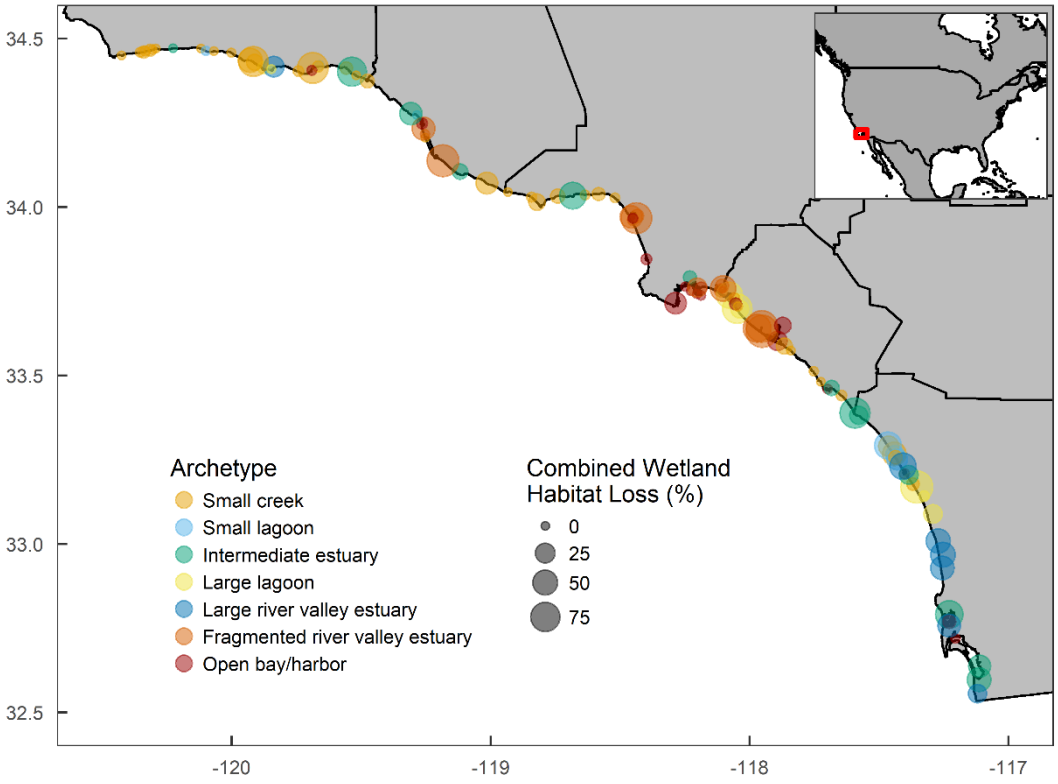


**Figure 1-2. Archetype classification and projected percent difference in combined wetland habitat (vegetated marsh and unvegetated mudflat) for individual wetland sites for 1.7 m SLR (2100) in the southern California region.**

### *1.3.4 Model Components*

#### *1.3.4.1 Sea Level Rise*

Sea level projections for the Los Angeles area range from 12.7 – 60.8 cm for the year 2050, and from 44.2 – 166.5 cm for 2100 (National Research Council 2012). We selected the maximum of the projected SLR ranges for 2050 and 2100 (0.6 m and 1.7 m, respectively). We converted these projected levels of inundation to SLR rates (mm $yr^{-1}$) by dividing by the difference in time period between our modeling time points (2050, 2100) and the reports' baseline (2000), resulting in SLR rates of 12.2 mm $yr^{-1}$ for 2050 and 16.6 mm $yr^{-1}$ for 2100. A regional default value for SLR was selected to provide a standardized baseline for comparison across wetlands and also to align with ongoing regional efforts (SCWRP 2018).

### *1.3.4.2 Accretion*

Empirical estimates of accretion in coastal wetlands in southern California were obtained through a review of published literature (Table S1-1). The records included in the analysis were derived from radiocarbon dating, radiocesium dating, and paleoenvironmental soil core analysis of pollen and cover periods ranging from ~30 to 10,000 years. Accretion estimates were standardized to millimeters per year (mm $yr^{-1}$). Records reflecting short term (< 10 yr) accretion and episodic sediment deposition from storms were excluded from the analysis to ensure that model inputs reflect long-term accretion rates on temporal scales comparable to SLR projections.

Because of the limited availability of published accretion records specific to this region (see Results), we used the archetype framework to extrapolate data from well-studied sites to data-poor sites. When empirical data was available for a given wetland, we used site-wide averages across all intertidal marsh zones as accretion input. For wetlands lacking empirical data, we calculated archetype accretion estimates from our literature review by aggregating records first by marsh zone within a site, then by site and finally by archetype to provide inputs for similar sites specific to this region (Table 1-2). Accretion rates for small creeks and lagoons were set to 0 mm

**Table 1-2. Archetype accretion rates estimated from the literature review**

| | | Accretion ± SD (mm $yr^{-1}$) | | |
|---|---|---|---|---|
| **Archetype** | **Zone** | **By Zone** | **Total** | **n** |
| Small Creek | | No Data | | 0 |
| Small Lagoon | | No Data | | 0 |
| Intermediate Estuary | Low | 3.63 | 3.63 | 1 |
| Large Lagoon | Mid | 12 | 9.55 ± 9.40 | 4 |
| | High | 21.8 | | |
| Large River Valley Estuary | Low | 4.8 | 4.68 ± 2.94 | 5 |
| | Mid | 4.83 ± 5.49 | | |
| Fragmented River Valley Estuary | Low | 1.38 | 1.2 ± 0.65 | 3 |
| | Mid | 0.49 | | |
| Open Bay/Harbor | Low | 2.83 | 3.84 ± 2.32 | 5 |
| | Mid | 3.24 ± 2.82 | | |
| | High | 7.13 | | |

$yr^{-1}$ because of a lack of empirical data and to avoid additional uncertainty associated with modeling fluvial sediment discharge. Contributions to accretion from both allochthonous and autochthonous inputs are relatively low for these systems given the variable precipitation patterns in southern California, small catchments sizes and the small vegetated areas associated with these systems.

#### *1.3.4.3 Mouth Dynamics*

We included an estuary mouth dynamics component in our assessment to address the intermittently opening and closing state of estuary mouths common to southern California and throughout the world (Rich and Keller 2013). Changing mouth state is a product of marine and fluvial drivers, such as wave energy and river discharge, which contribute to changes in estuary water levels by altering the height and position of terminal estuary bars. As estuary bars rise with sea level, the flood risk associated with estuary closure is expected to worsen (Behrens et al. 2015). These changes can in turn affect extent and duration of inundation and therefore, habitat distributions. To inform our model, we conducted a separate modeling analysis which includes a closure index (PWA 2003; Williams and Cuffe 1995) and a water balance model (Behrens et al. 2013; Behrens et al. 2015).

These analyses were conducted to estimate the probability of changing mouth state and the subsequent changes to estuary water levels for individual sites. We hypothesize that increased sea levels will increase the frequency of estuary closure, inducing a shift in dominant mouth state, and will ultimately increase water levels within a site. To test our hypothesis, we created a synthetic daily time series for current, 2050 and 2100 sea levels using local NOAA tide level data, Coastal Data Information Program (CDIP) water level and wave data, and Southern California Coastal Water Research Project (SCCWRP) coastal watershed run-off data for the last 20 years (Table 1-

1). To predict future closure indices, we manipulated wave and tidal inputs to reflect SLR projections of 0.6 m for 2050 and 1.7 m for 2100.

In order to estimate the probability of changing mouth state, we used the closure index (S) metric used by Williams and Cuffe (1995) and PWA (2003):

$$S = Pw/Pt \quad (1)$$

$$Pw = 0.5\rho g H_s C \quad (2)$$

$$Pt = (\gamma h_T)/b * (\Omega/T+Q) \quad (3)$$

Where $P_w$ is wave power, $\rho$ is the constant 1 kg $L^{-1}$ for water density, g is the constant 9.81 m $s^2$ for acceleration by gravity, $H_s$ is significant wave height and C is wave group velocity (C=1.56*s, where s is wave period). Tidal power ($P_t$) is also described above, where $\gamma$ is the constant 1000 kg unit weight of water, $h_T$ is the tidal range, b is the estuary mouth width, $\Omega$ is tidal prism ($\Omega$= hT*A, where A is the water surface area of the basin), T is the ebb tide period and Q is fluvial discharge. We estimated the daily likelihood of closure for each estuary over the entire time series.

Next, we estimated how water levels may change in a given system when it is predicted to be open (S < 0.1) or closed (S > 0.1). In doing so, we made the assumption that every time closure risk is above the threshold, the system closes. This likely over-predicts mouth closure; however, we wanted to calculate the percent increase in predicted closure associated with SLR and the hypothetical changes to system water level based on the time series data. Also, this mouth dynamics response threshold allowed us to repeat this process and compare outcomes for all systems where data was available. We estimated daily system water levels for systems with both "open" and "closed" conditions using a simplified model based on the work of Behrens et al.

(2013; 2015). When the system was at low risk of closure ($S < 0.1$), we assumed the system would be open and that system water level ($\eta$) would track mean seal level (MSL):

$$\eta = MSL \quad (4)$$

When the system was at high risk of closure ($S > 0.1$), we assumed the system would be closed and that system water level ($\eta$) would be largely determined by the starting conditions of the estuary mouth and net fluvial inputs ($Q_{net}$):

$$\eta_{t+1} = \eta_t + Q_{net}/Area_\eta \quad (5)$$

$$Q_{net} = Q_{river} - Q_{evap} \quad (6)$$

Where $\eta_{t+1}$ is the future system water level, $\eta$ is current water level, $Q_{net}$ is the sum of fluvial inputs and evaporation, and $Area_\eta$ is the surface area of the system at a given water level determined by system hypsometry.

Seventy of the 105 sites in the region were considered in our mouth dynamics analysis because they did not have openly-engineered estuary mouths. Of these, 36 sites had sufficient data and fall within several archetypes: small creeks, small lagoons, intermediate estuaries, large perennially-open lagoons and large river valley estuaries. For these sites, we calculated the percent of time that the site was expected to have high closure risk, and the hypothetical changes to water levels when we assume the site is closed. Estimates of percent closure for 2050 and 2100 were added to estuary closure estimates for the present day and were then binned into the following categories: predominantly open (<40%); intermittently open/closed (>40%, <60%); and predominantly closed (>60%). Predominantly open sites received no additional changes in water level; intermittently open/closed sites received a dampened (0.5x) increase in water level; and predominantly closed sites received the full (1x) increase in water level associated with closed mouth state. The findings of our estuary mouth dynamics modelling analysis were aggregated by

archetype to extrapolate to other systems with similar mouth dynamics characteristics but without sufficient data to be included in our mouth dynamics model.

### *1.3.5 Wetland Hypsometry*

Hypsometric data were developed for the extent of each of the 105 wetlands using a digital elevation model (DEM) obtained from the 2009-2011 NOAA-CA Coastal Conservancy Coastal Lidar Project (Table 1-1). The DEM had a spatial resolution of 1 $m^2$ and horizonal and vertical error of 50 cm and 9.4 cm, respectively. DEM elevation relative to the North American Vertical Datum 1988 (z) was converted to z*;

$$z^* = \frac{z - MSL}{MHHW - MSL} \quad (7)$$

where z* is the relative elevation within the tidal range calculated as a dimensionless ratio of elevation referenced to mean sea level (MSL) and mean high high water (MHHW) from the nearest NOAA tidal station (Swanson et al. 2014). z* was used in order to standardize estimates of elevation changes across wetlands with varying tidal datums, elevations and tidal ranges. Standard hypsometric curves providing information on wetland elevation relative to sea level were created by cumulatively summing the area that falls within z* bins of 0.05.

### *1.3.6 Changes in Elevation and Water Level*

Model components for SLR, accretion and mouth dynamics were used to estimate changes in elevation and water level relative to our 2016 ($t_0$) baseline. Change in marsh elevation ($\Delta E$) is determined by SLR and accretion:

$$\Delta E_t = SL_t - A_t \quad (8)$$

Where $SL_t$ is the change in sea level occurring by the year benchmark ($t_{1,2}$=2050, 2100) associated with the SLR projections and $A_t$ is the total accretion by that time. $SL_t$ and $A_t$ are

calculated from the rates described above by multiplying by the desired time period ($t_{1,2}$ - $t_0$) and converting to meters.

Change in water level ($\Delta\eta$) was determined by SLR and mouth dynamics:

$$\Delta\eta_t = SL_t + \eta_{closed} \quad (9)$$

Where $\eta_{closed}$ is the hypothetical change in water level when a site is assumed to be closed (see section *Mouth Dynamics*). $\Delta E_t$ and $\Delta\eta_t$ were estimated for all 105 wetlands for each SLR scenario.

### *1.3.7 Habitat Change*

We used the estimated changes in elevation and water levels for 2050 and 2100, along with the hypsometric curves developed for each wetland to estimate areal changes in habitat occurring with SLR (Figure 1-1). Changes in elevation act upon the hypsometric curve itself, increasing the z* values by $\Delta E$ (which has been converted from meters to z* using the local tide datum), while keeping the total area of the marsh constant. Changes in water level are used to manipulate the z* ranges that correspond to different wetlands habitats (Figure 1-1, Table S1-2). z* ranges were informed by a synthesis of regional habitat-elevation data.

We calculated the area within three habitat classes (subtidal, unvegetated mudflat, and vegetated marsh) for each of the 105 wetlands under current sea levels and 0.6 m and 1.7 m SLR scenarios. We report the estimated changes to each habitat class and two metrics of wetland habitat loss. For the purpose of this study, wetland habitat loss reflects the combined loss of vegetated marsh and unvegetated mudflat areas, which assigns equal weight to these ecologically important classes and also aligns with ongoing regional efforts (SCWRP 2018). First, we calculated percent change as the difference in wetland area between the existing area and the predicted area under the SLR scenario divided by the existing area (hereafter “percent change”). Second, we calculated

percent difference as the decrease in the percent of wetland area for each site between the existing conditions and the predicted conditions under the SLR scenarios to produce an estimate of the relative decrease in the percent of wetland area (hereafter "percent difference"). We report percent loss using the "percent difference" approach in order to account for site sizes when comparing wetland loss among sites, archetypes, and the region.

#### *1.3.8 Uncertainty and Sensitivity Analyses*

We conducted an uncertainty analysis to address errors of measurement and sensitivity to model parameters that may influence model outputs. We propagated errors (e.g., standard error, standard deviation, 95% confidence intervals) associated with each of the model inputs through the model to determine the cumulative errors in the habitat change output. Model inputs considered include SLR rate, accretion rate, water level changes caused by mouth dynamics, and vertical error of the DEM. This error analysis provides us with a bookended range of potential habitat change for each site. We conducted a sensitivity analysis by modifying each input ±50% while leaving all other inputs unchanged. We modified DEM inputs by ±50 cm to test sensitivity to initial elevation for a broad, hypothetical range of vertical error feasible for digital elevation datasets. The sensitivity analysis provides an estimate of the percent change in habitat caused by modifying the inputs, which allows us to identify the importance of each input in predicting habitat change.

### 1.4 Results

#### *1.4.1 Regional Accretion and Estuary Mouth Dynamics*

Investigation of regional accretion and mouth dynamics were conducted to inform the model and revealed inter-archetype differences that may cause differential response to SLR. Over 100 records of accretion rates were obtained for 10 wetland sites from 16 published sources and of these 58 records were suitable for analysis (Table S1-1). Estimates of accretion per archetype

based on the site-wide averages ranged from 1.2 ± 0.7 mm $yr^{-1}$ in fragmented river valleys to 9.5 ± 9.4 mm $yr^{-1}$ in large lagoons (Table 1-2). Differences in accretion between archetypes were useful for modeling but were not statistically significant given low sample sizes following data aggregation due to data limitations of this study (Table 1-2). Similarly, the mouth dynamics modeling analysis indicates that certain archetypes may experience increased likelihood of closure causing increased estuary water levels with future SLR (Table 1-3). For 2050, likelihood of closure was predicted to increase by 0 – 13% with water levels increasing by an average of 34 cm, and by 0 – 48% with increases of 114 cm for 2100. Specifically, small creeks and lagoons are most at risk for increased closure, while larger sites with sufficient fluvial runoff are more likely to remain open. Although differences in increased likelihood of closure were detected, estimates of increased estuary water levels were similar among archetypes and neither was found to be significantly different across archetypes.

**Table 1-3. Mouth Dynamics Analysis results. Increased likelihood of high closure risk and the resultant increases in water levels when a system is presumed to be closed.**

| | 0.6 m SLR | | 1.7 m SLR | |
|---|---|---|---|---|
| **Archetype** | **Δ Likelihood of Closure (%)** | **Δ Estuary water level (m)** | **Δ Likelihood of Closure (%)** | **Δ Estuary water level (m)** |
| Small Creek | +13% | 0.43 | +27% | 1.38 |
| Small Lagoon | +8% | 0.43 | +48% | 1.55 |
| Intermediate Estuary | +3% | 0.42 | +14% | 1.41 |
| Large Perennially-Open Lagoon | +7% | 0.42 | +21% | 1.38 |
| Large River Valley Estuary | 0% | 0 | 0% | 0 |
| Fragmented River Valley Estuary | No Data | No Data | No Data | No Data |
| Open Bay/Harbor | No Data | No Data | No Data | No Data |

Changes calculated using 2016 as the baseline. Values for change in estuary water levels represent the contribution of mouth dynamics alone; these values will be combined with inundation from SLR in order to estimate total increases in water level in the estuary.

### *1.4.2 Wetland Habitat Change and Loss*

Estimates of subtidal, unvegetated mudflat, and vegetated marsh areas were made for each of the 105 sites under current, 2050 (0.6 m) and 2100 (1.7 m) projected sea levels. Site-specific estimates of wetland habitat area were aggregated to the region and to the regional archetypes for large-scale inferences into SLR response (Figure 1-3). Region-wide, current vegetated marsh habitats encompass 26.6 $km^2$ and are predicted to decrease to 19.9 $km^2$ with 0.6 m SLR and 8.3 $km^2$ with 1.7 m SLR, which represent losses of 25.3% and 68.8%, respectively. Unvegetated mudflat habitats account for 12.5 km2 of the regional habitat under current conditions and are predicted to increase to 14.4 $km^2$ with 0.6 m SLR and decrease to 12.1 $km^2$ with 1.7 m SLR, representing a 15.7% gain and a 3.0% loss, respectively. Combined wetland habitat (vegetated marsh and unvegetated mudflat) for the entire region currently comprises 39.1 $km^2$, or 30.8%, of the total wetland area (Table 1-4). When open bays and harbors, which are predominately subtidal sites, are excluded, the current proportion of combined wetland habitat in the region is approximately 70%. With SLR, the combined wetland area across the entire region (including open bays and harbors) are predicted to decrease to 34.3 $km^2$ by 2050 and 20.4 $km^2$ by 2100 (Table 1-4). This represents regional losses of 12.3% and 47.8% of combined wetland habitat with 0.6 m and 1.7 m SLR, respectively.

**Table 1-4. Predicted percent change in wetland (vegetated marsh and unvegetated mudflat) habitat area for the southern California region and individual wetland archetypes.**

| | Wetland Area ($km^2$) | | | Percent Change (%) | |
|---|---|---|---|---|---|
| **Archetype** | **Existing** | **0.6 m SLR** | **1.7 m SLR** | **0.6 m SLR** | **1.7 m SLR** |
| Small creek | 0.08 | 0.06 | 0.01 | 25.0% | 87.5% |
| Small lagoon | 0.04 | 0.008 | 0.001 | 80.0% | 97.5% |
| Intermediate estuary | 14.9 | 13.5 | 9.9 | 9.4% | 33.6% |
| Large lagoon | 5.6 | 4.3 | 1.1 | 23.2% | 80.4% |
| River valley estuary | 9.4 | 9.2 | 6.2 | 2.1% | 34.0% |
| Fragmented river valley estuary | 4.1 | 2.9 | 0.9 | 29.3% | 78.0% |
| Open bay/harbor | 5.0 | 4.3 | 2.1 | 14.0% | 58.0% |
| **Region** | 39.1 | 34.3 | 20.4 | 12.3% | 47.8% |

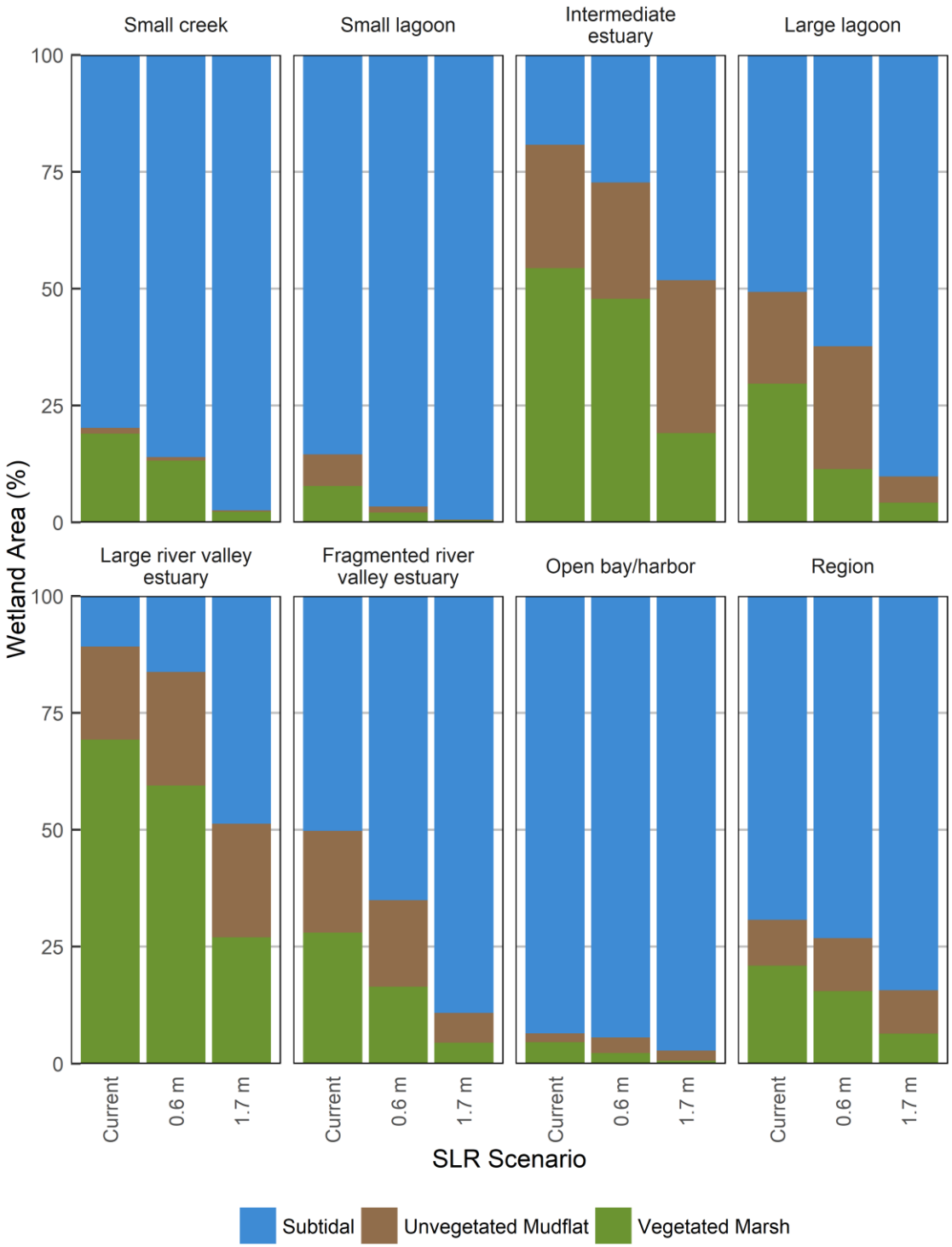


**Figure 1-3. Current and predicted habitat change for wetland archetypes under two sea level rise scenarios when wetlands are confined to existing boundaries.**

Percent change in combined wetland habitat for the regional archetypes provide a more detailed look at SLR response (Table 1-4). Small archetypes with an initially low proportion of wetland habitat are predicted to experience rapid habitat loss. Specifically, small creeks currently make up 0.08 $km^2$ of wetland habitats in the region but are estimated to decline to 0.06 $km^2$ (-25%) by 2050 and to 0.01 $km^2$ (-88%) by 2100. Similarly, small lagoons comprise 0.08 $km^2$ of existing wetland areas in the region but will be reduced to 0.008 $km^2$ (-80%) by 2050 and only 0.001 $km^2$ (-98%) by 2100. Larger archetypes with higher initial proportions of wetland habitats, such as intermediate estuaries, large lagoons, and large river valley estuaries, are expected to experience slight reductions in the percent of wetland area with 0.6 m SLR, however, with 1.7 m SLR these archetypes will experience more drastic declines in wetland area, reflecting overall gains in subtidal habitat and conversion of vegetated marsh areas to unvegetated mudflats (Figure 1-3). For example, intermediate estuaries comprise 14.9 $km^2$ of existing wetland areas in the region and will lose 9.4% of wetlands by 2050 and 33.6% by 2100 (Table 1-4). In the course of this overall reduction of wetland area, this archetype is predicted to gain 7.8% of unvegetated mudflat areas from 2050 to 2100 at the expense of vegetated marsh (Figure 1-3). Wetland habitat loss, as an estimate of percent change, is predicted to be minimal in open bays and harbors, which are large, predominantly deep subtidal systems and are often highly modified and managed.

Site-specific estimates of SLR-driven change to wetland habitat areas provide insights into the range of potential responses within archetypes (Figure 1-2, Figure 1-4). Percent difference in wetland area per site reflects the combined loss of vegetated marsh and unvegetated mudflat compared to the current proportion of wetland area per site (Figure 1-2). With 0.6 m SLR, percent difference in wetland habitat per site ranged from -1.1 to 74.2%, indicating a highly variable response to SLR given site-specific model parameterization. Similarly, 1.7 m SLR estimates

indicate differential site response but overall increased percent difference in wetland habitat ranging from -0.7 to 94%. Low or negative predicted percent difference in estimates suggest that some sites may be able maintain or gain wetland habitats (vegetated marsh and unvegetated mudflat) while others will likely lose habitat area.

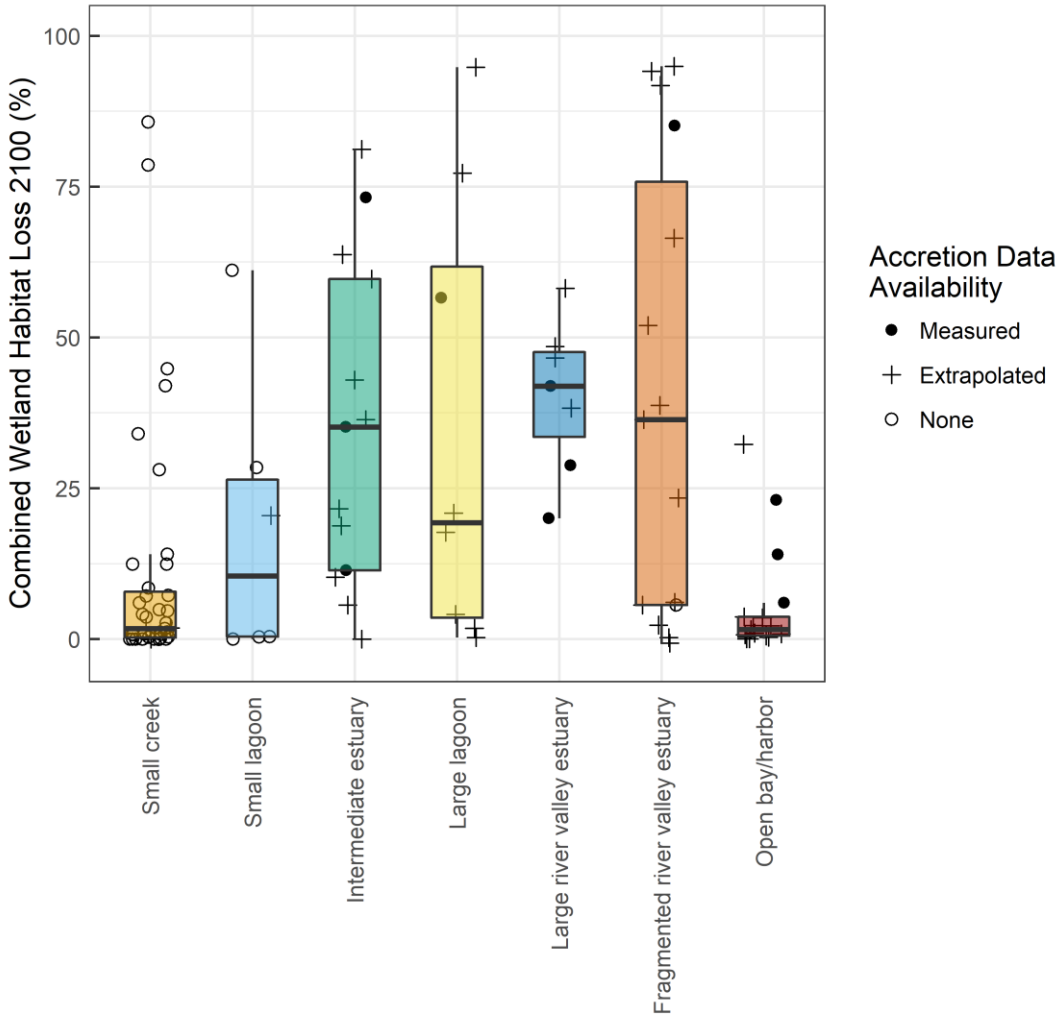


**Figure 1-4. Inter- and intra-archetype variability in percent difference in combined wetland habitat (vegetated marsh and unvegetated mudflat) predicted with 1.7 m SLR by 2100. Boxplots indicate the distribution of percent difference for each archetype including the median, first and third quartiles. Points indicate each site within the archetype class and the availability of accretion data for that site: data was either available from our literature review (measured, closed circle), extrapolated using the archetype framework (extrapolated, plus) or unavailable (none, open circle). For sites where accretion data was unavailable (small creeks and lagoons), estimates were made using a bathtub model assuming no accretion.**

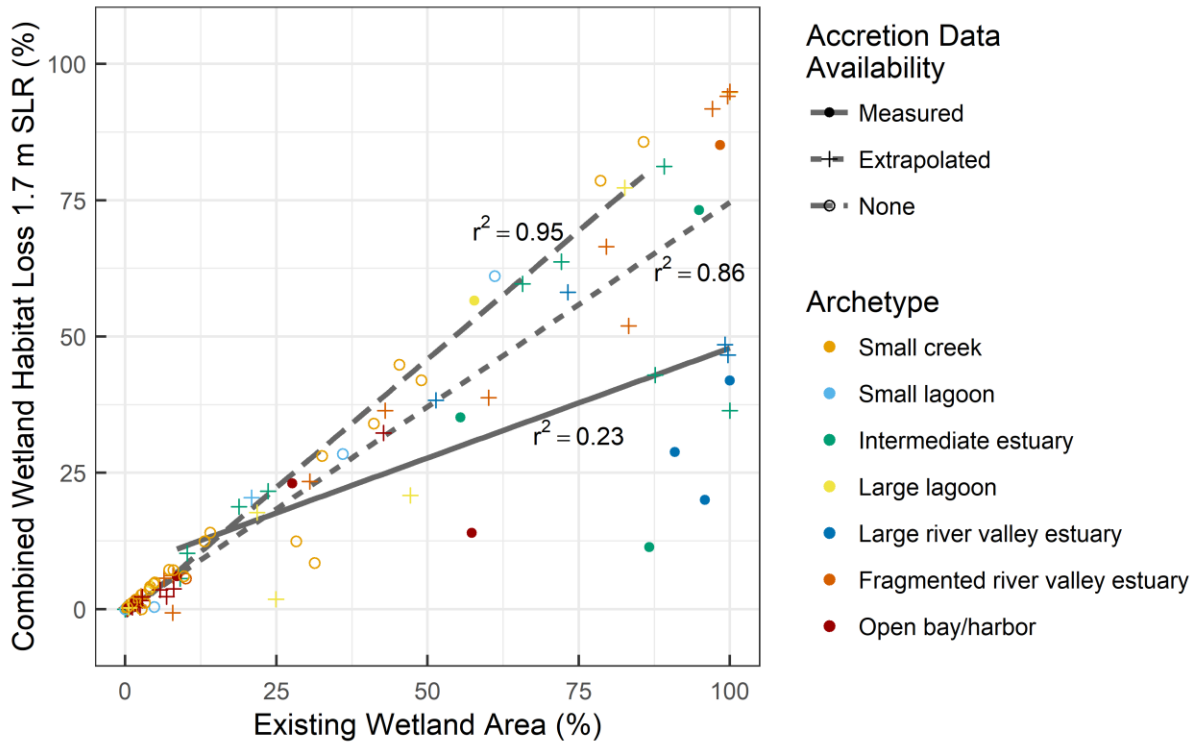


**Figure 1-5. Relationship between predicted percent difference in wetland habitat with 1.7 m SLR by 2100 and existing (2016) percent wetland areas (vegetated marsh and unvegetated mudflat) for all 105 sites. Site symbology reflects the archetype classification (color) and data availability of accretion inputs for that site (shape). Accretion data was either available from our literature review (closed circle, solid trendline), extrapolated using the archetype framework (plus, dashed trendline) or unavailable (open circle, long-dash trendline). For sites where accretion data was unavailable (small creeks and lagoons), estimates were made using a bathtub model assuming no accretion.**

### *1.4.3 Model Uncertainty and Sensitivity*

Uncertainty analyses revealed the ranges of potential habitat outputs when input error was propagated though the model (Figure 1-6). The estimated range of error with 0.6 m SLR is 12.9 – 33.7 $km^2$ for vegetated marsh, 4.1 – 20.3 $km^2$ for unvegetated mudflat, and 80.0 – 97.2 $km^2$ for subtidal habitats. For 1.7 m SLR, the estimated range of error is 5.7 – 37.5 $km^2$ for vegetated marsh, 1.6 – 69.8 $km^2$ for unvegetated mudflat, and 21.2 – 13.8 $km^2$ for subtidal habitats. When the range of error was compared to the model estimates for each habitat type for 2050 and 2100, we found that the predictions for subtidal areas are high within the range and that the predictions for vegetated areas are low within the range, while predictions for unvegetated mudflats are in the

middle of the range (Figure 1-6). Although this renders model predictions for vegetated areas as conservative, the gains in vegetated areas suggested by the uncertainty analysis reflect unlikely scenarios of low SLR with high accretion. Overall, predictions for 2100 exhibits higher uncertainty due to model inputs than those for 2050.

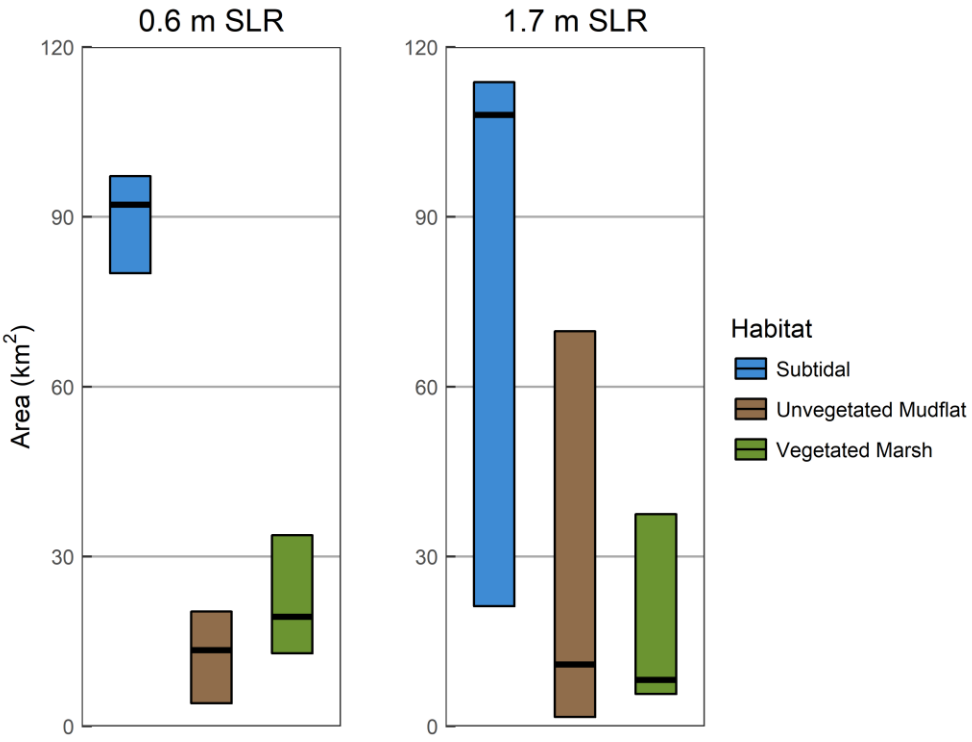


**Figure 1-6. Bookended range of the potential area for each wetland habitat when error is propagated through the model. Black lines represent the area of each habitat originally predicted by the model. Floating bars represent the range of possible values when model input errors are considered.**

The sensitivity analysis revealed that model estimates of wetland habitat area are most sensitive to initial elevation and SLR, followed by accretion and mouth dynamic inputs (Figure 1-7). When initial elevation was increased by 50 cm, an additional 53.7% of vegetated marsh was retained with 0.6 m SLR and an additional 99% was saved with 1.7 m SLR compared to the original model estimates. Increasing SLR estimates by 50% caused reductions of 22.6% and 53.5% for vegetated marsh areas for 2050 and 2100, respectively. Decreasing SLR estimates by 50% caused

gains in vegetated marsh areas but is not a realistic scenario. Increasing accretion inputs resulted in additional vegetated marsh areas (+10.3%, +57.7%), while decreasing accretion resulted in additional subtidal and unvegetated mudflat areas. Percent change to habitat areas when modifying water levels associated with mouth closure were minimal compared to other model inputs but indicate slight increases to unvegetated marsh areas when this input was increased. Overall, the sensitivity of model outputs increases from 0.6 m SLR to 1.7 m SLR.

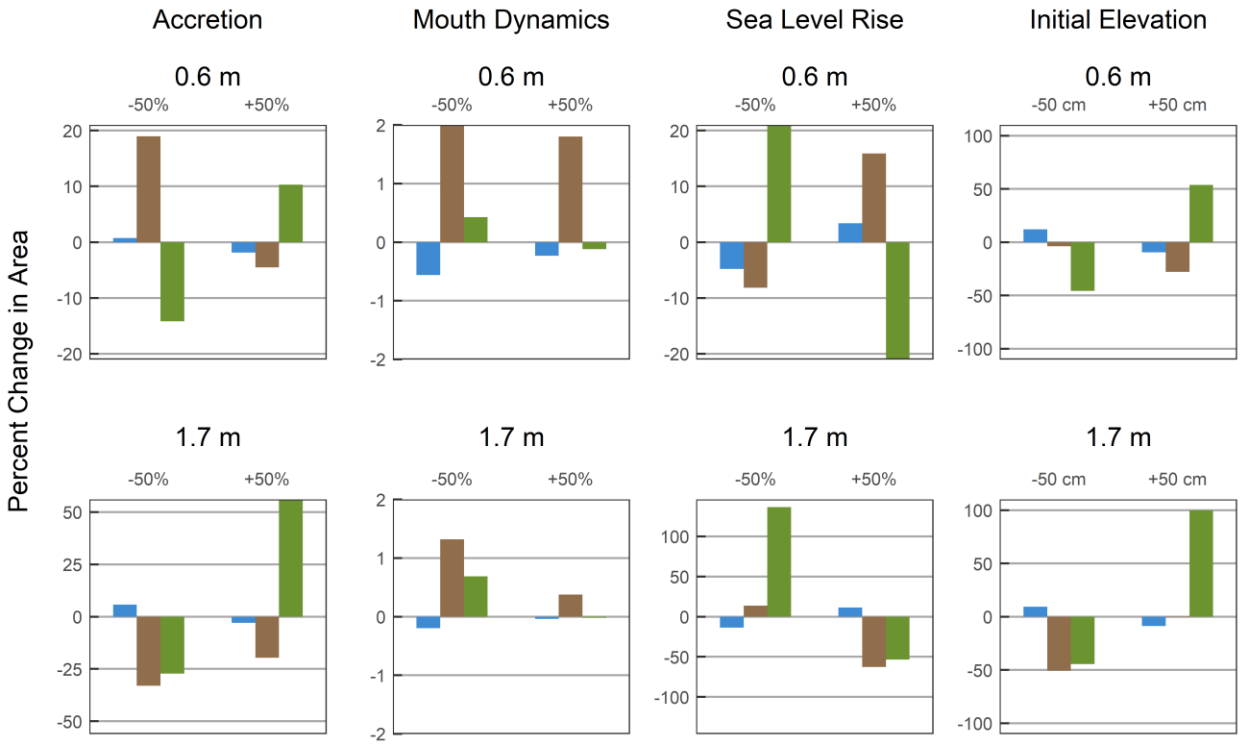


**Figure 1-7. Percent change in habitat area caused by sensitivity to model inputs. Percent change is calculated based on the area of each habitat (subtidal (light grey), unvegetated mudflat (grey), and vegetated marsh (dark grey)) originally predicted by the model. Sensitivity was analyzed by varying model parameters Accretion, Mouth Dynamics, SLR by ±50% and Initial Elevation by ±50 cm. Note varying y-axis scales in plot panels.**

## 1.5 Discussion

Southern California exemplifies many coastal regions threatened by SLR, where efforts to understand future impacts are challenged by spatial variability in drivers and responses, a heterogeneous coastal landscape, and limited data availability. Wetland hypsometry offers a

standardized modeling approach that can provide multi-scale insights to SLR response for a diverse region. Hypsometry data can be developed for any number of wetland sites using a consistent approach and readily available datasets. The output of hypsometric analysis provides a standardized measure of wetland elevation relative to current sea levels for each site across a large geographic area, making it a universal foundation for modeling SLR across sites of various morphologies and sizes. The majority of SLR modeling efforts are based on some metric of elevation, yet to our knowledge, wetland hypsometry as a measure of z* has not been developed for 100+ sites at 1-m resolution to identify site-level impacts throughout a region, as we have done here. This framework can be applied to any other coastal regions where elevation data are accessible. When combined with analysis of wetland typology (or archetypes), this approach reduces the gap between fine-scale (site specific) and large-scale assessments.

Large-scale assessments often provide a limited understanding of regional SLR response (Fagherazzi et al. 2012). Recent global assessments report wetland losses up to 22 – 59% under low SLR (0.3 and 0.5 m) and 78% with high SLR (1.1 m) (Nicholls 2004; Nicholls et al. 1999; Spencer et al. 2016). Such assessments often indicate no or low vulnerability to SLR in southern California relative to other regions because these wetlands are either not included in global databases (e.g., RAMSAR) or are characterized under a broad coastal classification scheme (Nicholls et al. 1999; Spencer et al. 2016). Our findings indicate that when coastal wetlands are confined to their existing extents (i.e. not allowed to migrate), the southern California region could experience combined wetland habitat losses of 12% and 48% with 0.6 m and 1.7 m of SLR. For vegetated marsh alone, these figures increase to 25% and 68% loss, respectively. These projected losses fall within the range of global assessments, and are comparable to similar regional assessments (e.g., 45% loss with 0.69 m SLR in Georgia (Craft et al. 2009)). Our modeling

approach provides reasonable SLR response estimates at large spatial scales, but also facilitates assessment at smaller scales to provide contextualized intra-regional patterns in SLR response.

Wetland SLR response at intermediate scales is a critical missing piece in predicting SLR impacts globally. To address this, our assessment characterized variability in SLR-driven habitat loss among and within coastal wetland archetypes. Through the use of archetypes in southern California, we were able to identify wetland types that have a higher risk of habitat loss and to elucidate the underlying processes that lead to habitat loss. Many of the factors contributing to high SLR vulnerability in this study region are universal and applicable worldwide. For example, large bays and harbors are predicted to experience minimal relative loss of vegetated marsh and unvegetated mudflat habitats because existing habitat composition in these systems is predominantly subtidal with few fringing wetlands. Also, bays and harbors are often armored and highly managed to maintain deep water and remain open to the ocean; consequently, most impacts will be to subtidal habitats. Conversely, small creeks and lagoons are at greater risk for more rapid loss of wetland because of their small extent and the steep grade of adjacent upland transition zones, which limits migration potential (Donnelly and Bertness 2001; FitzGerald et al. 2008). Moreover, these small systems often have limited opportunity for accretion, decreasing their ability to accommodate SLR.

Insights at the archetype level are especially valuable for intermediate estuaries, which exhibit a wide range of potential responses to SLR. This archetype is characteristically diverse because it consists of systems that are naturally dynamic, fluctuating between open and closed mouth states due to fluvial, tidal and wave drivers (Behrens et al. 2015). These dynamic estuarine systems are present along the coasts of the Western United States, Mexico, South America, Europe, South Africa, Asia and Australia (McSweeney et al. 2017) and are often underrepresent

in large-scale assessments despite offering important ecosystems services like refuge for endangered fish species (e.g., Swenson, 1999). Incorporating estuary mouth dynamics into SLR response models is challenging because mouth dynamics are expected to be heavily influenced by SLR (Haines and Thom 2007) and are difficult to model. Therefore, the difficulty in predicting mouth dynamics means that the intermediate estuary response to SLR also comes with a high amount of uncertainty. Given that intermediate estuaries are more widespread globally than previously reported (McSweeney et al. 2017), additional monitoring and modeling of estuary dynamics relative to coastal and fluvial processes also subject to climate change represent a high research priority.

Similarly, fragmented river valleys exhibit the largest range of SLR responses because they also encompass a diverse group of wetlands, all of which have been highly modified by humans. This archetype exemplifies the global phenomenon of coastal squeeze caused by shoreline hardening, where natural systems have become hydrologically altered and bounded by concrete structures like seawalls and jetties (Pontee 2013). Anthropogenic impacts like habitat fragmentation and shoreline hardening in coastal wetlands will accelerate habitat loss with future SLR (Gittman et al. 2015). However, even archetypes considered to be unmodified are also highly vulnerable to SLR. Larger archetypes, including intermediate estuaries, large lagoons, and river valley estuaries, will experience the greatest amount of habitat change in the region. Although these systems are characteristically large, predominantly comprised of wetland habitat, and have shallow grades ideal for upland migration, it is likely that allochthonous and autochthonous inputs to accretion will not be sufficient to maintain elevation with SLR in the long term. Within these larger archetypes there is also wider range of site responses, which reflects the intra-archetype diversity of system characteristics.

Indeed, we found that site-level response to SLR is highly variable, further emphasizing the importance of spatial scale in SLR assessments and the need to supplement regional projections with local insights. To date, local insights are best acquired through fine-scale SLR assessments conducted for individual wetland sites. This is exemplified by the work of Thorne et al. (2016; 2018) for several wetland sites in southern California including Upper Newport Bay, Mugu Lagoon, and Tijuana River Estuary. Detailed field collections of physical and biological data were used to parameterize the process-based WARMER model (Swanson et al. 2014) to predict SLR response for a subset area within the study sites. Our SLR response predictions corroborate their overall finding that these sites will experience conversion of mid- and high-marsh to low marsh with modest SLR projections (0.44 m) and gains of intertidal mudflat and subtidal habitat at the expense of vegetated marsh with high SLR projections (1.66 m) (Thorne et al. 2016). Specifically, projections for Upper Newport Bay by Thorne et al. (2016) indicate that 60% of the wetland area will be converted to subtidal with 1.66 m SLR and this study estimates a total of 57% subtidal under the same SLR scenario. Mugu Lagoon is estimated to become 100% intertidal mudflat with 1.66 m SLR (Thorne et al. 2016), whereas we predict the future habitat composition to be 50% intertidal mudflat and 25% subtidal. However our Mugu wetland boundary is larger than the area studied by Thorne et al. (2016) and includes more subtidal areas. Thorne et al. (2016) predict that a portion of the Tijuana River Estuary will convert to 80% mudflat and 20% subtidal, and we predict that a larger area of the estuary containing a higher initial proportion of vegetated marsh will consist of 32% mudflat and 24% subtidal with high SLR. Similarities in SLR response predictions for these three sites indicate that our approach may provide an alternative option when time and resource intensive assessments are not possible for individual wetlands or when regional efforts need to identify sites where more work should be targeted.

Accommodating all wetlands types regardless of data availability is another essential step towards a comprehensive assessment of wetland response. Our approach is designed for flexibility in model parameterization by incorporating site-specific data when available, and by using archetype or regional defaults when site data is not available. Having predicted site-level response estimates for each site revealed additional patterns in SLR response, including a positive correlation between the initial proportion of wetland habitat in each site and the potential relative wetland habitat loss, as well as the implications of data availability (Figure 1-5). The availability of in situ accretion measurements determines the relationship between wetland habitat composition and wetland loss, where sites with higher estimates of accretion supported by empirical data appear to be less at risk for future habitat loss. Our model is sensitive to the accretion parameter, and our literature review of regional accretion rates highlights that more work is needed to characterize accretion variability across marsh zones and among archetypes.

Like many SLR impacts assessment, a lack of data adds to the uncertainty of our estimates of SLR-driven habitat change. Our results indicate that efforts should be targeted towards providing additional, spatially explicit estimates of accretion, perhaps supplied by a coordinated regional or global sampling network (Osland et al. 2017; Webb et al. 2013). Such information would improve data gaps involving plant-mediated biogeomorphic feedbacks, especially considering that these processes are variable between individual wetlands and archetypes (Webb et al. 2013) and serve as broad indicators of vulnerability (Ganju et al. 2017). Although data limitations made it difficult to detect significant differences in accretion between archetypes, the archetype framework represents meaningful physical and ecological differences that will likely become more significant in the future with the support of additional empirical data. The mouth dynamics model component also represents an important, yet highly uncertain, hydrodynamic

aspect of modeling SLR response (Rodríguez et al. 2017). As evidenced by the previous lack of understanding on the distribution of intermediate estuaries (McSweeney et al. 2017) and the complexity of modeling such systems, data availability represents a major hurdle to modeling SLR impacts in certain wetland types and regions worldwide. Furthermore, advances in SLR projections and elevation datasets that reduce uncertainty and error would be beneficial to modeling SLR response, given the high model sensitivity to SLR rate and starting elevation.

This assessment is designed to inform comprehensive coastal planning by providing insights at a variety of spatial scales to aid both regional efforts and local management. Consistent, large scale methods are critical for informing regional planning and prioritization, whereas detailed methods can then be used to help inform site-specific designs (Runting et al. 2013). Our approach augments existing SLR response assessments by estimating both the risk to individual wetlands and the relative SLR response within a region. Our findings are comparable to both large-scale assessments and intensive, site-based models, making it a useful tool for coastal management. Multi-scale inferences to SLR impacts can also aid coordinated regional efforts in maintaining regional wetland composition by indicating which subregions, archetypes or individual sites have a higher relative vulnerability to SLR (Stralberg et al. 2011). Failure to include all relevant coastal wetland types can produce an incomplete picture of regional vulnerability and can obscure differences in archetype response to SLR. This is exemplified by intermediate estuaries which are globally important wetland types and require additional management considerations when planning for SLR impacts. Our approach can also be used to investigate how alterative management strategies could reduce SLR-driven habitat loss by manipulating model inputs (see SCWRP 2018 for more details). For example, expanding hypsometric curves to include suitable upland habitat adjacent to a given site can reveal reductions in habitat loss associated with

facilitating wetland migration. Raising the starting elevation of hypsometric curves could indicate the potential of thin-layer sediment augmentation as an adaptation strategy. Furthermore, modifying accretion rates can help set sediment management goals required to maintain current wetland habitat composition within a site or across the region. Overall, this approach is suitable for management applications in other regions given its ability to accommodate a diversity of wetland types and varying levels of data availability.

### 1.6 Acknowledgements

This work was conducted as part of the Southern California Wetland Recovery Project (SCWRP) aimed at preserving the remaining coastal wetlands in the southern California region (https://scwrp.org/). Our findings contributed to regional goal setting, prioritization, and management alternatives for the 2018 SCWRP Regional Strategy Update. Funding for this work was provided by grants from the U.S. Fish and Wildlife Service Landscape Conservation Cooperative (LCC) Program, the California State Coastal Conservancy, and the USC Sea Grant Trainee Program. Cheryl Doughty was also supported by a part-time graduate researcher position at the Southern California Coastal Water Research Project (SCCWRP) and by the Summer Graduate Research Mentorship Program at the University of California, Los Angeles. The SCWRP effort is an interagency consortium involving federal, state and local agencies, ranging, for example, from the U.S. Army Corps of Engineers, the CA Coastal Conservancy and the CA State Water Resources Board down to individual site management like the Tijuana River National Estuarine Research Reserve. Therefore, we would like to express our gratitude towards all who contributed to this project, especially the SCWRP's Science Advisory Panel for their input and guidance. Special thanks to Megan Cooper and Evyan Sloane at the CA Coastal Conservancy, Jeremy Lowe, Carolyn Doehring and Heather Dennis at the San Francisco Estuarine Institute

(SFEI), and John Largier at UC Davis Bodega Bay Marine Lab for their technical input and guidance. Finally, we would also like to thank Phyllis Grifman and Ruth Dudas at the USC Sea Grant Program for their continued support.

### 1.7 References

Alizad, K., Hagen, S. C., Morris, J. T., Bacopoulos, P., Bilskie, M. V., Weishampel, J. F., and Medeiros, S. C. (2016). A coupled, two-dimensional hydrodynamic-marsh model with biological feedback. *Ecological Modelling*, *327*(2016), 29–43. http://doi.org/10.1016/j.ecolmodel.2016.01.013

Alizad, K., Hagen, S. C., Morris, J. T., Medeiros, S. C., Bilskie, M. V, and Weishampel, J. F. (2016). Coastal wetland response to sea-level rise in a fluvial estuarine system. *Earth's Future*, *4*, 483–497. http://doi.org/10.1002/2016EF000385

Anisfeld, S. C., Cooper, K., and Kemp, A. (2017). Upslope development of a tidal marsh as a function of upland land use. *Global Change Biology*, *23*(2), 755–766. http://doi.org/10.1111/gcb.13398

Bamber, J., and Riva, R. (2010). The sea level fingerprint of recent ice mass fluxes. *The Cryosphere*, *4*, 621–627. http://doi.org/10.5194/tc-4-621-2010

Behrens, D. K., Bombardelli, F. A., Largier, J. L., and Twohy, E. (2013). Episodic closure of the tidal inlet at the mouth of the Russian River — A small bar-built estuary in California. *Geomorphology*, *189*(2013), 66–80. http://doi.org/10.1016/j.geomorph.2013.01.017

Behrens, D. K., Brennan, M., and Battalio, B. (2015). A quantified conceptual model of inlet morphology and associated lagoon hydrology. *Shore and Beach*, *83*(3), 33–42.

Cahoon, D. R., Hensel, P. F., Spencer, T., Reed, D. J., McKee, K. L., and Saintilan, N. (2006). Coastal wetland vulnerability to relative sea-level rise: wetland elevation trends and process controls. In *Ecological Studies: Wetlands and Natural Resource Management* (Vol. 190, pp. 271–292). http://doi.org/10.1007/978-3-540-33187-2_12

California Coastal Commission. (2015). *Sea Level Rise Policy Guidance: Interpretive Guidelines for Addressing Sea Level Rise in Local Coastal Programs. California Coastal Commission: San Francisco, California.*

Cazenave, A., and Cozannet, G. Le. (2013). Sea level rise and its coastal impacts. *Earth's Future*, *2*, 15–34. http://doi.org/10.1002/2013EF000188

Church, J. A., Gregory, J. M., Cazenave, A., Gregory, J. M., Jevrejeva, S., Levermann, A., … Good, P. (2013). Sea Level Change. *Climate Change 2013: The Physical Science Basis. Contribution of Working Group I to the Fifth Assessment Report of the Intergovernmental Panel on Climate Change*, 1–8. http://doi.org/10.1017/CBO9781107415324.026

Clough, J. S., Park, R. A., Propato, M., Polaczyk, A., and Fuller, R. (2012). *SLAMM 6.2 Technical documentation. Warren Pinnacle Consulting, Waitsfield, Vermont.*

Craft, C., Clough, J., Ehman, J., Jove, S., Park, R., Pennings, S., … Machmuller, M. (2009).

Forecasting the effects of accelerated sea-level rise on tidal marsh ecosystem services. *Frontiers in Ecology and the Environment*, *7*(2), 73–78. http://doi.org/10.1890/070219

Donnelly, J. P., and Bertness, M. D. (2001). Rapid shoreward encroachment of salt marsh cordgrass in response to accelerated sea-level rise. *Proceedings of the National Academy of Sciences of the United States of America*, *98*(25), 14218–14223. http://doi.org/10.1073/pnas.251209298

Dürr, H. H., Laruelle, G. G., van Kempen, C. M., Slomp, C. P., Meybeck, M., and Middelkoop, H. (2011). Worldwide Typology of Nearshore Coastal Systems: Defining the Estuarine Filter of River Inputs to the Oceans. *Estuaries and Coasts*, *34*(3), 441–458. http://doi.org/10.1007/s12237-011-9381-y

Fagherazzi, S., Kirwan, M. L., Mudd, S. M., Guntenspergen, G. R., Temmerman, S., Rybczyk, J. M., … Clough, J. (2012). Numerical models of salt marsh evolution: Ecological, geormorphic, and climatic factors. *Review of Geophysics*, *50*(1), 1–28. http://doi.org/10.1029/2011RG000359

FitzGerald, D. M., Fenster, M. S., Argow, B. A., and Buynevich, I. V. (2008). Coastal impacts due to sea-level rise. *Annual Review of Earth and Planetary Sciences*, *36*(1), 601–647. http://doi.org/10.1146/annurev.earth.35.031306.140139

Ganju, N. K., Defne, Z., Kirwan, M. L., Fagherazzi, S., D'Alpaos, A., and Carniello, L. (2017). Spatially integrative metrics reveal hidden vulnerability of microtidal salt marshes. *Nature Communications*, *8*, 14156. http://doi.org/10.1038/ncomms14156

Gilmer, B., Brenner, J., and Sheets, J. (2012). *Informing conservation planning using sea-level rise and storm surge impact estimates in the Galveston Bay and Jefferson County, Texas area*. The Nature Conservancy.

Gittman, R. K., Fodrie, F. J., Popowich, A. M., Keller, D. A., Bruno, J. F., Currin, C. A., … Piehler, M. F. (2015). Engineering away our natural defenses: An analysis of shoreline hardening in the US. *Frontiers in Ecology and the Environment*, *13*(6), 301–307. http://doi.org/10.1890/150065

Gornitz, V. (1991). Global coastal hazards from future sea level rise. *Palaeogeography, Palaeoclimatology, Palaeoecology (Global and Planetary Change)*, *3*(4), 379–398. http://doi.org/10.1016/0921-8181(91)90118-G

Griggs, G., Árvai, J., Cayan, D., DeConto, R., Fox, J., Fricker, H., … Group), (California Ocean Protection Council Science Advisory Team Working. (2017). *Rising Seas in California: An Update on Sea-Level Rise Science.* Retrieved from http://www.opc.ca.gov/webmaster/ftp/pdf/docs/rising-seas-in-california-an-update-on-sea-level-rise-science.pdf

Haines, P. E., and Thom, B. G. (2007). Climate Change Impacts on Entrance Processes of Intermittently Open/Closed Coastal Lagoons in New South Wales, Australia. *Journal of Coastal Research, SI 50*(Proceedings of the 9th International Coastal Symposium), 242–246.

King, M., Keshin, M., Whitehouse, P., Thomas, I., Milne, G., and Riva, R. (2012). Regional biases in absolute sea-level estimates from tide gauge data due to residual unmodeled vertical land movement. *Geophysical Research Letters*, *39*(L14604), 1–5.

http://doi.org/10.1029/2012GL052348

Kirwan, M. L., Guntenspergen, G. R., D'Alpaos, A., Morris, J. T., Mudd, S. M., and Temmerman, S. (2010). Limits on the adaptability of coastal marshes to rising sea level. *Geophysical Research Letters*, *37*(23), L23401. http://doi.org/10.1029/2010GL045489

Kirwan, M. L., Temmerman, S., Skeehan, E. E., Guntenspergen, G. R., and Faghe, S. (2016). Overestimation of marsh vulnerability to sea level rise. *Nature Climate Change*, *6*(3), 253–260. http://doi.org/10.1038/nclimate2909

Klein, R., and Nicholls, R. J. (1999). Assessment of Coastal Vulnerability to Climate Change. *Ambio*, *28*(2), 182–187.

Lentz, E. E., Thieler, E. R., Plant, N. G., Stippa, S. R., Horton, R. M., and Gesch, D. B. (2016). Evaluation of dynamic coastal response to sea-level rise modifies inundation likelihood. *Nature Climate Change*, *6*, 696–700. http://doi.org/10.1038/nclimate2957

McSweeney, S. L., Kennedy, D. M., Rutherfurd, I. D., and Stout, J. C. (2017). Intermittently Closed/Open Lakes and Lagoons: Their global distribution and boundary conditions. *Geomorphology*, *292*, 142–152. http://doi.org/10.1016/j.geomorph.2017.04.022

Morris, J. T., Sundareshwar, P. V., Nietch, C. T., Kjerfve, B. B., and Cahoon, D. R. (2002). Responses of coastal wetlands to rising sea level. *Ecology*, *83*(10), 2869–2877. http://doi.org/10.2307/3072022

Mueller, P., Jensen, K., and Megonigal, J. P. (2016). Plants mediate soil organic matter decomposition in response to sea level rise. *Global Change Biology*, *22*(1), 404–414. http://doi.org/10.1111/gcb.13082

National Research Council. (2012). *Sea-level rise for the coasts of California, Oregon, and Washington: Past, present, and future*. Washington, DC: National Academy Press. http://doi.org/10.17226/13389

Nicholls, R. J. (2004). Coastal flooding and wetland loss in the 21st century: Changes under the SRES climate and socio-economic scenarios. *Global Environmental Change*, *14*(1), 69–86. http://doi.org/10.1016/j.gloenvcha.2003.10.007

Nicholls, R. J., Hoozemans, F. M. J., and Marchand, M. (1999). Increasing flood risk and wetland losses due to global sea-level rise: regional and global analyses. *Global Environmental Change*, *9*(S1), S69–S87. http://doi.org/10.1016/S0959-3780(99)00019-9

Osland, M. J., Griffith, K. T., Larriviere, J. C., Feher, L. C., Cahoon, R., Enwright, N. M., … Consulting, G. (2017). Assessing coastal wetland vulnerability to sea-level rise along the northern Gulf of Mexico coast: Gaps and opportunities for developing a coordinated regional sampling network. *PLoS ONE*, *12*(9), e0183431. http://doi.org/10.1371/journal.pone.0183431

Passeri, D. L., Hagen, S. C., Medeiros, S. C., Bilskie, M. V, Alizad, K., and Wang, D. (2015). The dynamic effects of sea level rise on low-gradient coastal landscapes: A review. *Earth's Future*, *3*, 159–181. http://doi.org/10.1002/2015EF000298

Pontee, N. (2013). Defining coastal squeeze: A discussion. *Ocean and Coastal Management*, *84*, 204–207. http://doi.org/10.1016/j.ocecoaman.2013.07.010

Preston, B. L., Yuen, E. J., and Westaway, R. M. (2011). Putting vulnerability to climate change on the map: A review of approaches, benefits, and risks. *Sustainability Science*, *6*(2), 177–202. http://doi.org/10.1007/s11625-011-0129-1

PWA. (2003). *Management of Lake Earl Lagoon water elevations. PWA Ref# 1678.00*.

Rhein, M., Rintoul, S. R., Aoki, S., Campos, E., Chambers, D., Feely, R. A., … Wang, F. (2013). Observations: Ocean. In: Climate Change 2013: The Physical Science Basis. Contribution of Working Group I to the Fifth Assessment Report of the Intergovernmental Panel on Climate Change. http://doi.org/10.1017/CBO9781107415324.010

Rich, A., and Keller, E. a. (2013). A hydrologic and geomorphic model of estuary breaching and closure. *Geomorphology*, *191*, 64–74. http://doi.org/10.1016/j.geomorph.2013.03.003

Riva, R. E. M., Bamber, J. L., Lavallée, D. A., and Wouters, B. (2010). Sea-level fingerprint of continental water and ice mass change from GRACE. *Geophysical Research Letters*, *37*(19), 1–6. http://doi.org/10.1029/2010GL044770

Rodríguez, J. F., Saco, P. M., Sandi, S., Saintilan, N., and Riccardi, G. (2017). Potential increase in coastal wetland vulnerability to sea-level rise suggested by considering hydrodynamic attenuation effects. *Nature Communications*, *8*(16094), 1–12. http://doi.org/10.1038/ncomms16094

Runting, R. K., Wilson, K. A., and Rhodes, J. R. (2013). Does more mean less? The value of information for conservation planning under sea level rise. *Global Change Biology*, *19*(2), 352–363. http://doi.org/10.1111/gcb.12064

SCWRP. (2018). *Wetlands on the Edge: The Future of Southern California's Wetlands: Regional Strategy 2018 prepared by the Southern California Wetlands Recovery Project*. California State Coastal Conservancy. Oakland, CA.

Spencer, T., Schürch, M., Nicholls, R. J., Hinkel, J., Lincke, D., Vafeidis, A. T. T., … Brown, S. (2016). Global coastal wetland change under sea-level rise and related stresses: The DIVA Wetland Change Model. *Global and Planetary Change*, *139*, 15–30. http://doi.org/10.1016/j.gloplacha.2015.12.018

Stammer, D., Cazenave, A., Ponte, R. M., and Tamisiea, M. E. (2013). Causes for Contemporary Regional Sea Level Changes. *Annual Review of Marine Science*, *5*, 21–46. http://doi.org/10.1146/annurev-marine-121211-172406

Stein, E. D., Cayce, K., Salomon, M., Bram, D. L., Grossinger, R., and Dark, S. (2014). Wetlands of the Southern California coast: Historical extent and change over time. *Southern California Coastal Water Research Project Technical Report 826*, 1–50.

Stralberg, D., Brennan, M., Callaway, J. C., Wood, J. K., Schile, L. M., Jongsomjit, D., … Crooks, S. (2011). Evaluating tidal marsh sustainability in the face of sea-level rise: a hybrid modeling approach applied to San Francisco Bay. *PloS One*, *6*(11), e27388. http://doi.org/10.1371/journal.pone.0027388

Swanson, K. M., Drexler, J. Z., Schoellhamer, D. H., Thorne, K. M., Casazza, M. L., Overton, C. T., … Takekawa, J. Y. (2014). Wetland Accretion Rate Model of Ecosystem Resilience (WARMER) and Its Application to Habitat Sustainability for Endangered Species in the

San Francisco Estuary. *Estuaries and Coasts*, *37*(2), 476–492. http://doi.org/10.1007/s12237-013-9694-0

Swenson, R. O. (1999). The ecology, behavior, and conservation of the tidewater goby, Eucyclogobius newberryi. *Environmental Biology of Fishes*, *55*, 99–114. http://doi.org/10.1023/a:1007478207892

Thorne, K., Macdonald, G., Guntenspergen, G., Ambrose, R., Buffington, K., Dugger, B., … Takekawa, J. (2018). U. S. Pacific coastal wetland resilience and vulnerability to sea-level rise. *Science Advances*, *4*(February), 1–11. http://doi.org/10.1126/sciadv.aao3270

Thorne, K., MacDonald, G. M., Takekawa, J. Y., Ambrose, R. A., Barnard, P., Guntenspergen, G. R., … Powelson, K. (2016). Climate change effects on tidal marshes along a latitudinal gradient in California. *U.S. Geological Survey Open-File Report 2016-1125*, 75 p. http://doi.org/10.3133/ofr20161125.

Vafeidis, A. T., Nicholls, R. J., Mcfadden, L., Tol, R. S. J., Hinkel, J., Spencer, T., … Klein, R. J. T. (2008). A New Global Coastal Database for Impact and Vulnerability Analysis to Sea-Level Rise. *Journal of Coastal Research*, *24*(4), 917–924. Retrieved from http://www.jstor.org/stable/40065185

Webb, E. L., Friess, D. A., Krauss, K. W., Cahoon, D. R., Guntenspergen, G. R., and Phelps, J. (2013). A global standard for monitoring coastal wetland vulnerability to accelerated sea-level rise. *Nature Climate Change*, *3*, 458–465. http://doi.org/10.1038/nclimate1756

Williams, P., and Cuffe, C. (1995). The management implications of the potential for closure of Bolinas Lagoon. *Oceanographic Literature Review*, *42*(6), 451 p.

Wong, P. P., Losada, I. J., Gattuso, J. P., Hinkel, J., Khattabi, A., McInnes, K. L., … Sallenger, A. (2014). Coastal Systems and Low-Lying Areas. In C. B. Field, V. R. Barros, D. J. Dokken, K. J. Mach, M. D. Mastrandrea, T. E. Bilir, … L. L. White (Eds.), *Climate Change 2014: Impacts, Adaptation, and Vulnerability. Report of the Intergovernmental Panel on Climate Change* (pp. 361–409). Cambridge University Press, Cambridge, United Kingdom and New York, NY, USA.

Zedler, J. B. (1982). The ecology of southern California coastal salt marshes: a community profile. *U.S. Fish and Wildlife Service, Biological Servces Program, Washington, D.C. FWS/OBS-81/54*, 110 p.

Zedler, J. B. (1996). Coastal mitigation in Southern California: The need for a regional restoration strategy. *Ecological Applications*, *6*(1), 84–93. http://doi.org/10.2307/2269555

## 1.8 Supplemental Materials

**Table S1-1. Records of published accretion data from the literature review. This supplemental info is provided as an excel file:**

https://onlinelibrary.wiley.com/action/downloadSupplement?doi=10.1111%2Fgcb.14429&file=gcb14429-sup-0001-TableS1.xlsx

**Table S1-2. Example z* bin range upper limits corresponding to wetland habitats under current, 2050 and 2100 conditions. Changes to z* are determined by site-specific changes in water level estimated in our analysis. Example values shown for the Aliso Canyon estuary in San Diego county. Z* for this site is based on the Newport Beach, CA NOAA tidal station.**

| | Z* Range Upper Limit | | |
|---|---|---|---|
| **Marsh Zone** | **Current** | **2050** | **2100** |
| Subtidal | -1.05 | -0.38 | 1.16 |
| Intertidal Mudflat | 0.00 | .66 | 2.19 |
| Low Marsh | 0.72 | 1.38 | 2.91 |
| Mid Marsh | 1.00 | 1.66 | 3.19 |
| High Marsh | 1.67 | 2.33 | 3.86 |
| Transition | 2.6 | 3.33 | 4.86 |

## CHAPTER 2: Mapping Coastal Wetland Biomass from High Resolution Unmanned Aerial Vehicle (UAV) Imagery[2]

### 2.1 Abstract

Salt marsh productivity is an important control of resiliency to sea level rise. However, our understanding of how marsh biomass and productivity vary across fine spatial and temporal scales is limited. Remote sensing provides a means for characterizing spatial and temporal variability in marsh aboveground biomass, but most satellite and airborne sensors have limited spatial and/or temporal resolution. Imagery from unmanned aerial vehicles (UAVs) can be used to address this data gap. We combined seasonal field surveys and multispectral UAV imagery collected using a DJI Matrice 100 and Micasense Rededge sensor from the Carpinteria Salt Marsh Reserve in California, USA to develop a method for high-resolution mapping of aboveground saltmarsh biomass. UAV imagery was used to test a suite of vegetation indices in their ability to predict aboveground biomass (AGB). NDVI provided the strongest correlation to aboveground biomass for each season and when seasonal data were pooled, though seasonal models (e.g. spring, $r^2$ = 0.67; rmse = 344 g $m^{-2}$) were more robust than the annual model ($r^2$ = 0.36; rmse = 496 g $m^{-2}$). The NDVI aboveground biomass estimation model (AGB = 2428.2 × NDVI + 120.1) was then used to create maps of biomass for each season. Total site wide aboveground biomass ranged from 147 Mg to 205 Mg and was highest in the spring, with an average of 1222.9 g $m^{-2}$. Analysis of spatial patterns in ABG demonstrated that ABG was highest in intermediate elevations that ranged from 1.6–1.8 m NAVD88. This UAV-based approach can be used aid the investigation of biomass dynamics in wetlands across a range of spatial scales.

[2] This chapter was published as Doughty C, Cavanaugh K. Mapping Coastal Wetland Biomass from High Resolution Unmanned Aerial Vehicle (UAV) Imagery. Remote Sens. 2019;11(5):540. It is reproduced here with minor formatting changes to comply with University of California dissertation specifications.

## 2.2 Introduction

Coastal wetlands, despite being characteristically dynamic ecosystems equipped to deal with a variety of stressors, are threatened by environmental change. Environmental stressors, such as inundation, salinity and nutrient availability, influence the overall productivity of coastal wetlands (Day et al. 2008). Wetland productivity is mediated by complex biogeomorphic feedbacks, whereby plants accumulate organic matter and trap inorganic sediment to maintain their elevation in relation to varying tidal levels and other stressors (Morris et al. 2002). The ability of coastal wetlands to remain productive and maintain elevation through accretion is a key factor in overall wetland resilience to environmental change (Pennings et al. 2005; Kirwan and Guntenspergen 2015). As a result of these complex biophysical interactions, coastal wetlands exhibit high spatial and temporal variability in characteristics such as plant community zonation and seasonal productivity.

Climate change threatens to disrupt the normative patterns and processes by exacerbating environmental stressors, which could have cascading effects on biological response, wetland productivity, and ultimately, resilience (Kirwan and Megonigal 2013). Climate change is expected to accelerate sea level rise, alter precipitation patterns and intensify coastal storms (Scavia et al. 2002), however, the full extent of impacts remains to be seen (Osland et al. 2016). Two likely consequences include changes to peak biomass and to phenology of plant growth (Buffington et al. 2018), but response will be highly variable among wetland sites, zones and species (Janousek et al. 2016; Goodman et al. 2018). Monitoring the current status and past trends in coastal wetland dynamics may provide valuable insights into future response. Specifically, understanding how coastal wetland biomass and productivity change over space and time can indicate vegetation stress

and help establish a threshold for resilience to environmental drivers (Klemas 2013; Buffington et al. 2018).

Satellite and aerial remote sensing have improved our ability to map and monitor the heterogeneous and dynamic nature of coastal wetlands (Klemas 2009). The high temporal frequency achieved by repeat coverage of satellite remote sensing has led to consistent, global, long-term data archives that can be used to detect changes in wetlands over time (Ozesmi and Bauer 2002; E. Adam et al. 2010; Mishra and Ghosh 2015). In addition, these methodologies can reveal large-scale patterns in productivity through the remote quantification of biomass (Byrd et al. 2014). Biomass estimation in optical remote sensing often uses spectral information in the form of vegetation indices (VIs) (Mutanga and Skidmore 2004). Vegetation indices summarize the reflectance occurring within visible and near-infrared wavelengths that are sensitive to biomass (Klemas 2013; Xue and Su 2017), while also controlling for variation caused by soil and atmospheric interference (Mutanga and Skidmore 2004). The correlation among *in situ* biomass measurements and VIs, such as the normalized difference vegetation index (NDVI), provide a basis for biomass estimation (Zhang et al. 1997; Adam and Mutanga 2012; Klemas 2013). This approach has been demonstrated successfully in numerous satellite applications, including the characterization of biomass dynamics over several decades in relation to environmental drivers in both Pacific (Buffington et al. 2018), and Atlantic coast marshes (O'Donnell and Schalles 2016).

However, there are a number of limitations and challenges associated with estimating coastal wetland biomass from multispectral imagery (Gallant 2015). Among these are tradeoffs in spatial, temporal, and radiometric resolution of satellite imagery that may obscure ecologically relevant patterns and processes occurring at fine scales. Limited spatial and temporal resolution is particularly an issue for coastal wetlands, as they exhibit variability in species composition,

biomass, productivity, and other characteristics on fine space and time scales (Shanmugam 2013). Steep environmental gradients and short ecotones can make it difficult to discriminate many wetland characteristics from moderate resolution (10 – 30 m) imagery (Zomer et al. 2009). In addition, the spectral response of wetland vegetation is convoluted with the reflectance emitted from underlying soils, water, and non-photosynthetic vegetation, and is also altered by water content in plant tissues and the structure of plant canopies (Schmidt and Skidmore 2003; Kearney et al. 2009). Therefore, patch size and inundation are key concerns in using satellite remote sensing to estimate biomass in coastal wetlands (Byrd et al. 2014). As a result, most algorithms that have been developed for biomass estimation are site specific and, in some situations, it may not be possible to accurately estimate aboveground biomass from multispectral imagery.

Unmanned aerial vehicles can improve the mapping and monitoring of biomass and productivity in coastal wetlands. UAVs offer a cost-effective, flexible approach with the ability to provide the finer spatial and temporal resolution needed to adequately identify and measure ecosystem change (Whitehead et al. 2014a; Klemas 2015a; Manfreda et al. 2018). UAV applications for ecological research are still relatively novel, especially in coastal systems (Hugenholtz 2012; Vincent et al. 2014; Whitehead et al. 2014a). To date, applications include geomorphological and topographical mapping (Delacourt et al. 2009; C. H. Hugenholtz et al. 2013; Turner et al. 2016), as well as coastal hazard and erosion detection (Chong 2007; Pereira et al. 2009). UAVs have demonstrated great potential in discriminating and mapping a variety of vegetation classes and species (Klemas 2015a), exemplified by recent research in mapping invasive salt marsh species (Jensen et al. 2011; Samiappan et al. 2016), discriminating mangrove species (Ruwaimana et al. 2018), and distinguishing salt marsh structure from underlying terrain (Kalacska et al. 2017; Meng et al. 2017a). Biomass quantification using UAVs has been successful

in a small number of case studies in coastal wetlands. For instance, high-resolution UAV imagery has been used to quantify aboveground biomass and fine-scale spatial patterns of *Spartina*, an invasive cordgrass in China (Zhou et al. 2018). UAVs have also been used to successfully quantify height and aboveground biomass in mangrove forests in Malaysia (Otero et al. 2018). UAV applications specific to vegetation dynamics in coastal wetland systems are currently limited, but examples drawn from agricultural applications highlight the potential for monitoring the health, productivity and biomass of vegetation (Sugiura et al. 2005; Berni et al. 2009; Whitehead et al. 2014a; Whitehead et al. 2014b; Tagle et al. 2017).

The aim of this study was to develop a UAV-based aboveground biomass estimation model for a coastal salt marsh in southern California. An initial objective was to validate UAV reflectance retrievals using *in situ* measures of canopy reflectance to ensure proper image acquisition and post-processing. We used field data to test the ability of several vegetation indices derived from the UAV imagery to accurately model aboveground biomass. By conducting this effort repeatedly over the course of an annual growing cycle, we examined the influence of season in our ability to model aboveground biomass. The UAV-based estimation model was then used to create ultra-high resolution maps of salt marsh aboveground biomass over the annual growing cycle, allowing us to detect fine-scale spatial patterns within the coastal wetland and to characterize intra-annual biomass dynamics. Ultimately, this study highlights the feasibility of UAVs for quantifying biomass dynamics, filling a critical gap in our ability to track coastal wetland phenology at fine spatial and temporal scales.

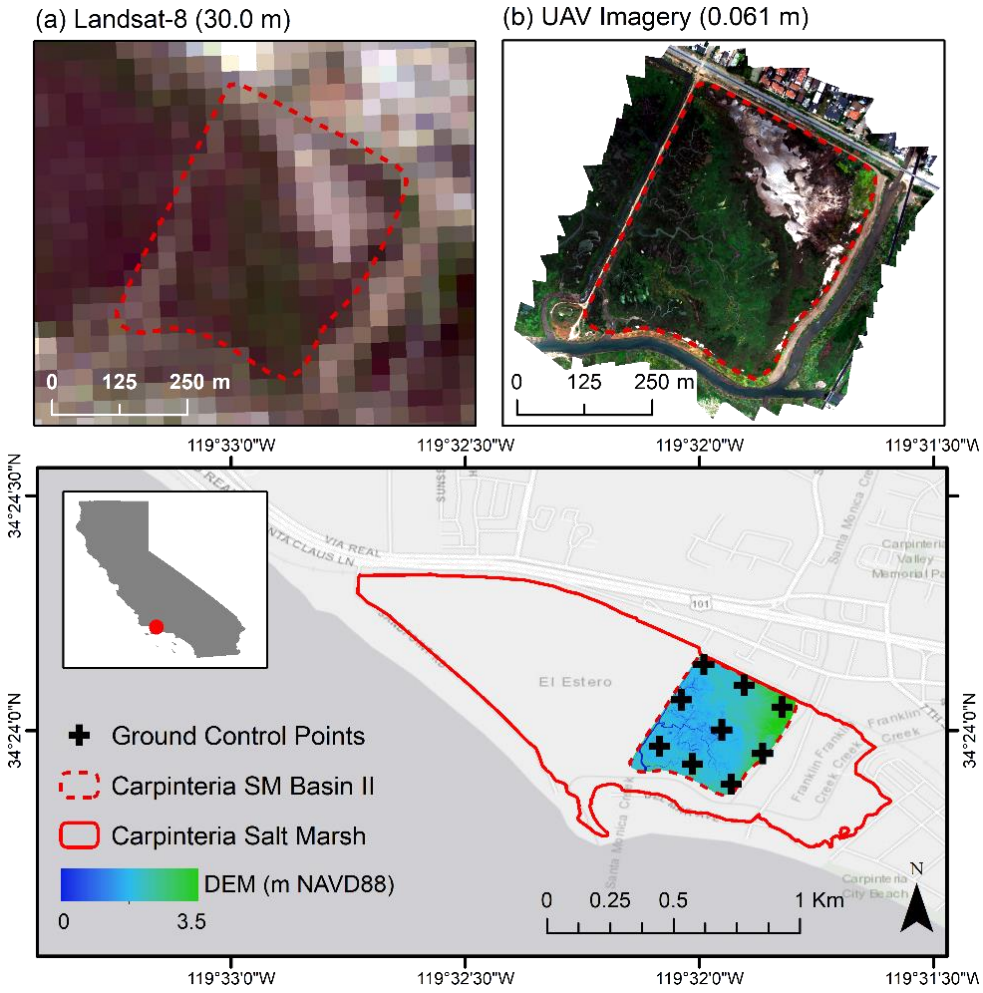


**Figure 2-1. The Carpinteria Salt Marsh Reserve located in Santa Barbara County, CA, USA. Landsat-8 (a) and UAV imagery (b) is shown in true color for a basin of the study site for comparison. Basemap is courtesy of ESRI.**

## 2.3 Materials and Methods

### *2.3.1 Site Description*

We conducted seasonal UAV surveys and field sampling at the Carpinteria Salt Marsh Reserve (34°24′4.3″N, 119°32′16.4″W), Basin II, in Santa Barbara County, CA, USA between February and November 2018 (

Figure 2-1). This site contains 93 hectares of wetland and channel habitats, in addition to transitional uplands, with relatively shallow elevations grading from −1 m to 3 m above mean sea level. Tidal statistics are characteristic of a perched system with mean sea levels ~0.25 m higher

and ~33% reduced tidal range within the marsh relative to the open coast (Sadro et al. 2007). Climate conditions are Mediterranean temperate with dry, hot summers. Mean temperatures at the site range from 24°C maximum in August and 6 °C minimum in January, with a mean annual precipitation of 38 cm.

The intertidal plant community consists of annual and perennial herbs and grasses. This site is dominated by *Salicornia pacifica* (pickleweed), *Jaumea carnosa* (marsh jaumea), and *Distichlis littoralis* (shore grass). Other species present include *Cuscuta salina* (saltmarsh dodder), *Frankenia salina* (alkali heath), *Limonium californicum* (marsh rosemary), *Distichlis spicata* (salt grass) and *Suaeda calceoliformis* (horned sea blite).

### *2.3.2 Field Data Collection*

#### *2.3.2.1 Multispectral UAV Image Data*

We conducted field campaigns each season for one year on 23 February 2018 (winter), 24 May 2018 (spring), 19 July 2018 (summer) and 13 November 2018 (fall). Sky conditions on flight days ranged from overcast to clear and tidal levels ranged from 0.24 to 1.29 m NAVD88 (Table S2-1). We performed UAV surveys using a DJI Matrice 100 quadcopter (DJI, Nanshan, Shenzhen, China). The DJI Matrice 100 is a fully programmable multirotor platform that can be customized with different sensors for specific applications, unlike other off-the-shelf models, like the DJI Phantom. The payload included a Micasense Rededge multispectral camera and a downwelling light sensor (DLS), or irradiance sensor (Micasense, Seattle, WA). However, DLS data were ultimately not included in image processing because it decreased radiometric performance and lead to an overestimation of reflectance in the resulting UAV orthomosaic (Figure S2-1). The Rededge multispectral camera used in this study captures five spectral bands: blue (475 nm, 20

nm bandwidth), green (560 nm, 20 nm bandwidth), red (668 nm, 10 nm bandwidth), red edge (717 nm, 10 nm bandwidth), and the near-infrared (840 nm, 40 nm bandwidth).

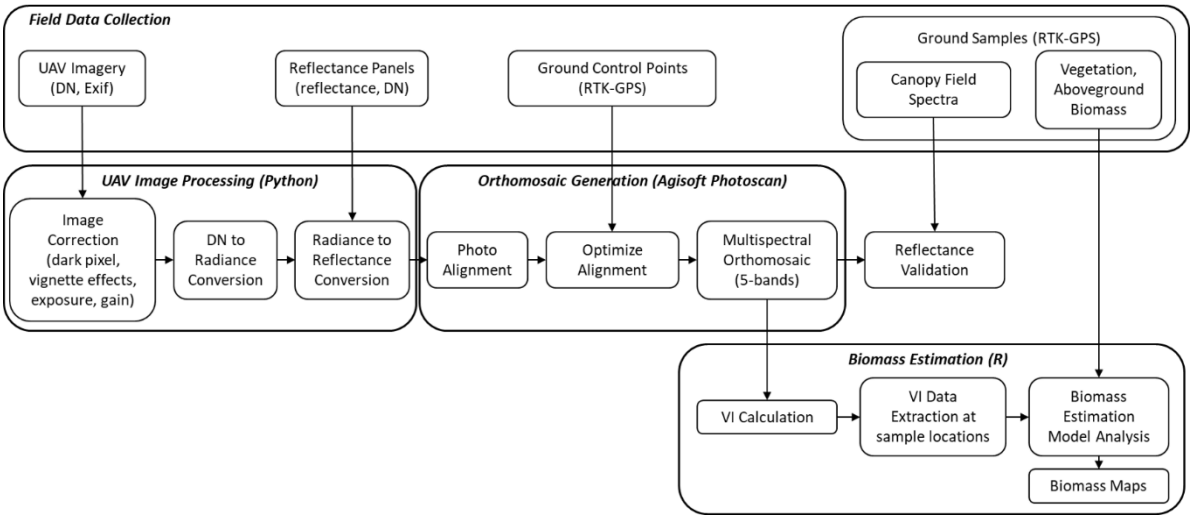


**Figure 2-2. Overview of data collection and processing workflow.**

Prior to UAV flight, we deployed ground control place markers (GCPs) with RTK-GPS to help with georeferencing and photo alignment during image processing (Figure 2-2). We performed RTK-GPS measurements at GCP centers with an Arrow Gold RTK-GPS with ~3 cm horizontal accuracy and ~5 cm vertical accuracy (EOS Positioning System, Terrebonne, QC, Canada). We also captured images of calibrated panels with known reflectance (Micasense, Seattle, WA) using the Rededge sensor before and after each flight to aid in radiometric conversion.

We planned UAV flights using the Atlas Flight software (Micasense, Seattle, WA). We conducted flights at an altitude of 90 m above ground level, an airspeed of 7 m $s^{-1}$, and with image overlap (frontlap and sidelap) set to 75%. With these specifications, average flight time per battery set was approximately 30 minutes, requiring up to 2 flights to cover a 0.35 $km^2$ study area (Table S2-1).

#### *2.3.2.2 Vegetation Sampling*

We conducted field sampling of salt marsh vegetation during each season along an elevational gradient which captured a representative subset of dominant species at the site (Figure 2, *Ground Samples*). The elevational gradient ranged from 0 m NAVD88 at the southwest corner of basin II to 3.5 m NAVD88 at the northeast corner of basin II (Figure 2-1). Along elevational transects, we sampled 0.25-$m^2$ plots (n = 15) placed approximately 10 m apart. We captured plot locations with submeter accuracy using the RTK-GPS. We also measured canopy reflectance with an ASD Handheld 2 Spectrometer (Malvern Panalytical, Malvern, UK). Reflectance spectra were sampled every 1 nm over 325–1075 nm using a 25 field of view foreoptics. We took ten readings at nadir at a height of approximately 50 cm for a 25 cm diameter ground field of view and averaged them together to create a single spectral profile for each plot. Following spectral measurements, we harvested all aboveground biomass above the soil level within the sampling plot. In the laboratory, aboveground biomass samples were massed for wet weight (g) then dried at 50°C for one week or until constant mass was achieved to obtain dry weight (g).

### *2.3.3 Multispectral UAV Image Processing*

We conducted preprocessing of UAV images to correct images for dark pixels, vignette effects, exposure and gain (Figure 2-2). Corrected images were then converted from raw digital number (DN) to radiance and from radiance to reflectance using an average radiance-to-reflectance conversion factor calculated by averaging the preflight and postflight calibration panel images. Image correction and radiometric conversion were conducted in Python 3.6 (Python Software Foundation, Amsterdam, the Netherlands) using scripts adapted from Micasense for batch processing (Doughty 2019). UAV images processed to reflectance were then imported to Agisoft Photoscan Pro v1.4 for orthomosaic generation (Agisoft, St. Petersburg, Russia). During this

process, photos were aligned to the highest accuracy setting and optimized using the GCPs with RTK-GPS coordinates. We took additional steps to calibrate image color and white balance to ensure brightness consistency within each band in the resulting orthomosaic. Final processing steps in Photoscan included the creation of a dense point cloud and a digital elevation model (DEM) to facilitate mosaicking. Final orthomosaics for each season cover the Carpinteria Salt Marsh Basin II (Figure 2-1) at ground resolutions averaging at approximately 6.1 cm pixel$^{-1}$ (Table S2-1).

We compared reflectance measured from the UAV imagery to the *in situ* canopy reflectance measurements to validate data collection and processing. To facilitate comparison, field spectra were first convolved using a weighted average filter to correspond to the bands measured by the Rededge sensor (Chen et al. 2015). We processed field spectra in Python 3.6. We extracted reflectance data for each band of the multispectral orthomosaics using the R raster package v2.7. Mean reflectance estimates were extracted for a circular area surrounding each sampling plot which, accounted for quadrat width (25 cm) and the horizontal error of both the RTK-GPS (~2.5 cm) and the orthomosaic (4.3 – 11.9 cm; Table S2-1). Comparison of UAV and field reflectance for each of the five bands was conducted for pooled seasonal data using simple linear regression in R (R Foundation for Statistical Computing, Vienna, Austria).

### *2.3.4 UAV-Based Biomass Estimation*

We tested a suite of vegetation indices for their ability to estimate aboveground biomass (

Table 2-1). We selected vegetation indices (VIs) based on the spectral bands present in the Micasense Rededge sensor and to align with common VIs used with multispectral satellite imagery. The UAV-based reflectance estimates corresponding to each sampling plot were then used to calculate average VI for each plot. We compared plot aboveground biomass to VI for

pooled seasonal data, as well as separately for each season, using simple linear regression from the R stats package v3.4.2. Linear regression analysis was selected because data derived from the orthomosaics did not exhibit pixel saturation.

**Table 2-1. Broad band vegetation indices used in UAV remote sensing.**

| Index | Description | Equation | Reference |
|---|---|---|---|
| CIgreen | Chlorophyll Index Green | $\frac{NIR}{GREEN} - 1$ | (Gitelson et al. 2005) |
| CIrededge | Chlorophyll Index Rededge | $\frac{NIR}{Rededge} - 1$ | (Gitelson, Merzlyak, et al. 1996) |
| EVI2 | Enhanced Vegetation Index | $2.5 * \frac{NIR - RED}{NIR + 2.4 * RED + 1}$ | (Jiang et al. 2008) |
| GNDVI | Green Normalized Difference VI | $\frac{NIR - GREEN}{NIR + GREEN}$ | (Gitelson, Kaufman, et al. 1996) |
| NRDE | Rededge Normalized Difference VI | $\frac{NIR - Rededge}{NIR + Rededge}$ | (Barnes et al. 2000) |
| NDVI | Normalized Difference Vegetation Index | $\frac{NIR - RED}{NIR + RED}$ | (Rouse et al. 1974) |

We selected the vegetation index with the highest performing biomass estimation model to create biomass maps for each season. We chose a single annual model based on the seasonally pooled data to allow for comparison across seasons. To create biomass maps, first, we created VI maps from the 5-band multispectral orthomosaics using raster band math functions in R. Then, we applied the biomass estimation model to the VI maps to create biomass maps. Additional raster processing included the masking of water and resampling so that resulting biomass maps conform to a 1-m pixel resolution. Water masks were created using a supervised classification in ENVI (Harris Geospatial Solutions, Boulder, CO). All raster processing was conducted in R.

Further investigation of annual verses seasonal models was performed for the highest performing VI. We used a partial F-test to compare the reduced model (pooled seasonal data) and the full model (including season as a predictor variable). All statistical analysis was performed in R.

### *2.3.5 Spatial and Temporal Analysis of Biomass*

We used the UAV-derived maps of biomass to estimate the mean aboveground biomass density and total aboveground biomass for the site in each season. We tested seasonal differences using a two-way ANOVA. Data were square root-transformed to meet assumptions of normality and homogeneity of variances as needed. Biomass maps were also compared to 1-$m^2$ resolution digital elevation models (DEMs) available from the NOAA-CA Coastal Conservancy Coastal LiDAR project 2009–2013. Biomass and elevation data were extracted for each pixel along an elevational gradient from the SW corner to the NE corner of Basin II (Figure 2-1). The correlation of biomass and elevation was tested using a parabolic linear regression in R.

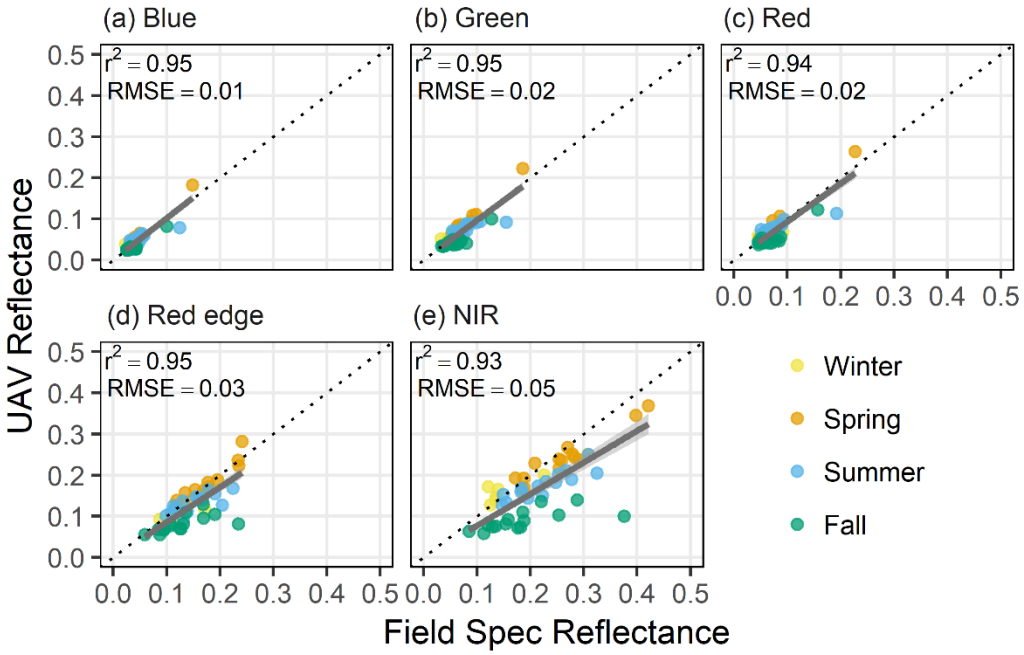

**Figure 2-3. Reflectance validation of UAV reflectance using in situ canopy reflectance for (a) blue, (b) green, (c) red, (d) rededge and (e) NIR bands.**

## 2.4 Results

### *2.4.1 Spectral Reflectance Validation Comparison*

Comparison of field and UAV-based reflectance measurements pooled for all seasons indicated a strong 1:1 correlation ($r^2 \geq 0.94$) with root mean square error (RMSE) less than 0.02 for all visible bands (Figure 2-3). The red edge (RE) and near-infrared (NIR) bands exhibited more variability at higher reflectance values. Overall, reflectance estimated with the UAV imagery and the observed reflectance in the field were well-correlated in the RE and NIR ($r^2 \geq 0.93$), with RMSE's less than 0.05. Linear regression models for each band were found to be statistically significant ($p < 0.005$).

### *2.4.2 Biomass Estimation Models*

The vegetation indices exhibited variable performance in estimating aboveground biomass (Figure 2-4, Table 2-2). Of the vegetation indices, NDVI had the strongest linear correlation to dry aboveground biomass for pooled seasonal data ($r^2 = 0.36$, RMSE = 495.9 g $m^{-2}$, $p < 0.005$; Table 2-2), and for each season when seasonal data was analyzed individually. Live aboveground biomass was also best predicted by NDVI compared to the other VIs (Table S2-2).

**Table 2-2. Aboveground biomass estimation equations for vegetation indices.**

| Index | Biomass Estimation Equation (g $m^{-2}$) | $R^2$ | RMSE (g $m^{-2}$) | p-value |
|---|---|---|---|---|
| CIgreen | 519.1 × CIgreen + 293.6 | 0.263 | 530.6 | <0.005 |
| CIrededge | 952.3 × CIrededge + 730.9 | 0.112 | 582.6 | 0.009 |
| EVI2 | 2867.6 × EVI2 + 566 | 0.244 | 537.5 | <0.005 |
| GNDVI | 3041.2 × GNDVI − 175.3 | 0.302 | 516.6 | <0.005 |
| NRDE | 2686.2 × NDRE + 682.9 | 0.115 | 581.6 | 0.008 |
| NDVI | 2428.2 × NDVI + 120.1 | 0.356 | 495.9 | <0.005 |

Further analysis of the NDVI-based biomass estimation model reveals that season is a significant predictor in estimating aboveground biomass (partial F-test, F = 6.13, p < 0.001). NDVI-aboveground biomass models for the individual seasons exhibited variable success in predicting biomass (

Table 2-3). Although linear models were significant for all seasons, spring had the best performing model ($r^2$ = 0.67, RMSE = 344.3 g $m^{-2}$). For live aboveground biomass, the spring biomass estimation model also outperformed all other seasons (Table S2-3).

**Figure 2-4. Correlation between vegetation indices and dry aboveground biomass for the vegetation indices (a) CIgreen, (b) CIrededge, (c) EVI2, (d) GNDVI, (e) NDRE and (f) NDVI.**

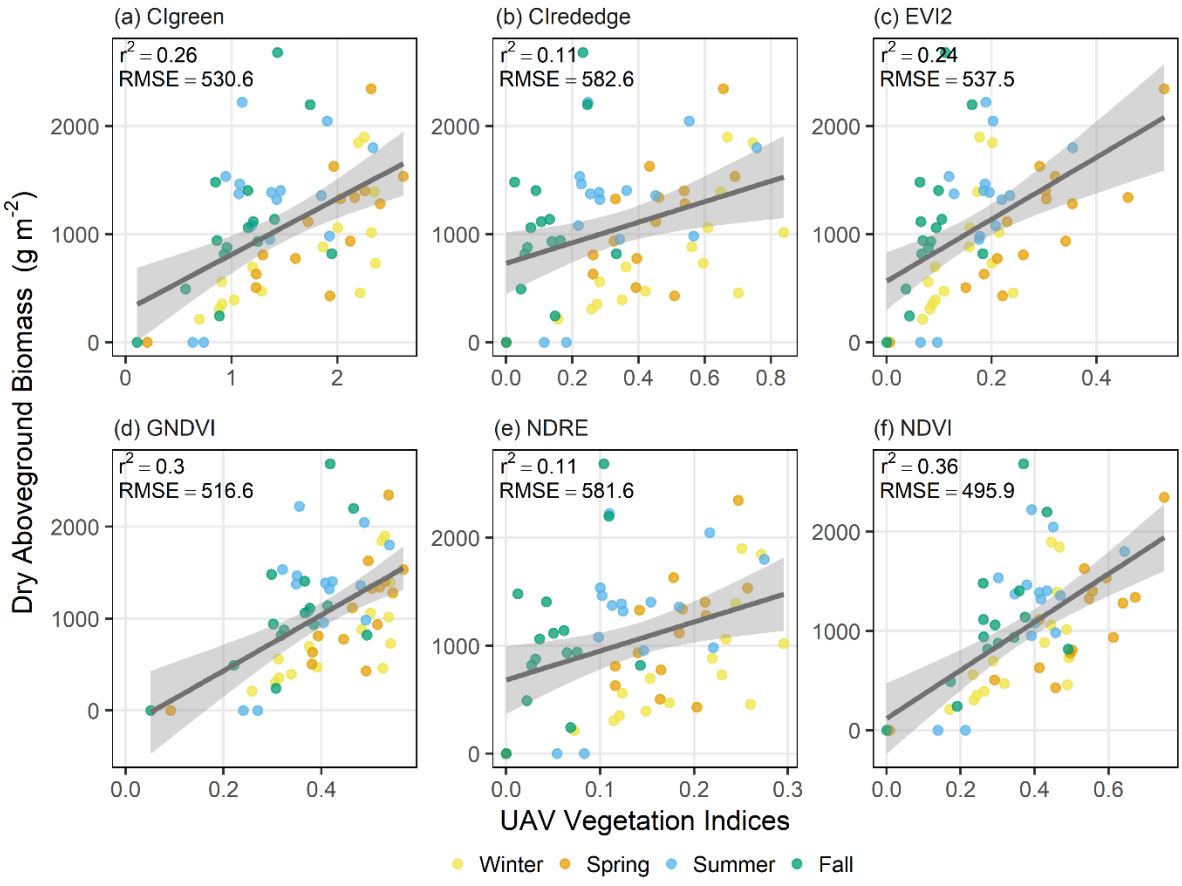


**Table 2-3. Seasonal NDVI-Aboveground biomass estimation equations.**

| Season | NDVI Biomass Estimation Equation (g $m^{-2}$) | $R^2$ | RMSE (g $m^{-2}$) | p-value |
|---|---|---|---|---|
| Winter | 3097.4 × NDVI − 309.4 | 0.448 | 413.6 | 0.006 |

| | | | | |
|---|---|---|---|---|
| Spring | 2670.7 × NDVI − 261.7 | 0.672 | 344.3 | <0.005 |
| Summer | 3725.3 × NDVI − 189.4 | 0.477 | 466.1 | <0.005 |
| Fall | 3717.2 × NDVI − 6.4 | 0.407 | 546 | 0.01 |

### *2.4.3 Spatial and Temporal Patterns in Aboveground Biomass*

The annual NDVI-based biomass estimation model,

$$AGB = 2428.2 \times NDVI + 120.1 \quad (1)$$

was selected to create comparable biomass maps for Basin II of the Carpinteria Salt Marsh Reserve for each season (Figure 2-5). Visual comparison of seasonal biomass maps reveal peak biomass indicative of salt marsh vegetation "green-up" occurring in spring. Analysis of pixel data for each biomass map also indicates an increase in average aboveground biomass in spring, which was estimated to be 1,222.9 ± 435.7 g $m^{-2}$ (Table 2-4). This was 295.3 g $m^{-2}$ higher than the average aboveground biomass estimated for the site in winter, summer, and fall. Similarly, total site biomass in Carpinteria Salt Marsh Basin II was 204.7 Mg in spring, approximately 49.3 Mg higher than total site biomass estimated for winter, summer, and fall.

**Figure 2-5. Biomass maps based on NDVI biomass estimation model for (a) winter, (b) spring, (c) summer and (d) fall.**

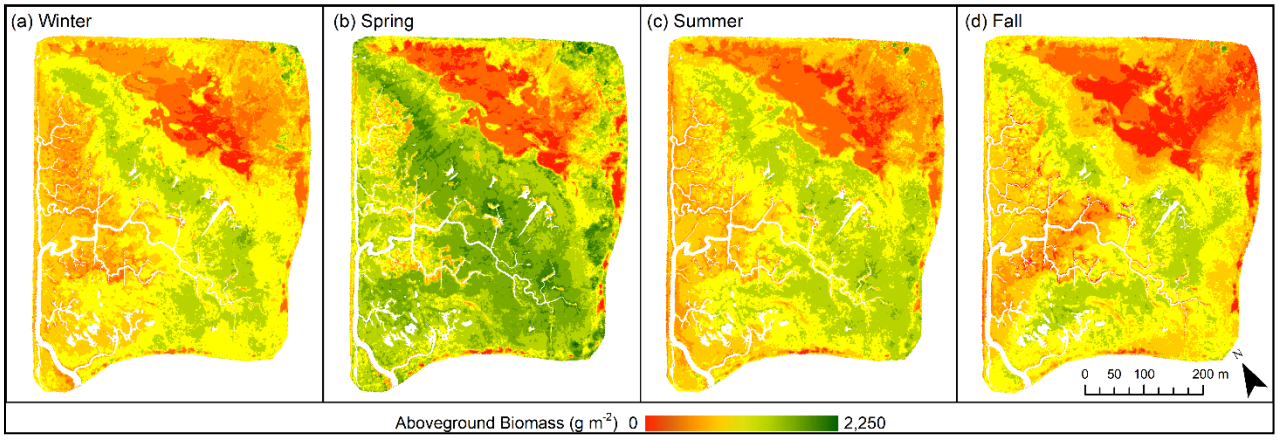


The seasonal patterns suggested by the biomass maps were supported by field observations and analysis of field biomass (Table 2-4). Spring and summer exhibited higher dry and wet aboveground biomass compared to that of fall and winter. Unlike the UAV-derived biomass

estimates, field data suggests peak plot biomass occurred in summer, which may be indicative of ongoing biomass accumulation from spring to summer coinciding with slight declines in vegetation greenness. However, only wet aboveground biomass was found to be significantly different among seasons ($p < 0.001$). Dry aboveground was not significantly different across seasons ($p = 0.27$).

UAV-derived estimates of biomass were compared to elevation for a subset of marsh area along an elevational gradient (Figure 2-6). For all seasons, peak biomass estimates occurred at elevations of 1.6 to 1.8 m. Maximum biomass occurred in spring with averages nearing 1,500 g $m^{-2}$, which was on average approximately 500 g $m^{-2}$ higher than the other seasons.

**Table 2-4. Seasonal biomass estimates from field sampling and UAV biomass maps.**

| | Field Measurements (±S.D.) | | UAV estimates (±S.D.) | | |
|---|---|---|---|---|---|
| | **Wet AGB (g $m^{-2}$)** | **Dry AGB (g $m^{-2}$)** | **Mean Site NDVI** | **Mean Site Dry AGB (g $m^{-2}$)** | **Total Site Dry AGB (Mg)** |
| **Winter** | 1461.0 ± 879.1 | 819.0 ± 536.3 | 0.34 ± 0.12 | 946.3 ± 300.7 | 158.5 |
| **Spring** | 3101.9 ± 2068.1 | 1071.3 ± 579.3 | 0.45 ± 0.18 | 1222.9 ± 435.7 | 204.7 |
| **Summer** | 4131.1 ± 2255.6 | 1262.5 ± 621.3 | 0.35 ± 0.14 | 958.6 ± 338.7 | 160.5 |
| **Fall** | 2972.7 ± 2214.3 | 1080.7 ± 683.3 | 0.31 ± 0.15 | 878.1 ± 359.6 | 147.1 |
| **p-value** | <0.001 | 0.268 | - | - | - |

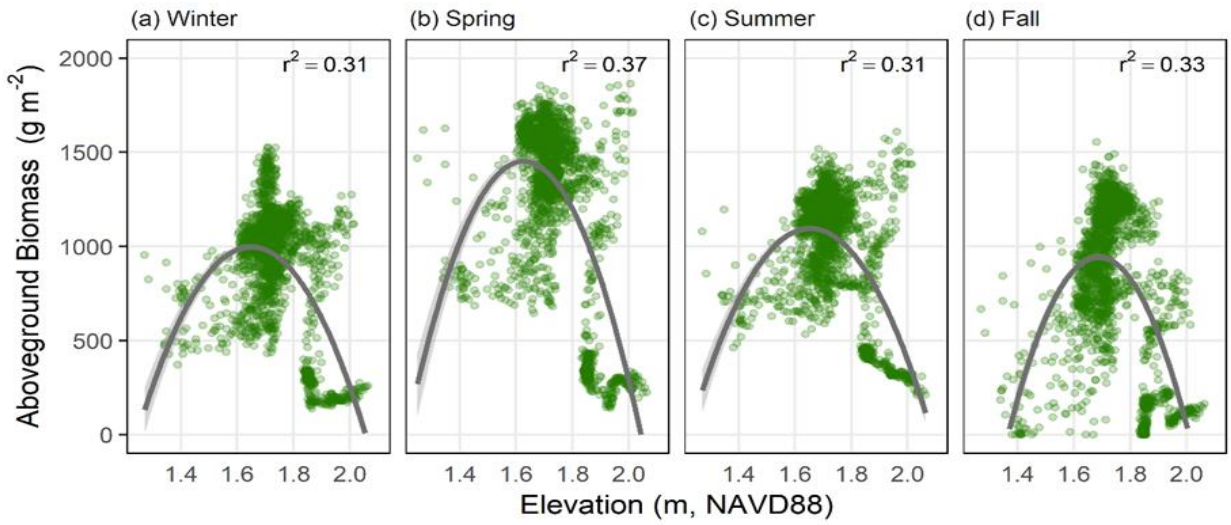

**Figure 2-6. Seasonal comparison of NDVI-based aboveground biomass by elevation for (a) winter, (b) spring, (c) summer and (d) fall. Pixel values (green circles) were extracted along an elevational gradient for vegetated wetland areas. Parabolic relationship shown in gray with standard error shaded light gray.**

## 2.5 Discussion

This study demonstrates potential for mapping aboveground biomass in coastal wetlands using high-resolution multispectral UAV imagery. By combining a UAV approach and field surveys over the course of an annual growing cycle, we were able to develop biomass estimation models based on NDVI, a commonly used proxy for vegetation health and productivity. We found a strong relationship between NDVI and biomass during the spring, which is typically the season of peak greenness. The submeter ground resolution attainable with UAVs was beneficial for investigating fine-scale spatial changes in wetland biomass. UAVs also offer high flexibility in the timing of imagery collection, which would be beneficial for a number of time-sensitive ecological applications. Overall, the multi-temporal, multispectral imagery derived from UAVs can help reveal spatio-temporal variability at resolutions superior to traditional remote sensing approaches.

Our findings reveal the high spatial and temporal variability of aboveground biomass in the Carpinteria Salt Marsh Reserve. The biomass maps created for this site indicate pronounced seasonal variability in vegetation health and biomass (Figure 2-5). This pattern is characteristic of southern California coastal marshes where green-up of vegetation generally occurs in spring following the rainy season with biomass then peaking at the end of summer followed by senescence (Zedler 1982; Zedler 2015). Our biomass maps capture spring green-up but indicate an overall reduction in green vegetation and aboveground biomass in summer (Table 2-4). This seasonal, site-wide response may be explained by spatial variation in vegetation productivity occurring within the marsh due to environmental stress along elevational gradients (Figure 2-6). High soil salinity is a major limiting factor for wetland plant growth in southern California (Zedler 1982), and soil salinity has been shown to vary spatially with elevation and tidal inundation (Traut

2005). While productivity at lower elevations is generally limited by inundation (Guo and Pennings 2012; Janousek and Mayo 2013; Janousek and Folger 2014), higher elevations are prone to increased soil salinities due to reduced tidal flushing, minimal freshwater inputs and high rates of evapotranspiration in hot, dry summer months (Callaway et al. 1990; Callaway and Sabraw 1994). Previous work in the Carpinteria salt marsh indicates reduced tidal exchange within the marsh, with higher elevations receiving as little as 5% of the inundation experienced at lower elevations (Sadro et al. 2007). This case site exemplifies how the high spatial resolutions and flexible temporal sampling frequency provided by UAVs can aid in investigating ecologically meaningful patterns and processes occurring within salt marshes.

However, there is uncertainty associated with the remotely sensed estimates of aboveground biomass that can be attributed to several sources of error caused by the coastal environment, as well as data collection and processing techniques (E. Adam et al. 2010). Environmental factors, such as sky conditions and tidal stage at the time of UAV flight can contribute to radiometric variability. Sky conditions, namely the presence of clouds, have been shown to influence the radiometric correction and resulting homogeneity of the UAV orthophotos (Tagle et al. 2017). We conducted our UAV flights over the course of a year under varying sky conditions. Environmental conditions during field campaigns contribute to radiometric variability, as evidenced by seasonal differences in the correlation among UAV and *in situ* measures of reflectance in the red edge and near-infrared wavelengths (Figure 2-3). This is shown by data collected in the fall, where variability in incoming irradiance associated with partly cloudy conditions led to an underestimation of reflectance by the UAV compared to the canopy reflectance measured *in situ*. Where possible, UAV imagery should be collected under constant sky conditions as close to solar noon as possible (Tagle et al. 2017) in accordance with other logistical, regulatory,

and weather constraints. In addition, the use of a downwelling light sensor, or irradiance sensor, may improve issues arising from variable light conditions; however, in this study, tests including irradiance data during image processing resulted in overestimation of reflectance in UAV imagery and thus, was excluded (Figure S2-1). Finally, sensor noise may also present a significant source of radiometric variability and should be considered when selecting and designing UAV payloads.

The presence of water also poses significant complications to estimating biomass in coastal wetlands using remote sensing approaches. Water inundation dampens the reflectance occurring in the near-infrared wavelengths (Kearney et al. 2009), and so will affect vegetation indices such as NDVI. The depth of inundation, vegetation structure and underlying soils can ultimately interfere with the relationship between reflectance and standing biomass (Byrd et al. 2014). This concern has been demonstrated in long-term time series analyses of wetlands, where high NDVI outliers are more likely to reflect real changes in vegetation, but low outliers are likely to be artifacts of clouds or inundation (Swets et al. 1999). The use of NDVI in this study as the foundation for biomass estimation models, therefore, comes with similar concerns. Due to sampling constraints and our desire to conduct UAV surveys as close to noon as possible, tidal levels varied across our survey dates. As a result, tidal inundation could lead to underestimation of NDVI and affect the relationship between NDVI and biomass. To reduce errors associated with inundation, water was masked for each season using a standardized classification. However, spatial analysis of the final biomass maps reveal potential issues caused by the presence of underlying water in vegetation canopies. In particular, the fall campaign was conducted with tidal levels over two times higher than the other seasons (Table S2-1), which may have resulted in underestimations of biomass, especially in pixels coinciding with lower elevations where tidal inundation is more probable (Figure 2-6). However, one of the benefits of UAV imagery is that the user has control

over the timing of image acquisition. Therefore, field campaigns can be planned so that multi-temporal images are collected at similar tidal stages.

Vegetation phenology likely also impacted our UAV based estimates of biomass. The NDVI-based aboveground biomass model was significantly improved when season was considered as an additional predictor variable, meaning that season plays a significant role in predicting aboveground biomass. Further analysis of biomass estimation models for the individual seasons shows that although biomass estimation models for each season were significant (Table 2-3), spring presents the strongest model for estimating biomass. One key reason for this finding relates to the relationship between greenness and biomass. NDVI is essentially a measure of vegetation greenness, therefore, it serves best as a predictor of live, green biomass, which is typically produced during the growing season beginning in spring (Zedler 1982). This is also evident in NDVI-based biomass estimation models developed for live, or wet, vegetation (Table S2-2, Table S2-3). Following the summer and fall dry season, salt marsh perennial and annual plants have either senesced or died, often resulting in higher levels of non-photosynthetic vegetation (NPV). During summer, fall and winter, poor correlation can be expected between NDVI and biomass due to a lack of green biomass given the environmental stressors and natural phenological cycles at play in these Mediterranean coastal wetland systems. As a result, we recommend that studies examining interannual variability in marsh biomass in this region should conduct multispectral UAV surveys during the spring. These findings also have implications for satellite-based assessments, where peak biomass may be the most informative biomass estimate for detecting long term changes associated with environmental variability (Buffington et al. 2018). This has been shown in other satellite-based assessments. For example, (O'Donnell and Schalles

2016) found a strong correlation ($r^2$ = 0.70) between NDVI and peak biomass in *Spartina* dominated salt marshes on the coast of Georgia.

Further improvements to biomass estimation using UAVs in coastal wetlands can be achieved by more accurately capturing NPV. Fortunately, the ground resolutions provided by UAVs offer a number of advantages for mapping and monitoring coastal wetlands. For instance, the increased spatial resolution of ground pixels leads to a decrease in the amount of mixed pixels, which might contain both green vegetation and NPV. The spectral response of an unmixed pixel will be more representative of a single vegetation cover type, whereas mixed pixels constitute a combination of spectral responses from multiple, often disparate cover types. For example, spectral signatures can vary among herbaceous or woody vegetation types due to the biochemical and biophysical properties of the vegetation (Asner 1998; Klemas 2015b), and therefore, may be more easily differentiated at finer resolutions. Increased spatial resolution has a proven advantage in delineating vegetation classes and estimating percent cover in salt marshes (Marcaccio et al. 2015; Zhou et al. 2017) and mangroves (Ruwaimana et al. 2018) using multispectral imagery. Additionally, increased spectral resolution can also aid in the differentiation of cover types like live vegetation and NPV. Hyperspectral imagery has demonstrated an advantage over broad-band multispectral imagery with improved accuracies in differentiating vegetation types and species (Adam et al. 2010). Gains in both spatial and spectral resolution can increase sensitivity to variations in reflectance or vegetation indices and ultimately improve the separability of different vegetation types.

High-resolution information on vegetation height and structure is another important component that could improve biomass estimation in coastal wetlands. Vegetation height and structure are typically measured remotely using active sensors such as LiDAR and RADAR

(Zolkos et al. 2013). These types of sensors can be placed on UAVs, but they are relatively expensive as compared to multispectral optical sensors. As UAV and sensor technology advances, the inclusion of active sensors to UAV payloads will become more feasible (Whitehead et al. 2014b; Whitehead et al. 2014a). However, passive optical sensors onboard UAVs also have the potential to provide structural information using photogrammetric methods in coastal wetlands (Kalacska et al. 2017). These approaches have been successfully applied in olive orchards, temperate deciduous forests, and mangrove forests (Dandois and Ellis 2013; Díaz-Varela et al. 2015; Otero et al. 2018). However, mapping vegetation height using photogrammetry is challenging in dense coastal wetlands as it is difficult to obtain sufficient numbers of ground points required to calculate vegetation height. For example, errors of up to 80% have been documented in elevation models created for dense cordgrass habitats (Meng et al. 2017b).

## 2.6 Conclusions

Here, we demonstrate that UAVs can aid our understanding of the spatial and temporal patterns in salt marsh biomass and productivity. Improved understanding of how productivity and biomass change over seasonal, annual and decadal time scales is especially valuable, because this could indicate deviations from normal patterns of coastal wetland health. But in order to detect ecologically relevant changes, remote sensing methods must capture both press and pulse disturbances that operate at vastly different temporal scales. In particular, discrete pulse disturbances often require flexibility and rapid deployment to time sampling efforts appropriately in order to capture the impacts to coastal wetlands. Impacts to biomass, productivity and wetland health could serve as harbingers of future climate change impacts and could help establish thresholds of resilience to climate change drivers. Assessment of changes to biomass and

productivity also highlight the potential for high-resolution insights into climate-related threats to ecosystem services, like carbon storage, that are provided by these valuable coastal habitats.

The benefits of UAVs for ecological applications in coastal wetlands are numerous due to their high operational flexibility and relatively low cost. This is a key advantage over traditional aerial and satellite remote sensing. Furthermore, UAVs are a valuable addition to traditional ecological fieldwork, which can often be time and resource intensive and costly, and may limit the scope of study to relatively small areas and periods of time. Therefore, UAVs may be a complementary approach to fill critical spatial and temporal gaps inherent to both field work and other remotely sensed data. Integrating contextual field data, high-accuracy GPS and both UAV and satellite remote sensing approaches can improve our ability to estimate biomass and productivity over time. Overall, remotely sensed data with high spatial and temporal resolutions could provide a more synoptic understanding of coastal wetland ecology and an invaluable view of ecological patterns and processes.

## 2.7 Acknowledgements

Funding for this work was provided by the NASA New Investigator Program (NNX16AN04G). Cheryl Doughty was also supported by a Graduate Research Mentorship and Summer Graduate Research Mentorship at the University of California, Los Angeles. We would like to thank the Carpinteria Salt Marsh Reserve and site director, Andrew Brookes for providing access to the field site. Special thanks to Daniel Jensen, Kate Cavanaugh and Jessica Fayne for their help conducting field work and Amanda Wagner, Nickie Cammisa, Marisol Hernandez-Cira and Jessica Kurylo for laboratory access. Lastly, we thank the editors and the anonymous reviewers whose suggestions have greatly improved the quality of the manuscript.

## 2.8 References


Adam, Elhadi M. I., and Onisimo Mutanga. 2012. Estimation of high density wetland biomass: combining regression model with vegetation index developed from Worldview-2 imagery. *Remote Sensing for Agriculture, Ecosystems, and Hydrology XIV* 8531. Elsevier B.V.: 85310V. https://doi.org/10.1117/12.970469.

Adam, Elhadi, Onisimo Mutanga, and Denis Rugege. 2010. Multispectral and hyperspectral remote sensing for identification and mapping of wetland vegetation: A review. *Wetlands Ecology and Management* 18: 281–296. https://doi.org/10.1007/s11273-009-9169-z.

Asner, Gregory P. 1998. Biophysical and biochemical sources of variability in canopy reflectance. *Remote Sensing of Environment* 64: 234–253. https://doi.org/10.1016/S0034-4257(98)00014-5.

Barnes, Em, TR Clarke, Se Richards, PD Colaizzi, J Haberland, M Kostrzewski, P Waller, et al. 2000. Coincident detection of crop water stress, nitrogen status and canopy density using ground-based multispectral data. In *Proceedings of the Fifth International Conference on Precision Agriculture, Bloomington, MN, USA. Vol. 1619. 2000.*

Berni, Jose a.J., Student Member, Pablo J. Zarco-tejada, Lola Suárez, and Elias Fereres. 2009. Thermal and Narrowband Multispectral Remote Sensing for Vegetation Monitoring From an Unmanned Aerial Vehicle. *IEEE Transactions on Geoscience and Remote Sensing* 47: 722–738. https://doi.org/10.1109/TGRS.2008.2010457.

Buffington, Kevin J., Bruce D. Dugger, and Karen M. Thorne. 2018. Climate-related variation in plant peak biomass and growth phenology across Pacific Northwest tidal marshes. *Estuarine, Coastal and Shelf Science* 202: 212–221. https://doi.org/10.1016/j.ecss.2018.01.006.

Byrd, Kristin B., Jessica L. O'Connell, Stefania Di Tommaso, and Maggi Kelly. 2014. Evaluation of sensor types and environmental controls on mapping biomass of coastal marsh emergent vegetation. *Remote Sensing of Environment* 149. Elsevier B.V.: 166–180. https://doi.org/10.1016/j.rse.2014.04.003.

Callaway, Ragan M., Scott Jones, Wayne R. Ferren Jr., and Anuja Parikh. 1990. Ecology of a mediterranean-climate estuarine wetland at Carpinteria, California: plant distributions and soil salinity in the upper marsh. *Canadian Journal of Botany* 68: 1139–1146. https://doi.org/10.1139/b90-144.

Callaway, Ragan M., and Craig S. Sabraw. 1994. Effects of variable precipitation on the structure and diversity of a California salt marsh community. *Journal of Vegetation Science* 5: 433–438. https://doi.org/10.2307/3235867.

Chen, Shuisen, Liusheng Han, Xiuzhi Chen, Dan Li, Lin Sun, and Yong Li. 2015. Estimating wide range Total Suspended Solids concentrations from MODIS 250-m imageries: An improved method. *ISPRS Journal of Photogrammetry and Remote Sensing* 99. International Society for Photogrammetry and Remote Sensing, Inc. (ISPRS): 58–69. https://doi.org/10.1016/j.isprsjprs.2014.10.006.

Chong, Albert K. 2007. HD aerial video for coastal zone ecological mapping. *Presented at SIRC 2007 – The 19th Annual Colloquium of the Spatial Information Research Centre*

*University of Otago, Dunedin, New Zealand December 6th-7th 2007*.

Dandois, Jonathan P., and Erle C. Ellis. 2013. High spatial resolution three-dimensional mapping of vegetation spectral dynamics using computer vision. *Remote Sensing of Environment* 136. The Authors: 259–276. https://doi.org/10.1016/j.rse.2013.04.005.

Day, John W., Robert R. Christian, Donald M. Boesch, Alejandro Yáñez-Arancibia, James Morris, Robert R. Twilley, Larissa Naylor, Linda Schaffner, and Court Stevenson. 2008. Consequences of climate change on the ecogeomorphology of coastal wetlands. *Estuaries and Coasts* 31: 477–491. https://doi.org/10.1007/s12237-008-9047-6.

Delacourt, Christophe, Pascal Allemand, Marion Jaud, Philippe Grandjean, Anne Deschamps, Jérôme Ammann, and V Cuq. 2009. DRELIO : An Unmanned Helicopter for Imaging Coastal Areas. *Journal of Coastal Research, Special Issue 56, Proceedings of the 10th International Coastal Symposium* 56: 1489–1493.

Díaz-Varela, Ramón A., Raúl de la Rosa, Lorenzo León, and Pablo J. Zarco-Tejada. 2015. High-resolution airborne UAV imagery to assess olive tree crown parameters using 3D photo reconstruction: Application in breeding trials. *Remote Sensing* 7: 4213–4232. https://doi.org/10.3390/rs70404213.

Doughty, C.L. 2019. Batch processing Micasense images to reflectance (batch-imageprocessing), GitHub repository.

Gallant, Alisa L. 2015. The challenges of remote monitoring of wetlands. *Remote Sensing* 7: 10938–10950. https://doi.org/10.3390/rs70810938.

Gitelson, Anatoly A., Yoram J. Kaufman, and Mark N. Merzlyak. 1996. Use of a green channel in remote sensing of global vegetation from EOS-MODIS. *Remote Sensing of Environment* 58. Elsevier: 289–298. https://doi.org/10.1016/S0034-4257(96)00072-7.

Gitelson, Anatoly A., Mark N. Merzlyak, and Hartmut K. Lichtenthaler. 1996. Detection of Red Edge Position and Chlorophyll Content by Reflectance Measurements Near 700 nm. *Journal of Plant Physiology* 148. Urban & Fischer: 501–508. https://doi.org/10.1016/S0176-1617(96)80285-9.

Gitelson, Anatoly A., Andrés Viña, Verónica Ciganda, Donald C. Rundquist, and Timothy J. Arkebauer. 2005. Remote estimation of canopy chlorophyll content in crops. *Geophysical Research Letters* 32. John Wiley & Sons, Ltd: L08403. https://doi.org/10.1029/2005GL022688.

Goodman, Arianna C., Karen M. Thorne, Kevin J. Buffington, Chase M. Freeman, and Christopher N. Janousek. 2018. El Niño Increases High-Tide Flooding in Tidal Wetlands Along the U.S. Pacific Coast. *Journal of Geophysical Research: Biogeosciences* 123: 3162–3177. https://doi.org/10.1029/2018JG004677.

Guo, Hongyu, and Steven C. Pennings. 2012. Mechanisms mediating plant distributions across estuarine landscapes in a low-latitude tidal estuary. *Ecology* 93: 90–100. https://doi.org/10.1890/11-0487.1.

Hugenholtz, Chris. 2012. Small unmanned aircraft systems for remote sensing and earth science research. *Eos* 93: 24–25. https://doi.org/10.1117/1.3474649.

Hugenholtz, Chris H., Ken Whitehead, Owen W. Brown, Thomas E. Barchyn, Brian J.

Moorman, Adam LeClair, Kevin Riddell, and Tayler Hamilton. 2013. Geomorphological mapping with a small unmanned aircraft system (sUAS): Feature detection and accuracy assessment of a photogrammetrically-derived digital terrain model. *Geomorphology* 194. Elsevier B.V.: 16–24. https://doi.org/10.1016/j.geomorph.2013.03.023.

Janousek, Christopher N., Kevin J. Buffington, Karen M. Thorne, Glenn R. Guntenspergen, John Y. Takekawa, and Bruce D. Dugger. 2016. Potential effects of sea-level rise on plant productivity: Species-specific responses in northeast Pacific tidal marshes. *Marine Ecology Progress Series* 548: 111–125. https://doi.org/10.3354/meps11683.

Janousek, Christopher N., and Christina L. Folger. 2014. Variation in tidal wetland plant diversity and composition within and among coastal estuaries: Assessing the relative importance of environmental gradients. *Journal of Vegetation Science* 25: 534–545. https://doi.org/10.1111/jvs.12107.

Janousek, Christopher N., and Cara Mayo. 2013. Plant responses to increased inundation and salt exposure: Interactive effects on tidal marsh productivity. *Plant Ecology* 214. Springer Netherlands: 917–928. https://doi.org/10.1007/s11258-013-0218-6.

Jensen, Austin M., Thomas Hardy, Mac McKee, and YangQuan Chen. 2011. Using a multispectral autonomous unmanned aerial remote sensing platform (AggieAir) for riparian and wetlands applications. *International Geoscience and Remote Sensing Symposium (IGARSS)*: 3413–3416. https://doi.org/10.1109/IGARSS.2011.6049953.

Jiang, Zhangyan, Alfredo R. Huete, Kamel Didan, and Tomoaki Miura. 2008. Development of a two-band enhanced vegetation index without a blue band. *Remote Sensing of Environment* 112. Elsevier: 3833–3845. https://doi.org/10.1016/J.RSE.2008.06.006.

Kalacska, M., G. L. Chmura, O. Lucanus, D. Bérubé, and J. P. Arroyo-Mora. 2017. Structure from motion will revolutionize analyses of tidal wetland landscapes. *Remote Sensing of Environment* 199: 14–24. https://doi.org/10.1016/j.rse.2017.06.023.

Kearney, Michael S., David Stutzer, Kevin Turpie, and J. Court Stevenson. 2009. The Effects of Tidal Inundation on the Reflectance Characteristics of Coastal Marsh Vegetation. *Journal of Coastal Research* 256: 1177–1186. https://doi.org/10.2112/08-1080.1.

Kirwan, Matthew L., and Glenn R. Guntenspergen. 2015. Response of plant productivity to experimental flooding in a stable and a submerging marsh. *Ecosystems* 18. Springer US: 903–913. https://doi.org/10.1007/s10021-015-9870-0.

Kirwan, Matthew L., and J. Patrick Megonigal. 2013. Tidal wetland stability in the face of human impacts and sea-level rise. *Nature* 504: 53–60. https://doi.org/10.1038/nature12856.

Klemas, Victor. 2013. Remote sensing of coastal wetland biomass: An overview. *Journal of Coastal Research* 290: 1016–1028. https://doi.org/10.2112/JCOASTRES-D-12-00237.1.

Klemas, Victor V. 2015a. Coastal and Environmental Remote Sensing from Unmanned Aerial Vehicles: An Overview. *Journal of Coastal Research* 315: 1260–1267. https://doi.org/10.2112/JCOASTRES-D-15-00005.1.

Klemas, Victor V. 2015b. Remote Sensing of Mangroves. In *Remote Sensing of Wetlands: Applications and Advances*, 241–262. CRC Press. https://doi.org/doi:10.1201/b18210-

16\r10.1201/b18210-16.

Klemas, Victor V. 2009. Remote Sensing of Coastal Ecosystems and Environments. *Remote Sensing and Modeling* 8: 978-1-4244-2268–5. https://doi.org/10.1007/978-3-319-06326-3.

Manfreda, Salvatore, Matthew F. McCabe, Pauline E. Miller, Richard Lucas, Victor Pajuelo Madrigal, Giorgos Mallinis, Eyal Ben Dor, et al. 2018. On the use of unmanned aerial systems for environmental monitoring. *Remote Sensing* 10. https://doi.org/10.3390/rs10040641.

Marcaccio, James V., Chantel E. Markle, and Patricia Chow-Fraser. 2015. Unmanned aerial vehicles produce high-resolution, seasonally-relevant imagery for classifying wetland vegetation. *International Archives of the Photogrammetry, Remote Sensing and Spatial Information Sciences - ISPRS Archives* 40: 249–256. https://doi.org/10.5194/isprsarchives-XL-1-W4-249-2015.

Meng, Xuelian, Nan Shang, Xukai Zhang, Chunyan Li, Kaiguang Zhao, Xiaomin Qiu, and Eddie Weeks. 2017a. Photogrammetric UAV mapping of terrain under dense coastal vegetation: An object-oriented classification ensemble algorithm for classification and terrain correction. *Remote Sensing* 9: 1–23. https://doi.org/10.3390/rs9111187.

Meng, Xuelian, Nan Shang, Xukai Zhang, Chunyan Li, Kaiguang Zhao, Xiaomin Qiu, and Eddie Weeks. 2017b. Photogrammetric UAV mapping of terrain under dense coastal vegetation: An object-oriented classification ensemble algorithm for classification and terrain correction. *Remote Sensing* 9: 1–23. https://doi.org/10.3390/rs9111187.

Mishra, Deepak R., and Shuvankar Ghosh. 2015. Using Moderate-Resolution Satellite Sensors for Monitoring the Biophysical Parameters and Phenology of Tidal Marshes. In *Remote Sensing of Wetlands: Applications and Advances*, 300–331. CRC Press.

Morris, James T., P. V. Sundareshwar, Christopher T. Nietch, Björn Bjorn Kjerfve, and D. R. Cahoon. 2002. Responses of coastal wetlands to rising sea level. *Ecology* 83: 2869–2877. https://doi.org/10.2307/3072022.

Mutanga, O., and A. K. Skidmore. 2004. Narrow band vegetation indices overcome the saturation problem in biomass estimation. *International Journal of Remote Sensing* 25: 3999–4014. https://doi.org/10.1080/01431160310001654923.

O'Donnell, John P R, and John F Schalles. 2016. Examination of abiotic drivers and their influence on Spartina alterniflora biomass over a twenty-eight year period using Landsat 5 TM satellite imagery of the Central Georgia Coast. *Remote Sensing* 8: 477-. https://doi.org/10.3390/rs8060477.

Osland, Michael J., Nicholas M. Enwright, Richard H. Day, Christopher A. Gabler, C.L. Stagg, and J.B. Grace. 2016. Beyond just sea-level rise: considering macroclimatic drivers within coastal wetland vulnerability assessments to climate change. *Global Change Biology* 22: 1–11. https://doi.org/10.1111/gcb.13084.

Otero, Viviana, Ruben Van De Kerchove, Behara Satyanarayana, Columba Martínez-Espinosa, Muhammad Amir Bin Fisol, Mohd Rodila Bin Ibrahim, Ibrahim Sulong, Husain Mohd-Lokman, Richard Lucas, and Farid Dahdouh-Guebas. 2018. Managing mangrove forests from the sky: Forest inventory using field data and Unmanned Aerial Vehicle (UAV)

imagery in the Matang Mangrove Forest Reserve, peninsular Malaysia. *Forest Ecology and Management* 411. Elsevier: 35–45. https://doi.org/10.1016/j.foreco.2017.12.049.

Ozesmi, Stacy L., and Marvin E. Bauer. 2002. Satellite remote sensing of wetlands. *Wetlands Ecology and Management* 10: 381–402. https://doi.org/10.1023/A:1020908432489.

Pennings, Steven C., Mary Bestor Grant, and Mark D. Bertness. 2005. Plant zonation in low-latitude salt marshes: Disentangling the roles of flooding, salinity and competition. *Journal of Ecology* 93: 159–167. https://doi.org/10.1111/j.1365-2745.2004.00959.x.

Pereira, E, R Bencatel, J Correia, L. Felix, G Goncalves, J Morgado, and J Sousa. 2009. Unmanned air vehicles for coastal and environmental research. *Journal of Coastal Research* 56: 1557–1561. https://doi.org/http://www.jstor.org/stable/25738051.

Rouse, JW, RH Haas, JA Schell, and DW Deering. 1974. Monitoring vegetation systems in the Great Plains with ERTS. *NASA Spec. Publ.*: 351, 309.

Ruwaimana, Monika, Behara Satyanarayana, Viviana Otero, Aidy M. Muslim, A. Muhammad Syafiq, Sulong Ibrahim, Dries Raymaekers, Nico Koedam, and Farid Dahdouh-Guebas. 2018. The advantages of using drones over space-borne imagery in the mapping of mangrove forests. *PLoS ONE* 13: 1–22. https://doi.org/10.1371/journal.pone.0200288.

Sadro, Steven, Mary Gastil-Buhl, and John Melack. 2007. Characterizing patterns of plant distribution in a southern California salt marsh using remotely sensed topographic and hyperspectral data and local tidal fluctuations. *Remote Sensing of Environment* 110: 226–239. https://doi.org/10.1016/j.rse.2007.02.024.

Samiappan, Sathishkumar, Gray Turnage, Lee Allen Hathcock, and Robert Moorhead. 2016. Mapping of invasive phragmites (common reed) in Gulf of Mexico coastal wetlands using multispectral imagery and small unmanned aerial systems. *International Journal of Remote Sensing* 38. Taylor & Francis: 1–22. https://doi.org/10.1080/01431161.2016.1271480.

Scavia, Donald, John C Field, Donald F Boesch, Robert W Buddemeier, Daniel R Cayan, Michael Fogarty, Mark A Harwell, et al. 2002. Climate Change Impacts on U. S. Coastal and Marine Ecosystems. *Estuaries* 25: 149–164.

Schmidt, K. S., and A. K. Skidmore. 2003. Spectral discrimination of vegetation types in a coastal wetland. *Remote Sensing of Environment* 85: 92–108. https://doi.org/10.1016/S0034-4257(02)00196-7.

Shanmugam, Palanisamy. 2013. Remote Sensing of the Coastal Ecosystems. *Journal of Geophysics and Remote Sensing* S2: e001. https://doi.org/10.4172/2169-0049.S2-e001.

Sugiura, Ryo, Noboru Noguchi, and Kazunobu Ishii. 2005. Remote-sensing Technology for Vegetation Monitoring using an Unmanned Helicopter. *Biosystems Engineering* 90: 369–379. https://doi.org/10.1016/j.biosystemseng.2004.12.011.

Swets, Daniel L., S. E. Marko, J. Rowland, and B. C. Reed. 1999. Statistical Methods for NDVI Smoothing. In *Proceedings, American Society for Photogramity and Remote Sensing*.

Tagle, Ximena, Maria Ximena Tagle Casapia, Ximena Tagle, and Ximena. 2017. Study of radiometric variations in Unmanned Aerial Vehicle remote sensing imagery for vegetation mapping. Lund University. https://doi.org/10.13140/RG.2.2.16940.36485.

Traut, Bibit Halliday. 2005. The role of coastal ecotones: A case study of the salt marsh/upland transition zone in California. *Journal of Ecology* 93: 279–290. https://doi.org/10.1111/j.1365-2745.2005.00969.x.

Turner, Ian L., Mitchell D. Harley, and Christopher D. Drummond. 2016. UAVs for coastal surveying. *Coastal Engineering* 114. Elsevier B.V.: 19–24. https://doi.org/10.1016/j.coastaleng.2016.03.011.

Vincent, John B., Leland K. Weden, and Mark A. Ditmer. 2014. Barriers to adding UAVs to the ecologist's toolbox. *Frontiers in Ecology and the Environment* 13: 73–74. https://doi.org/10.1890/15.WB.001.

Whitehead, Ken, Chris H. Hugenholtz, Stephen Myshak, Owen Brown, Adam LeClair, Aaron Tamminga, Thomas E. Barchyn, Brian Moorman, and Brett Eaton. 2014a. Remote sensing of the environment with small unmanned aircraft systems (UASs), part 1: a review of progress and challenges. *Journal of Unmanned Vehicle Systems* 02: 86–102. https://doi.org/10.1139/juvs-2014-0007.

Whitehead, Ken, Chris H. Hugenholtz, Stephen Myshak, Owen Brown, Adam LeClair, Aaron Tamminga, Thomas E. Barchyn, Brian Moorman, and Brett Eaton. 2014b. Remote sensing of the environment with small unmanned aircraft systems (UASs), part 2: scientific and commercial applications. *Journal of Unmanned Vehicle Systems* 02: 86–102. https://doi.org/10.1139/juvs-2014-0007.

Xue, Jinru, and Baofeng Su. 2017. Significant remote sensing vegetation indices: a review of developments and applications. *Journal of sensors* Vol.2017: 17p. https://doi.org/10.1155/2017/1353691.

Zedler, Joy B. 1982. The ecology of southern California coastal salt marshes: a community profile. *U.S. Fish and Wildlife Service, Biological Servces Program, Washington, D.C. FWS/OBS-81/54*: 110 p.

Zedler, Joy B. 2015. Salt Marsh Secrets. In , 1–11.

Zhang, M., Susan L. Ustin, E Rejmankova, and Eric W Sanderson. 1997. Monitoring Pacific Coast Salt Marshes Using Remote Sensing. *Ecological Applications* 7: 1039–1053. https://doi.org/https://doi.org/10.1890/1051-0761(1997)007[1039:MPCSMU]2.0.CO;2.

Zhou, Zaiming, Yanming Yang, and Benqing Chen. 2017. Estimating Spartina alterniflora fractional vegetation cover and aboveground biomass in a coastal wetland using SPOT6 satellite and UAV data. *Aquatic Botany*. Elsevier B.V. https://doi.org/10.1016/j.aquabot.2017.10.004.

Zhou, Zaiming, Yanming Yang, and Benqing Chen. 2018. Estimating Spartina alterniflora fractional vegetation cover and aboveground biomass in a coastal wetland using SPOT6 satellite and UAV data. *Aquatic Botany* 144. Elsevier: 38–45. https://doi.org/10.1016/j.aquabot.2017.10.004.

Zolkos, S. G., S. J. Goetz, and R. Dubayah. 2013. A meta-analysis of terrestrial aboveground biomass estimation using lidar remote sensing. *Remote Sensing of Environment* 128. Elsevier Inc.: 289–298. https://doi.org/10.1016/j.rse.2012.10.017.

Zomer, R. J., A. Trabucco, and S. L. Ustin. 2009. Building spectral libraries for wetlands land

cover classification and hyperspectral remote sensing. *Journal of Environmental Management* 90. Elsevier Ltd: 2170–2177. https://doi.org/10.1016/j.jenvman.2007.06.028.

## 2.9 Supplemental Materials

**Table S2-1. Site conditions and flight data for seasonal field surveys.**

| Season | Date | Initial Flight Time (hh:mm PST) | Sky Conditions | Tidal level (m NAVD88) | Flight Duration (h:mm) | Flight Altitude (m) | Coverage Area ($km^2$) | Ground Resolution (cm $pixel^{-1}$) | Orthophoto Horizontal Error (cm)* |
|---|---|---|---|---|---|---|---|---|---|
| Winter | 02/23/2018 | 11:45 | Clear | 0.28 | 0:32 | 92.5 | 0.24 | 6.23 | 11.9 |
| Spring | 05/24/2018 | 11:43 | Overcast | 0.24 | 0:28 | 91.8 | 0.35 | 6.11 | 4.3 |
| Summer | 07/19/2018 | 11:55 | Clear | 0.58 | 0:31 | 92.0 | 0.33 | 6.12 | 7.3 |
| Fall | 11/13/2018 | 12:13 | Partly cloudy | 1.29 | 0:37 | 92.0 | 0.35 | 6.11 | 11.1 |

Average tidal levels are reported for the nearest open-ocean NOAA tidal station, Santa Barbara, CA (9411340).

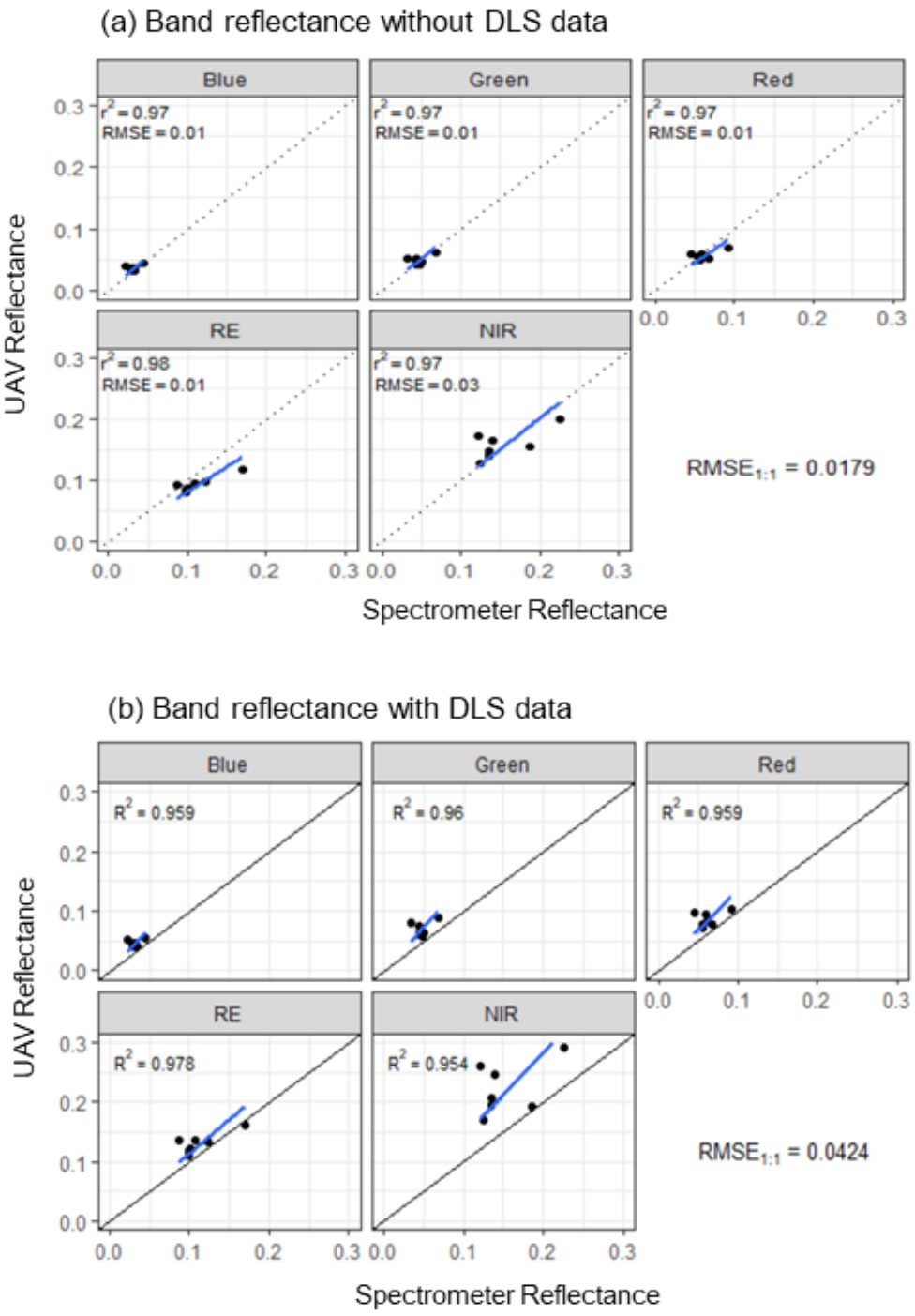


**Figure S2-1. Radiomatric performance of UAV orthomosaic (a) without and (b) with the inclusion of downwelling light sensor (DLS) data in image processing. Reflectance derived from UAV orthomosaics were compared to spectrometer reflectance of the vegetation canopy measured *in situ*.**

**Table S2-2. Live aboveground biomass estimation equations for vegetation indices.**

| Index | Biomass Estimation Equation ($g\ m^{-2}$) | $R^2$ | RMSE ($g\ m^{-2}$) | p-value |
|---|---|---|---|---|
| CIgreen | 1423.6*CIgreen + 819.3 | 0.166 | 1952.7 | < 0.005 |
| CIrededge | 1993.2*CIrededge + 2231.2 | 0.041 | 2093.4 | 0.12 |
| EVI2 | 11060.4*EVI2 + 1017.7 | 0.303 | 1784.2 | < 0.005 |
| GNDVI | 8437.8*GNDVI - 506.1 | 0.194 | 1918.9 | < 0.005 |
| NRDE | 5933.4*NDRE + 2087.3 | 0.047 | 2087 | 0.1 |
| NDVI | 8433.9*NDVI - 342.3 | 0.36 | 1710.8 | < 0.005 |

**Table S2-3. Seasonal NDVI-Live aboveground biomass estimation equations.**

| Season | NDVI Live Biomass Estimation Equation ($g\ m^{-2}$) | $R^2$ | RMSE ($g\ m^{-2}$) | p-value |
|---|---|---|---|---|
| Winter | 6002.5*NDVI - 725.7 | 0.626 | 557.8 | < 0.005 |
| Spring | 9790.3*NDVI - 1784.7 | 0.709 | 1158.4 | < 0.005 |
| Summer | 13743.8*NDVI - 1225.4 | 0.493 | 1666.6 | < 0.005 |
| Fall | 12997.2*NDVI - 828.6 | 0.474 | 1666.6 | < 0.005 |

## CHAPTER 3: Characterizing spatial variability in coastal wetland biomass across multiple scales using UAV and satellite imagery[3]

### 3.1 Abstract

Coastal wetland biomass is an important indicator of wetland productivity, carbon storage, health, and vulnerability to climate change. The ability to estimate aboveground biomass (AGB) in wetlands at ecologically relevant scales is complicated by the spatial variability inherent to patterns in wetland vegetation and the biogeomorphic processes that help create them. Remote sensing provides an approach for mapping wetland biomass, but the spatial resolutions of satellite and airborne imagery often constrain the types of ecological patterns and processes that can be detected. Unmanned Aerial Vehicles (UAVs) have previously been used to capture fine-scale (≤ 1m) variability in AGB in coastal wetland settings. However, it is unclear if a UAV approach to estimating wetland biomass is transferrable across diverse wetland sites or how it compares to commonly used satellite-based approaches. Here, we test the capabilities of UAVs in remotely quantifying AGB and compare biomass estimation using UAV and Landsat satellite imagery (30 m resolution) in several wetland sites in southern California. Field surveys highlight significant spatial variability in wetland plant community AGB and height that influence remote biomass estimation. Relationships between UAV vegetation indices and AGB were site-specific and influenced by vegetation types. Biomass estimation using UAVs ($r^2$ = 0.40, RMSE = 534.6 g $m^{-2}$) showed better correlation with NDVI than a Landsat-based approach ($r^2$ = 0.26, RMSE = 596.8 g $m^{-2}$). We found combining high-resolution UAV AGB maps and Landsat NDVI to develop AGB models showed the highest correlation ($r^2$ = 0.45, RMSE = 659.7 g $m^{-2}$) and provided additional

[3] This chapter has been submitted to Remote Sensing in Ecology and Conservation and is under review as Doughty CL, Ambrose RF, Okin GS, Cavanaugh KC. Characterizing spatial variability in coastal wetland biomass across multiple scales using UAV and satellite imagery. Remote Sens Ecol Conserv.

spatial information to aid scaling field data to satellite imagery. Overall, UAVs captured more spatial complexity in aboveground biomass at finer scales than is possible with moderate-resolution Landsat pixels, indicating that UAVs can be used to characterize patterns of within-marsh variability resulting from local-scale (≤ 100s of meters) ecological processes.

### 3.2 Introduction

Coastal wetland biomass is an important indicator of ecosystem productivity, carbon storage capacity, and resiliency to climate change. This is because biomass is the product of complex biogeomorphic processes in wetlands that link plant growth and turnover, biomass accumulation, and decomposition in response to abiotic factors like elevation, inundation, freshwater inflow, and salinity (Cahoon et al. 2009; Cahoon and Guntenspergen 2010). Through biogeomorphic processes wetland vegetation contributes to vertical accretion through biomass creation, organic matter burial, and sediment trapping, which allows marshes to engineer their surrounding habitat to optimize plant productivity (Morris et al. 2002) and improve resilience to sea level rise (Kirwan and Guntenspergen 2015; Pennings et al. 2005). Inferring the state of these processes using measures of biomass, however, often requires harvesting vegetation through intensive fieldwork. As a result, data on coastal wetland biomass can be difficult to collect frequently enough and at spatial scales that capture the full range of variability of the processes and patterns relevant to coastal wetland ecology.

Coastal wetlands exhibit high spatial and temporal complexity in vegetation as a result of dynamic physical, abiotic drivers, and biotic responses that mediate biogeomorphic processes. Physical and biological factors that control wetland biomass form a hierarchy that operates across multiple spatial and temporal scales (Figure 3-1). Relevant processes and patterns vary among

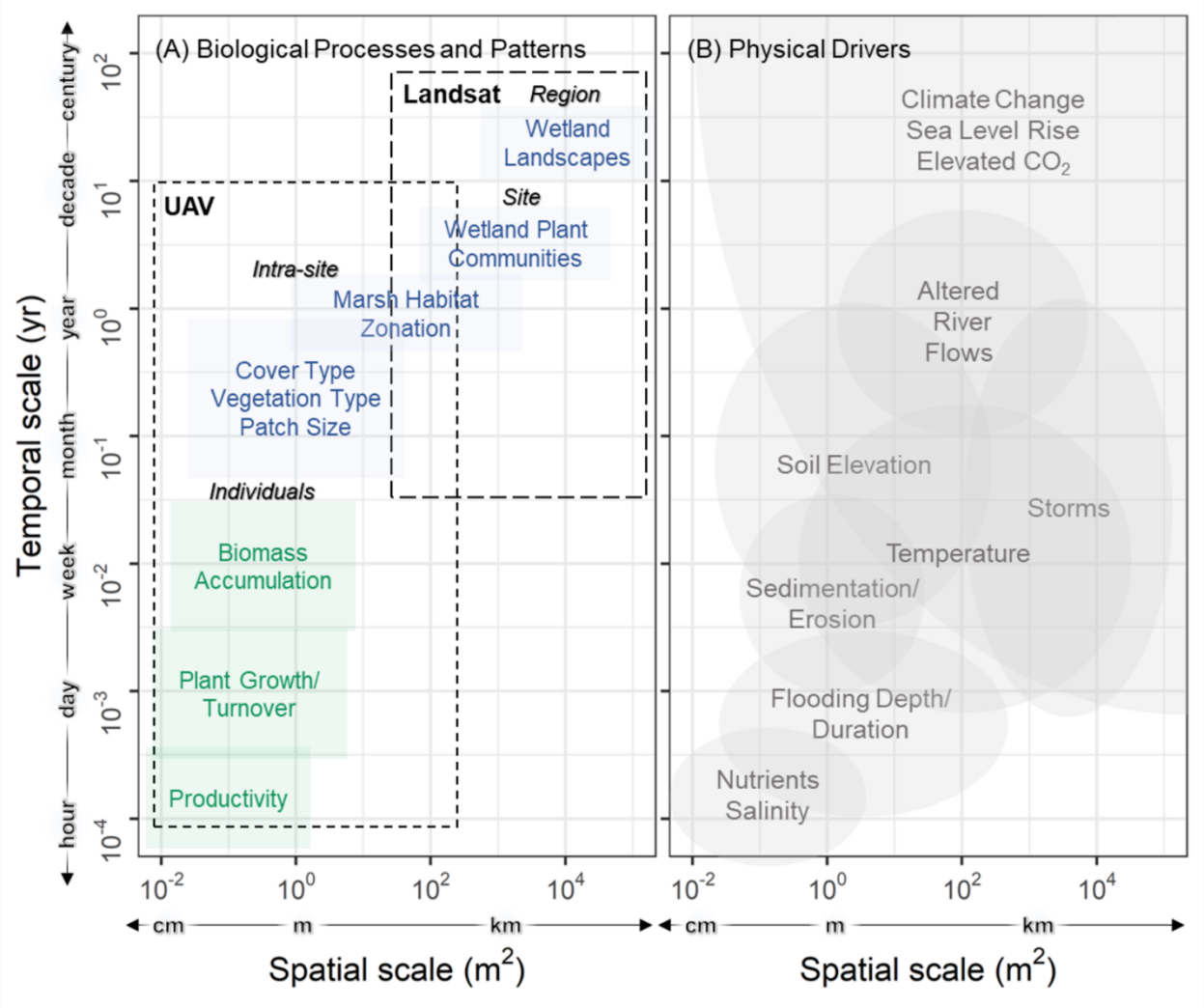


**Figure 3-1. Conceptual hierarchy of factors related to wetland biomass in space and time. (A) Biological processes (green) occurring at fine scales give rise to patterns (blue) in wetland vegetation. The organizational levels at which processes and patterns manifest are labeled in italics. (B) Physical abiotic drivers (grey) influence biological processes and patterns across scales. Scale determines which factors can be remotely assessed using UAVs and Landsat (dashed lines).**

organizational levels that range from individual plants, within sites, among sites, and regions. Abiotic drivers influence biological plant processes occurring at fine scales that give rise to patterns in wetland vegetation at larger scales. For example, sea level rise is an abiotic driver operating across large spans of space (100s of km) and time (years to centuries) that can alter daily tidal inundation levels in a wetland, but its impacts can vary across fine-scales (≤ 1m) within wetlands according to existing topography or creek distributions. Changing inundation levels can

influence plant productivity, and over time can lead to measurable changes in vegetation species composition and standing biomass. Because of these complex interactions across space and time, vegetation patterns in coastal wetlands can be highly spatially complex, as evidenced by heterogeneous plant community composition, marsh zonation, and species' elevational niches. Impacts of physical drivers on phenology and biomass production can be highly variable among wetland sites, zones, and species (Goodman et al. 2018; Janousek et al. 2016). Such high spatial complexity contributes to variability in vegetation properties like height and density, productivity, and biomass that can be difficult to capture.

Investigations into coastal wetland productivity, aboveground biomass, and carbon dynamics at broad scales are possible using remote sensing (Klemas 2013a). Remote sensing based approaches can help reveal large-scale spatial and temporal patterns in bioproductivity through the remote quantification of biomass (Byrd et al. 2014). Biomass estimation in optical remote sensing uses vegetation indices to summarize the spectral reflectance occurring within visible and near-infrared wavelengths that are sensitive to plant biomass (Mutanga and Skidmore 2004; Xue and Su 2017). The correlation between vegetation indices, such as the normalized difference vegetation index (NDVI), and *in situ* biomass measurements provide a basis for biomass estimation using satellite imagery (Klemas 2013a; Mutanga et al. 2012; Pettorelli et al. 2005; Zhang et al. 1997). This approach has been used to estimate biomass in tidal wetland settings using the Landsat satellite archive of moderate-resolution (30 m) optical imagery (Buffington et al. 2018; Byrd et al. 2018, 2014; Gross et al. 1987; Mo et al. 2015; O'Donnell and Schalles 2016). Landsat is commonly used for its global coverage, 16-day revisit frequency, and decades-long data archive, which provides an invaluable tool for investigating long-term changes at broad scales (Kennedy et al. 2014; Pasquarella et al. 2016; Wulder et al. 2012). However, there are a number of limitations to

estimating coastal wetland biomass from satellite multispectral imagery (Gallant 2015), such as the interference of water in the atmosphere and in underlying soils (Kearney et al. 2009; Mutanga and Skidmore 2004).

Issues of scale present additional challenges to estimating aboveground biomass in coastal wetlands using remote sensing. Tradeoffs in the spatial, temporal, and spectral resolution of satellite imagery can obscure ecologically relevant patterns and processes occurring at fine spatial scales (Kennedy et al. 2014), such as habitat function, complexity, and community composition that contribute to biomass variability in wetlands. Moderate-resolution (30-m) Landsat has had difficulty characterizing the high spatial heterogeneity of wetland gradients (Adam et al. 2010; Ozesmi and Bauer 2002; Pasquarella et al. 2016). Furthermore, the development of biomass estimation models often relies on *in situ* biomass measurements taken at scales much finer than the spatial resolution of satellite imagery (Baccini et al. 2007; Wu and Li 2009). How successfully field measurements capture variability in coastal wetland plant communities can influence predictive models and resulting biomass estimates (Baccini et al. 2007; Byrd et al. 2014). These challenges make it difficult to capture the spatial variability of aboveground biomass within coastal wetlands and across larger, regional spatial scales using moderate resolution imagery. However, as remote sensing technology advances, products of higher spatial, temporal, and spectral resolution are becoming available for wetland applications (Klemas 2013b 2011). These products may be useful in filling data gaps that arise from the tradeoffs in spatial and temporal resolution inherent to satellite remote sensing.

Unmanned Aerial Vehicles (UAVs) are revolutionizing spatial ecology (Anderson and Gaston 2013) and can facilitate high-resolution monitoring of coastal wetlands (Klemas 2015; Pereira et al. 2009). With recent advances in platform and sensor technologies, UAVs provide a

low-cost, operationally flexible alternative to traditional satellite and airborne remote sensing, which make them especially useful for small-scale or site-based applications. UAVs have been used in a number of coastal wetland applications at small scales including coastal monitoring (Manfreda et al. 2018; Turner et al. 2016), hazard assessment (Vousdoukas et al. 2011), wetland delineation (Gray et al. 2018; Marcaccio et al. 2015), and vegetation height estimation (DiGiacomo et al. 2020). Biomass quantification using UAVs has been tested in wetland settings containing invasive grasses (Zhou et al. 2018) and mangroves (Navarro et al. 2019; Otero et al. 2018), and in other non-wetland applications (see Poley and Mcdermid 2020 for review).

More recently, UAVs have been applied to the task of quantifying aboveground biomass (AGB) in coastal saltmarshes (Doughty and Cavanaugh 2019). In this application, biomass estimation models based on UAV NDVI accounted for up to 67% of variability in AGB, but model performance varied among seasons. This study was also limited to one saltmarsh site over a single annual growth cycle. Although UAVs have demonstrated potential in estimating coastal wetland biomass, more work is needed to test how transferrable this approach is among wetlands with different plant communities. UAVs could serve as an intermediate between field-based measures of biomass and satellite imagery by providing high-resolution insights into complex spatial patterns in AGB, habitat complexity, and community composition. A comparison of UAV and satellite biomass estimation approaches is needed to see if UAV imagery can be used to supplement traditional satellite-based approaches.

The overarching aim of this study is to test the feasibility of using UAV-based approaches to map coastal wetland biomass across spatial scales. First, we test biomass estimation using UAVs at fine scales ($\leq$ 1m) within four tidal wetland sites within the southern California region. By using wetlands of varying setting, size, and plant communities, we can also identify factors that

contribute to variability in biomass modelling across sites. Second, we compare how the spatial resolution of high- and moderate-resolution imagery can influence biomass estimation by comparing UAV and Landsat approaches at each site. This comparison allows us to quantify spatial heterogeneity and patterns in AGB detected using imagery of differing resolutions. Overall, this study provides the first quantitative comparison of UAV and Landsat biomass estimation approaches in coastal wetlands. This is an essential first step in testing a novel remote sensing technology in its ability to capture wetland biomass at ecologically relevant scales and its potential in supplementing satellite-based approaches.


**Figure 3-2. Study site locations in southern California, USA with site symbology indicating wetland archetypes (A). Overviews of wetland areas and UAV survey areas (red outline) for (B) Carpinteria Salt Marsh Reserve, (C) San Dieguito Lagoon, (D) Los Peñasquitos Lagoon, and (E) Kendall-Frost Mission Bay Marsh Reserve. Gray basemap ©ESRI. Satellite imagery basemap ©Google.**

## 3.3 Methods

### *3.3.1 Site Description*

We conducted field surveys in four intertidal wetland sites in southern California near the end of the region's growing season during August – September of 2018 and 2019 (Figure 3-2, Table S3-1). Field sites included the Carpinteria Salt Marsh Reserve (CSMR), San Dieguito Lagoon (SDL), Los Peñasquitos Lagoon (LPL), and Kendall-Frost Mission Bay Marsh Reserve (KFMR). These sites represent two wetland types in the region, large river valley estuaries and intermittently open estuaries (Doughty et al. 2018; SCWRP 2018; Stein et al. 2019). Plant community composition differs among sites and reflects a range of common species throughout this region). Site selection was based on access to protected wetland areas and FAA airspace restrictions. At each site, field surveys consisted of UAV flights followed by biophysical surveys of wetland vegetation.

### *3.3.2 UAV Imagery Collection and Processing*

We performed UAV flights using a DJI Matrice 100 quadcopter (DJI, Nanshan, Shenzhen, China). Dates and times of UAV flights at each site were chosen to coincide with Landsat overpasses and flights were conducted within two hours of solar noon (Tagle et al. 2017). The Matrice was equipped with a Micasense Rededge multispectral sensor (Micasense, Seattle, WA), which captures five spectral bands: blue (475 nm, 20 nm bandwidth), green (560 nm, 20 nm bandwidth), red (668 nm, 10 nm bandwidth), red edge (717 nm, 10 nm bandwidth), and the near-infrared (840 nm, 40 nm bandwidth). We used the Rededge sensor to capture images of Micasense Calibrated Reflectance Panels before and after each flight for radiometric conversion of UAV images. UAV flight plans were created using Micasense Atlas Flight Software and flights were

**Table 3-1. Common species present in field biomass assessment plots (25 x 25 cm). Frequency provides the count of plots where each species was present. Mean percent cover is the average across all plots in which a species was present.**

| Species | Vegetation Type | Frequency | | | | | Mean Percent Cover (%) | | | | |
|---|---|---|---|---|---|---|---|---|---|---|---|
| | | CSMR | KFMR | SDL | LPL | Total | CSMR | KFMR | SDL | LPL | Total |
| *Salicornia pacifica (Sp)* | Succulent perennial herb | 10 | 6 | 7 | 8 | 31 | 44 | 32 | 28 | 36 | 36 |
| *Arthrocnemum subterminale (As)* | Succulent perennial herb | 2 | 0 | 1 | 0 | 3 | 65 | 0 | 5 | 0 | 45 |
| *Jaumea carnosa (Jc)* | Succulent perennial herb | 8 | 1 | 6 | 8 | 23 | 82 | 1 | 50 | 58 | 62 |
| *Salicornia bigelovii (Sb)* | Succulent perennial herb | 0 | 4 | 0 | 0 | 4 | 0 | 55 | 0 | 0 | 55 |
| *Batis maritima (Bm)* | Succulent perennial herb | 0 | 9 | 0 | 0 | 9 | 0 | 34 | 0 | 0 | 34 |
| *Frankenia salina (Fs)* | Perennial herb | 5 | 1 | 0 | 8 | 14 | 17 | 5 | 0 | 56 | 39 |
| *Distichlis littoralis (Dl)* | Perennial grass | 3 | 2 | 1 | 0 | 6 | 22 | 65 | 80 | 0 | 46 |
| *Distichlis spicata (Ds)* | Perennial grass | 1 | 2 | 3 | 1 | 7 | 10 | 50 | 23 | 90 | 39 |
| *Limonium californicum (Lc)* | Perennial herb | 2 | 1 | 0 | 0 | 3 | 55 | 60 | 0 | 0 | 57 |
| *Spartina foliosa (Sf)* | Perennial grass | 0 | 6 | 6 | 0 | 12 | 0 | 40 | 46 | 0 | 43 |
| *Triglochin concinna (Tc)* | Perennial herb | 0 | 1 | 0 | 0 | 1 | 0 | 2 | 0 | 0 | 2 |
| *Atriplex prostrata (Ap)* | Non-native annual herb | 0 | 0 | 0 | 3 | 3 | 0 | 0 | 0 | 53 | 53 |
| *Cuscuta salina (Cs)* | Annual herb or vine (parasitic) | 2 | 0 | 0 | 1 | 3 | 1 | 0 | 0 | 40 | 14 |

Abbreviations: Carpinteria salt marsh reserve (CSMR), Kendall-Frost Mission Bay Marsh Reserve (KFMR), San Dieguito Lagoon (SDL), Los Peñasquitos Lagoon (LPL)

conducted at an altitude of 90 m above ground level, at an airspeed of 7 m $s^{-1}$, and with image overlap set to 75%. Doughty & Cavanaugh (2019) provides a thorough overview of the UAV data collection and processing workflow.

UAV images were converted to reflectance using scripts adapted from Micasense (Doughty 2019). First, images were corrected for dark pixels, vignette effects, exposure, and gain. Corrected images were then converted from raw digital number (DN) to radiance and from radiance to reflectance using a conversion factor calculated from the preflight and postflight calibration panel images. UAV images of reflectance were then mosaicked to generate multispectral orthomosaics using Photoscan Pro v1.4 (Agisoft, St. Petersburg, Russia). Resulting 5-band orthomosaics were produced for each site with pixel resolutions averaging ~6 cm.

Orthomosaics were masked to wetland UAV survey areas (Figure 3-2; red outlines) and resampled to 1-m pixel resolutions. Masked orthomosaics were used to create maps of the normalized difference vegetation index (NDVI). NDVI was used as the focal vegetation index for estimating aboveground biomass using UAVs based on prior findings at CSMR (Doughty and Cavanaugh 2019). We extracted mean reflectance and NDVI values from the UAV-derived imagery that coincided with sampling plot locations from the biophysical surveys. Data was extracted from a circular area surrounding each plot that accounted for plot width (25 cm) plus the horizontal error of the RTK-GPS and the orthomosaic that varied for each site (Table S3-1); the circular area ranged in diameter from 1.09 – 1.37 m per site. All orthomosaic processing and analyses were conducted in R using base (v4.0.0), raster (v3.0-2), and stats (v3.6) packages (R Foundation for Statistical Computing, Vienna, Austria).

### *3.3.3 In Situ Biophysical Surveys*

Following UAV flights, we conducted biophysical surveys of the wetland vegetation at each site. Because the timing of field surveys was primarily done to coincide with Landsat overpasses and be within two hours of solar noon, tidal levels ranged from 0.70 – 1.25 m NAVD88 at the time of field sampling (Table S3-1). The location and sampling design of plots were selected based on elevation and Landsat pixel footprints of 30 m x 30 m (Figure 3-3). Plot placements were guided by elevational gradients at each site to ensure that we captured a variety of common wetland species in the region (Table 3-1). Site SDL contained a sharp elevational gradient over a small area; therefore, sampling design at SDL was perpendicular to the elevational gradient, unlike other sites where we sampled along elevational gradients (Figure 3-3A). Despite this alternative sampling design, we captured the range of species occurring at different elevations within SDL. We used elevation data from the NOAA-CA Coastal Conservancy Coastal LiDAR project 2009–2013, available as a 1-$m^2$ resolution digital elevation model (DEM) to measure elevation (m NAVD88) for each site. SDL mean elevation was 1.60 ± 0.29 m (1.15 – 2.16 m); KFMR mean elevation was 1.27 ± 0.53 m (0.03 – 5.65 m); CSMR mean elevation was 1.85 ± 0.26m (0.61 – 3.37 m); and LPL mean elevation was 1.88 ± 0.20 m (0.99 – 2.44 m) (Table S3-1; Figure S3-1). We selected Landsat pixels across these elevational gradients that also represent a range of vegetation "greenness" estimated from Landsat NDVI imagery taken in August - September from previous years. Five to six Landsat pixels were selected for each site based on these criteria and site size.

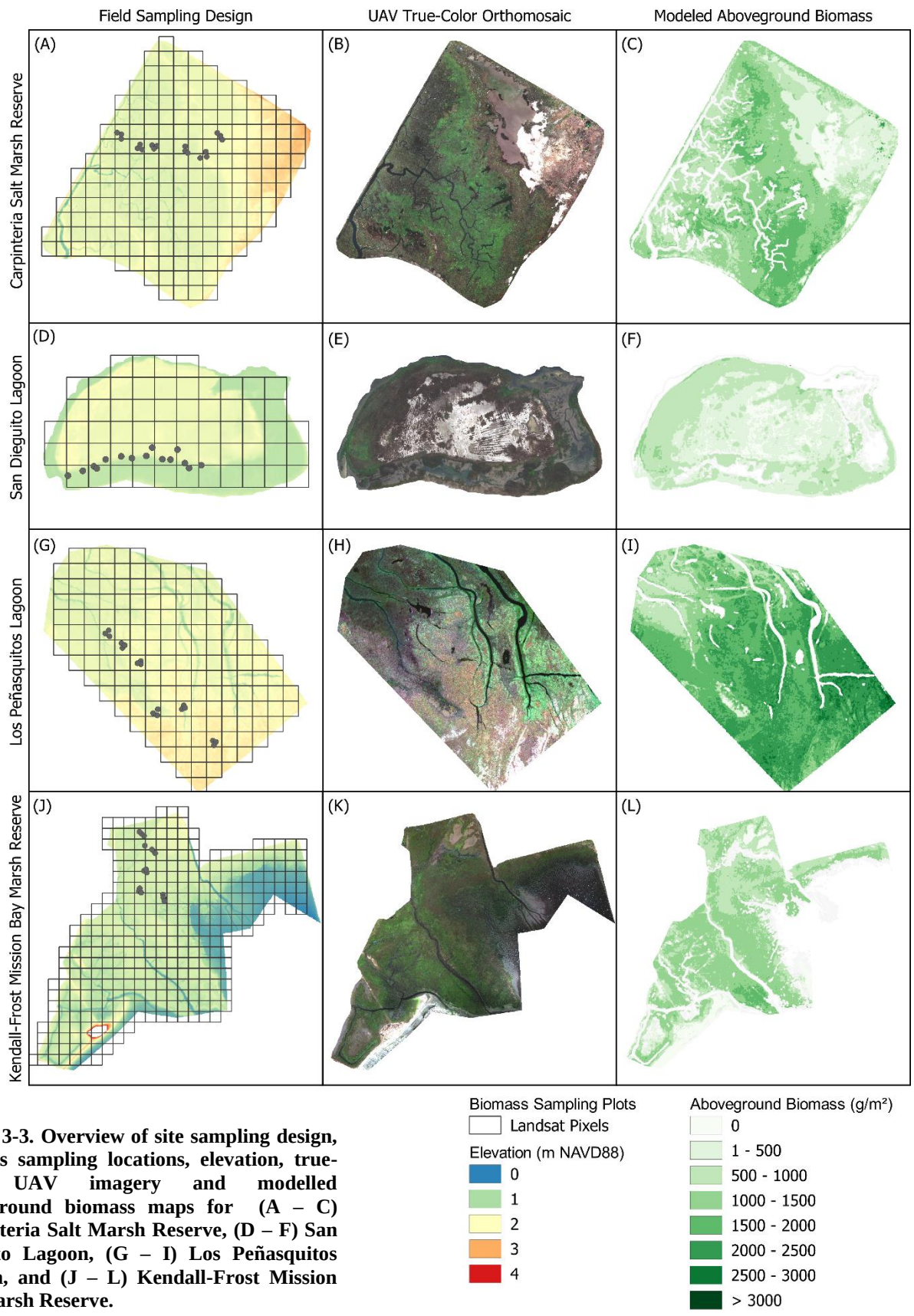


**Figure 3-3. Overview of site sampling design, biomass sampling locations, elevation, true-color UAV imagery and modelled aboveground biomass maps for (A – C) Carpinteria Salt Marsh Reserve, (D – F) San Dieguito Lagoon, (G – I) Los Peñasquitos Lagoon, and (J – L) Kendall-Frost Mission Bay Marsh Reserve.**

Within each of the selected 30-m Landsat pixels, we randomly placed three 25 x 25 cm sampling plots approximately 7 m apart around the pixel centers. The total number of plots per site ranged from 15 – 18. We measured the coordinates of plot centers using an Arrow Gold RTK-GPS with ~3 cm horizontal accuracy and ~5 cm vertical accuracy (EOS Positioning System, Terrebonne, QC, Canada). We estimated species percent cover and average vegetation height taken from three random samples within the plots, before harvesting all aboveground biomass. Aboveground biomass samples were dried at 50°C for one week to obtain dry weight (g).

### *3.3.4 Landsat Imagery Acquisition and Processing*

Landsat Collection-1 tier-1 Surface Reflectance products were downloaded through the USGS Earth Explorer (https://earthexplorer.usgs.gov/). We selected cloud-free Landsat 8 OLI scenes acquired within 0 – 18 days of field surveys (Table S3-1). Although field surveys were timed to coincide with Landsat satellite overpasses, some Landsat scenes were excluded from the analysis due to high cloud cover. Landsat OLI bands used in this study include blue (450 – 515 nm), green (525 – 600 nm), red (630 – 680 nm), and near-infrared (845 – 885 nm). Tier-1 Landsat 8 OLI imagery ground resolution is 30 m with ≤ 12 m circular geolocation error uncertainty (Roy et al. 2014). Landsat images were masked to wetland UAV survey areas for each site (Figure 3-2; red outlines) and converted to NDVI. All Landsat imagery processing and analyses were also conducted in R.

### *3.3.5 Biomass Model Development*

To study the effects of spatial resolution on AGB estimation, we developed models based on three remotely sensed datasets: UAV NDVI (1 m), Landsat NDVI (30 m), and a combination of Landsat NDVI and upscaled UAV AGB maps (30 m). For each biomass estimation approach, we used simple linear regression and reported the coefficient of determination ($r^2$), root mean

square error (RMSE) and Akaike information criterion (AIC) to aid model comparisons among sites and approaches.

#### *3.3.5.1 Biomass Estimation from UAV NDVI*

We developed linear regression models using estimates of aboveground biomass collected *in situ* and NDVI derived from UAV imagery at sampling plot locations. Simple linear regression was used, as this method is common for estimating marsh biomass with multispectral sensors (Hardisky et al. 1983; Mo et al. 2018; Zhang et al. 1997), and because our previous work in the region showed no saturation of broadband vegetation indices with increasing aboveground biomass (Doughty and Cavanaugh 2019). NDVI was selected as the focal vegetation index in this study because it is widely used in remote quantification of wetland biomass (Klemas 2013a) and because NDVI adequately modeled biomass in previous studies at CSMR (Doughty and Cavanaugh 2019). We did test other indices in this study and found that NDVI performed consistently better when comparing across sites (Table S3-2). Thus, linear models based on NDVI were developed for each site and for all pooled data. Site-specific models were used to create AGB maps used below in the approach combining Landsat NDVI and UAV biomass maps.

In addition to comparing biomass models among different wetland sites, we also tested the impacts of dominant vegetation cover type on the ability to model aboveground biomass using simple linear regression.

#### *3.3.5.2 Biomass Estimation from Landsat NDVI*

To test the impact of sensor resolution, we developed biomass models from the *in situ* biomass collections and Landsat NDVI. Similar to the biomass estimation approach using UAV imagery, mean NDVI values were extracted from the Landsat NDVI raster within a 30-m buffer area surrounding each sampling plot that accounted for plot size, Landsat resolution, and horizontal

error (±12 m) Landsat imagery. Simple linear regression models were then used to test the correlation among *in situ* aboveground biomass and Landsat NDVI among sites and approaches.

#### *3.3.5.3 Biomass Estimation Combining Landsat NDVI and UAV Aboveground Biomass*

Last, we developed biomass models based on UAV-derived maps of AGB and Landsat NDVI. UAV biomass maps were created using site-specific AGB models described above. UAV biomass maps were upscaled from 1-m to 30-m spatial resolutions using a bilinear raster resampling method, which calculates the mean AGB of 900 UAV pixels contained within each Landsat pixel. The resulting resolution and extent of upscaled UAV AGB rasters match Landsat NDVI rasters. We then used the pixelwise comparisons of UAV-modeled AGB and Landsat NDVI to develop biomass models using simple linear regression.

### *3.3.6 Spatial Heterogeneity Analysis*

To compare the spatial scale at which each sensor can detect variability, patterns, and features in coastal wetland vegetation, we used semivariogram analysis on AGB maps derived from UAV and Landsat imagery. Semivariograms provide a representation of spatial variability and autocorrelation in a dataset (Atkinson 1993; Cohen et al. 1990). The amount of variability can be quantified as semivariance ($\gamma$(h)), calculated as:

$$\gamma(h) = \frac{1}{2n}\sum\{z(x) - z(x+h)\}^2 \quad \text{(Eq. 1)}$$

Where $\gamma$(h) estimates the variability in aboveground biomass (z) as a function of separation in space (x) over a given lag distance (h) (Curran 1988). Semivariance has a dimension of units squared (Palmer 2002), therefore the units for semivariance of AGB presented here is $g^2\ m^{-4}$.

Empirical semivariograms can be developed using either transect or matrix sampling methods (Cohen et al. 1990). Matrix semivariograms evaluate raster images in 2-dimensions,

which permits a more complete, accurate assessment of habitat structure, while transect semivariograms based on 1-dimensional data are more useful for estimating habitat features like tree canopy size, gaps, and patterns in stand structure (Cohen et al. 1990). We opted for a matrix semivariogram approach performed on a 60-m wide spatial subset of each site that aligns with the field sampling design across an elevational gradient. This was done in order to simplify the spatial variability in multiple dimensions, so that habitat features could be inferred from the AGB maps in addition to overall habitat structure. This also allows us to analyze all sites, despite the different sampling design required at SDL. We implemented the R package "usdm" (v1.1-18) to perform the variogram analysis on raster data of UAV and Landsat maps of AGB (Naimi et al. 2011). Lag distance intervals were set to the resolution of UAV (1 m) and Landsat (30 m) imagery. Maximum lag distances analyzed for each site were half of the total transect length (100 – 250 m), because with greater lag distances, there is greater uncertainty and noise due to fewer available data pairs (Palmer 2002). Resulting semivariograms show semivariance of AGB over increasing lag distance for imagery type.

Semivariograms were then used to interpret the scales and patterns of spatial variability in each site. The overall form of the variogram summarizes spatial variability of the plant community, and noise within the variogram represents fine-scale variation arising from habitat features (See Curran 1988 for an overview of semivariogram forms). For "classical" semivariogram forms following a spherical model, semivariance increases as a distance decay function of lag distance. From this form it is possible to estimate the "sill", the maximum amount of variability detectable with increasing distance, and the "range", the lag distance at which the sill is reached (Cohen et al. 1990). We were able to estimate range where the semivariogram first begins to flatten for some sites. If semivariograms exhibited fine-scale variation indicative of habitat features, we compared

these to observations of habitat features, such as vegetation patch size or marsh zone width, taken from the field or from UAV true-color imagery.

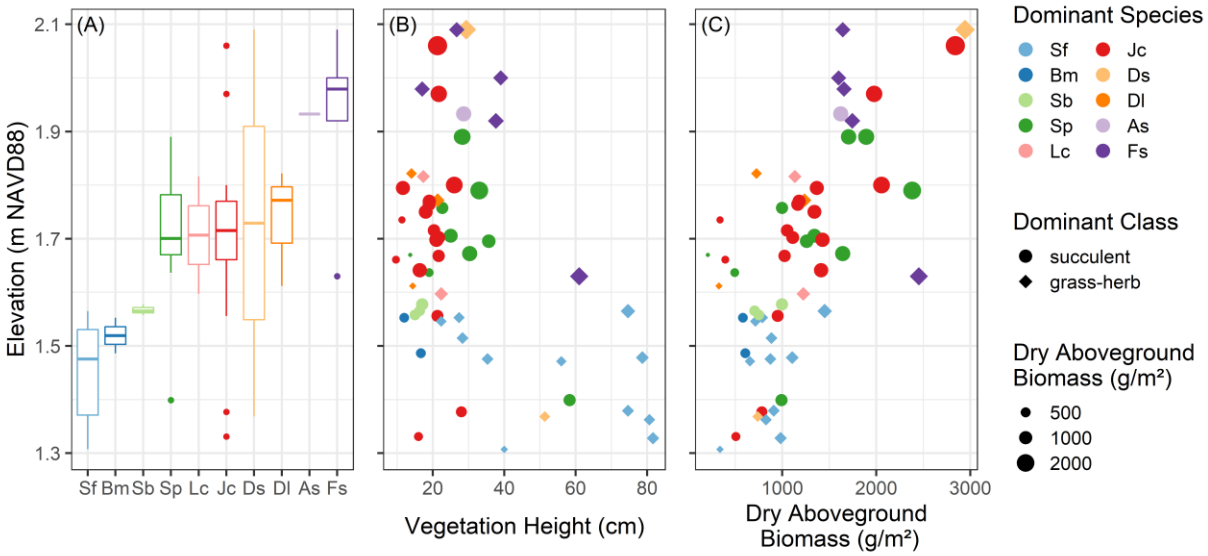


**Figure 3-4. Biophysical survey data on (A) species realized niches, (B) vegetation height and (C) aboveground biomass according to elevation. Dominant species reflect the highest percent cover within plots: Salicornia pacifica (Sp), Arthrocnemum subterminale (As), Jaumea carnosa (Jc), Salicornia bigelovii (Sb), Batis maritima (Bm), Frankenia salina (Fs), Distichlis littoralis (Dl), Distichlis spicata (Ds), Limonium californicum (Lc) and Spartina foliosa (Sf).**

## 3.4 Results

### *3.4.1 Variability in Wetland Vegetation Captured with Field Surveys*

Field surveys showed that plant community composition of vegetation types and species varied among sites (Table 3-1). Dominant vegetation types were most clearly different at CSMR, which was dominated by succulent vegetation and contained some *Distichlis* grass species but no *Spartina foliosa* within survey areas. California cordgrass, *S. foliosa*, was common in KFMR and SDL, which were dominated by grasses, however, SDL exhibited lower species diversity overall (Table 3-1). SDL has undergone recent restoration efforts in areas along the northern arm of the marsh creek (Figure 3-2C), which limited field surveys to a relatively small area containing pre-existing native plant communities (Figure 3-3D). Site LPL contained an even mix of grasses and

succulent species, but grasses occurred at higher mean percent cover in plots they occupied (Table 3-1). LPL, however, was also the only site where the non-native herbaceous species *Atriplex prostrata* was found in plots at higher elevations (Figure 3-4A).

Vegetation types and dominant species that comprised differing plant communities among sites also contributed to site-specific differences in plant height and AGB. Differences in *in situ* AGB were significant across sites, while vegetation height was not (Table 3-2). Overall, the average height of succulent perennials was 22.5 ± 9.1 cm (9.7 – 58.3 cm) and AGB was 1153.1 ± 587.7 g $m^{-2}$ (209.6 – 2841.6 g $m^{-2}$). For perennial herbs and grasses, average height was 44.4 ± 23.6 cm (14.0 – 81.7 cm) and AGB was 1283.5 ± 660.8 g $m^{-2}$ (326.4 – 2944.0 g $m^{-2}$). AGB was not significantly different among vegetation types, but average height did vary significantly among succulents and grasses-herbs ($t = -3.98$, $df = 34.3$, p-value < 0.0005; unpaired t-test; log-transformed for normality and homogeneity).

**Table 3-2. Mean height and aboveground biomass (± standard deviation) of dominant vegetation classes per site. Superscripts denote means differ significantly within each row (P < 0.05).**

| | CSMR | KFMR | SDL | LPL | Total |
|---|---|---|---|---|---|
| **Height (cm)** | | | | | |
| Succulent perennial | 22.8 ± 6.4 | 22.6 ± 17.6 | 17.0 ± 6.3 | 24.4 ± 5.2 | 22.5 ± 9.1 |
| Perennial herb-grass | 18.6 ± 2.4 | 39.4 ± 24.2 | 55.2 ± 26.5 | 38.7 ± 13.5 | 44.4 ± 23.6 |
| **Aboveground Biomass (g $m^{-2}$)** | | | | | |
| Succulent perennial | 1286.1 ± 221.7$^{a}$ | 773.1 ± 182.8$^{b}$ | 562.2 ±259.3$^{b}$ | 1922.2 ± 536.4$^{c}$ | 1153.1 ± 587.7 |
| Perennial herb-grass | 1342.9 ± 277.3$^{a}$ | 879.8 ± 339.6$^{a}$ | 787.0 ± 248.9$^{a}$ | 2077.1 ± 595.5$^{b}$ | 1283.5 ± 660.8 |

Comparing plant height and AGB field data to elevation provided insights into the spatial complexity of wetland vegetation properties within study sites (Figure 3-4). Species elevational ranges indicate the realized elevational niches of common wetland species throughout the region (Figure 3-4A), with some species like *D. spicata* capable of occupying broader elevational ranges. Vegetation heights decreased with elevation (Figure 3-4B), whereas aboveground biomass increased with elevation (Figure 3-4C). Spatial complexity within wetlands and site-specific differences throughout a region are important considerations for remote biomass estimation.

### *3.4.2 Site-specific UAV Biomass Estimation*

Site and vegetation type play a significant role in developing models to estimate end-of-season AGB using multispectral UAV imagery (Figure 3-5). Three of four site-specific relationships among wetland AGB and NDVI have similar slopes, indicating a similar rate of change in AGB associated with NDVI values for LPL, CSMR, and KFMR (Figure 3-5A, Table 3-3A). Slopes for these sites ranged from 3153.2 - 4351.9 g $m^{-2}$ $NDVI^{-1}$, whereas the slope for SDL was 1838.0 g $m^{-2}$ $NDVI^{-1}$. AGB models also indicate site-specific differences in the magnitude of aboveground biomass. For example, LPL had consistently higher biomass for all NDVI values compared to the other sites, and LPL also had significantly higher field biomass than other sites (Table 3-2). When data was pooled for all sites, the biomass estimation model accounted for 40% of the variation in measured AGB (RMSE = 534.6 g $m^{-2}$), compared to 48 – 79% of variance explained in site-specific models (Table 3-3A).

Linear models were considerably different for grasses and herbs (AGB=4760.4*NDVI-700.1; $r^2$ = 0.36; RMSE = 516.7 g $m^{-2}$; Figure 3-5B, Table S3-3) versus succulent vegetation (AGB=1941.4*NDVI+354.4; $r^2$ = 0.08; RMSE = 555.9 g $m^{-2}$). The linear model for succulents explains only 8% of variability in AGB.

### *3.4.3 A Comparison of UAV and Landsat Aboveground Biomass Estimation Approaches*

Aboveground biomass estimation models based on field biomass data and high-resolution UAV imagery outperformed models based on moderate resolution Landsat imagery (Figure 3-6A-B, Table 3). Models based on pooled data for all sites explained 40% of the variability in AGB using UAV imagery, while a similar model using Landsat explained only 26% of variability. Larger uncertainty in the Landsat-based model reflects poor correlation in site-specific models. For example, SDL model correlation was weak and not significant ($r^2$ = 0.06; RMSE = 297.5 g $m^{-2}$), compared to the UAV-based model for SDL ($r^2$ = 0.48; RMSE = 220.5 g $m^{-2}$). We found different linear relationships in UAV and Landsat models for SDL and LPL. Both UAV- and Landsat-based models for LPL performed well, explaining 79% and 67% of variability, but slopes were significantly different between the Landsat and UAV models (Figure 3-6). UAV-based

Table 3-3A). Slopes for these sites ranged from 3153.2 - 4351.9 g $m^{-2}$ $NDVI^{-1}$, whereas the slope for SDL was 1838.0 g $m^{-2}$ $NDVI^{-1}$. AGB models also indicate site-specific differences in the magnitude of aboveground biomass. For example, LPL had consistently higher biomass for all NDVI values compared to the other sites, and LPL also had significantly higher field biomass than other sites (Table 3-2). When data was pooled for all sites, the biomass estimation model accounted for 40% of the variation in measured AGB (RMSE = 534.6 g $m^{-2}$), compared to 48 – 79% of variance explained in site-specific models (Table 3-3A).

Linear models were considerably different for grasses and herbs (AGB=4760.4*NDVI-700.1; $r^2$ = 0.36; RMSE = 516.7 g $m^{-2}$; Figure 3-5B, Table S3-3) versus succulent vegetation (AGB=1941.4*NDVI+354.4; $r^2$ = 0.08; RMSE = 555.9 g $m^{-2}$). The linear model for succulents explains only 8% of variability in AGB.

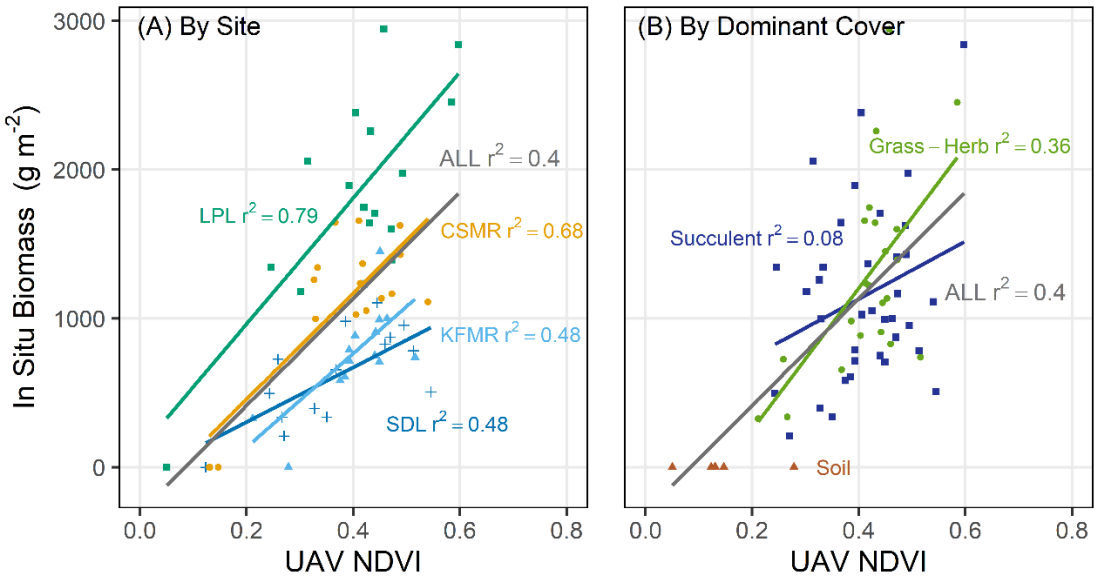


**Figure 3-5. Linear models between in situ aboveground biomass and NDVI derived from UAV imagery: (A) by site, Los Peñasquitos Lagoon (LPL, green squares), Carpinteria Salt Marsh Reserve (CSMR, orange circles), Kendall-Frost Mission Bay Marsh Reserve (KFMR, light blue triangles) and San Dieguito Lagoon (SDL, dark blue cross); and (B) by dominant cover classes, succulents (navy squares), grass-herbs (green circles), and soil (brown triangles). Linear model for all data is shown in grey.**

### *3.4.3 A Comparison of UAV and Landsat Aboveground Biomass Estimation Approaches*

Aboveground biomass estimation models based on field biomass data and high-resolution UAV imagery outperformed models based on moderate resolution Landsat imagery (Figure 3-6A-B, Table 3). Models based on pooled data for all sites explained 40% of the variability in AGB using UAV imagery, while a similar model using Landsat explained only 26% of variability. Larger uncertainty in the Landsat-based model reflects poor correlation in site-specific models. For example, SDL model correlation was weak and not significant ($r^2$ = 0.06; RMSE = 297.5 g $m^{-2}$), compared to the UAV-based model for SDL ($r^2$ = 0.48; RMSE = 220.5 g $m^{-2}$). We found different linear relationships in UAV and Landsat models for SDL and LPL. Both UAV- and Landsat-based models for LPL performed well, explaining 79% and 67% of variability, but slopes were significantly different between the Landsat and UAV models (Figure 3-6). UAV-based

**Table 3-3. Linear models of aboveground biomass derived when (A) in situ biomass is compared to NDVI derived from UAV imagery, (B) in situ aboveground biomass is compared to NDVI derived from Landsat imagery, and (C) modeled aboveground biomass from UAV imagery is compared to NDVI derived from Landsat imagery. Site abbreviations: Los Peñasquitos Lagoon (LPL), Carpinteria Salt Marsh Reserve (CSMR), Kendall-Frost Mission Bay Marsh Reserve (KFMR), and San Dieguito Lagoon (SDL).**

**A. Field biomass to UAV**

| Site | Equation | $r^2$ | RMSE (g $m^{-2}$) | AIC | p-value |
|---|---|---|---|---|---|
| SDL | 1838*NDVI - 63.4 | 0.48 | 220.5 | 210.4 | < 0.005 |
| KFMR | 3153.2*NDVI - 496.2 | 0.48 | 241.1 | 213.1 | < 0.005 |
| CSMR | 3567*NDVI - 255.9 | 0.68 | 293.8 | 261.7 | < 0.005 |
| LPL | 4351.9*NDVI + 63.9 | 0.79 | 398.0 | 272.6 | < 0.005 |
| ALL | 3368.4*NDVI - 210.2 | 0.40 | 534.6 | 1022.5 | < 0.005 |

**B. Field biomass to Landsat**

| Site | Equation | $r^2$ | RMSE (g $m^{-2}$) | AIC | p-value |
|---|---|---|---|---|---|
| SDL | -724.8*NDVI + 753.6 | 0.06 | 297.5 | 219.4 | 0.37 |
| KFMR | 3396.4*NDVI - 873.7 | 0.39 | 259.4 | 215.3 | 0.012 |
| CSMR | 3501.5*NDVI - 509.5 | 0.56 | 345.7 | 267.5 | < 0.005 |
| LPL | 25541.3*NDVI - 11618.3 | 0.67 | 495.6 | 280.5 | < 0.005 |
| ALL | 2338.3*NDVI + 74.4 | 0.26 | 596.8 | 1037.0 | < 0.005 |

**C. Modeled biomass to Landsat NDVI**

| Site | Equation | $r^2$ | RMSE (g $m^{-2}$) | AIC | p-value |
|---|---|---|---|---|---|
| SDL | 494.7*NDVI + 301.3 | 0.13 | 143.1 | 733.6 | 0.005 |
| KFMR | 2061.6*NDVI - 180.1 | 0.63 | 172.8 | 3488.7 | < 0.005 |
| CSMR | 2940.1*NDVI - 381.2 | 0.73 | 201.7 | 2844.3 | < 0.005 |
| LPL | 7630.7*NDVI - 2263.1 | 0.56 | 269.7 | 2223.2 | < 0.005 |
| ALL | 2856.7*NDVI - 284.7 | 0.45 | 400.5 | 10249.0 | < 0.005 |

models for CSMR and KFRM also outperformed Landsat-based models, but differences in models among imagery type were less evident.

Aboveground biomass models derived from a combination of UAV-based AGB maps and Landsat NDVI showed improved model performance compared to the Landsat model calibrated with *in situ* data (Figure 3-6C, Table 3-3C). Models based on pooled data for all sites using the combined approach increased the explained variance from 26% to 45%. Overall, biomass estimation combining Landsat NDVI and UAV aboveground biomass increased explained

variability at an average of 11% (7% - 24%) for all sites compared to using Landsat alone. LPL was the only site where biomass estimation from Landsat outperformed biomass estimation combining Landsat NDVI and UAV AGB maps. RMSE estimates were lower than other approaches indicating that the additional data provided by UAV AGB maps reduce model error, *i.e.*, data were more concentrated along the regression line. However, AIC estimates of model performance are higher than other approaches, which shows that the added UAV AGB data reduces the quality of the statistical model by contributing a larger amount of data for the model to account for (Table 3C). Overall, high-resolution UAV maps of AGB provide additional information to aid in scaling field data to moderate resolution imagery.

### *3.4.4 Increased Spatial Heterogeneity in Aboveground Biomass with Increased Image Resolution*

Detecting spatial heterogeneity in wetland aboveground biomass improved with increased spatial resolution (Figure 3-7). As expected, high-resolution (1 m) maps derived from UAVs captured more variability in AGB than Landsat (30 m), indicating a loss of detail with increased pixel sizes. This is especially important at lag distances smaller than the 30-m resolution of Landsat, where the dissimilarity of wetland characteristics can increase drastically (Figure 3-7B-D). UAVs consistently captured higher semivariance than Landsat at all sites; however, the magnitude of semivariance and form of semivariograms differed among sites and reveal different spatial patterns and features.

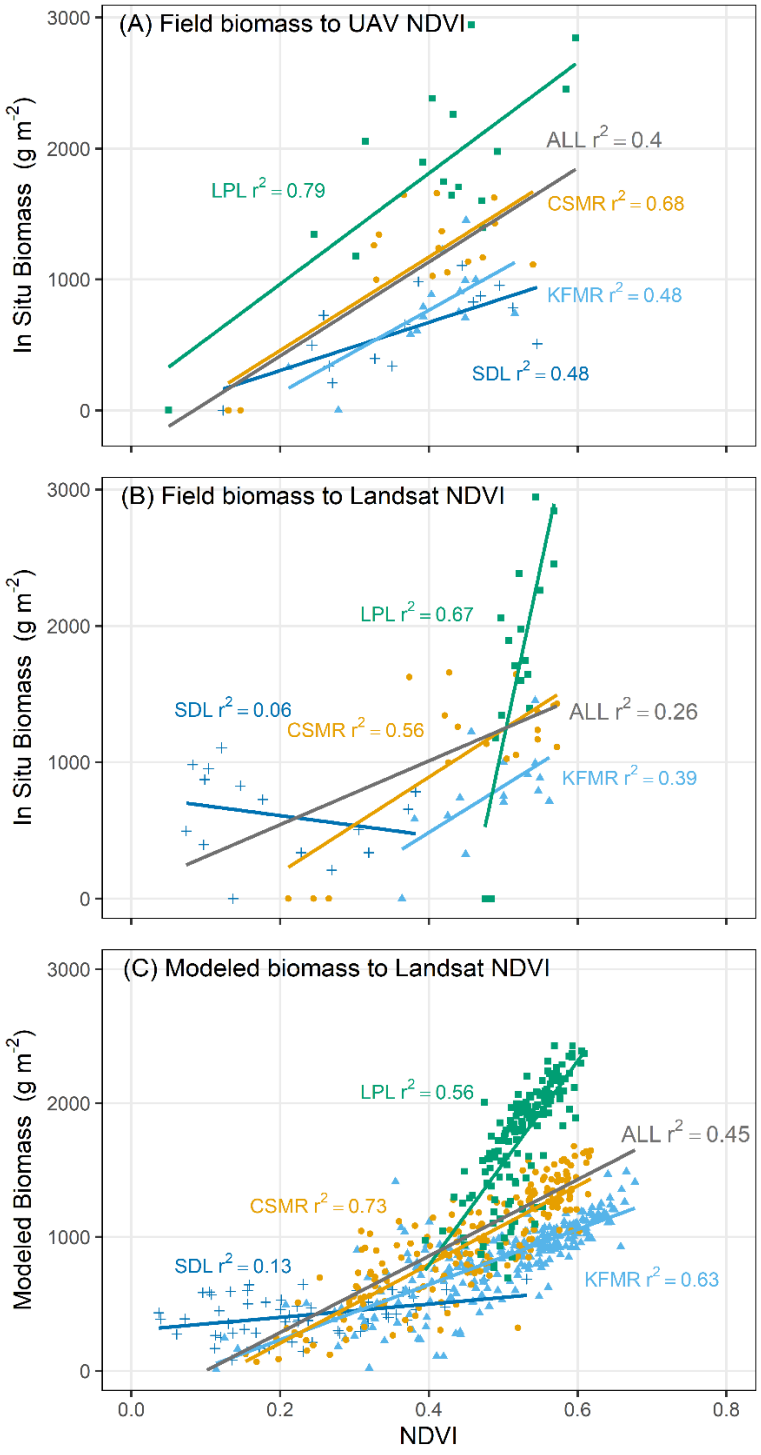


**Figure 3-6. Correlations of aboveground biomass and NDVI when (A) in situ biomass is compared to NDVI derived from UAV imagery, (B) in situ aboveground biomass is compared to NDVI derived from Landsat imagery, and (C) modeled aboveground biomass (using models in panel (A)) is compared to NDVI derived from Landsat imagery. Symbology represents different sites: Los Peñasquitos Lagoon (LPL, green squares), Carpinteria Salt Marsh Reserve (CSMR, orange circles), Kendall-Frost Mission Bay Marsh Reserve (KFMR, light blue triangles), and San Dieguito Lagoon (SDL, dark blue cross).**

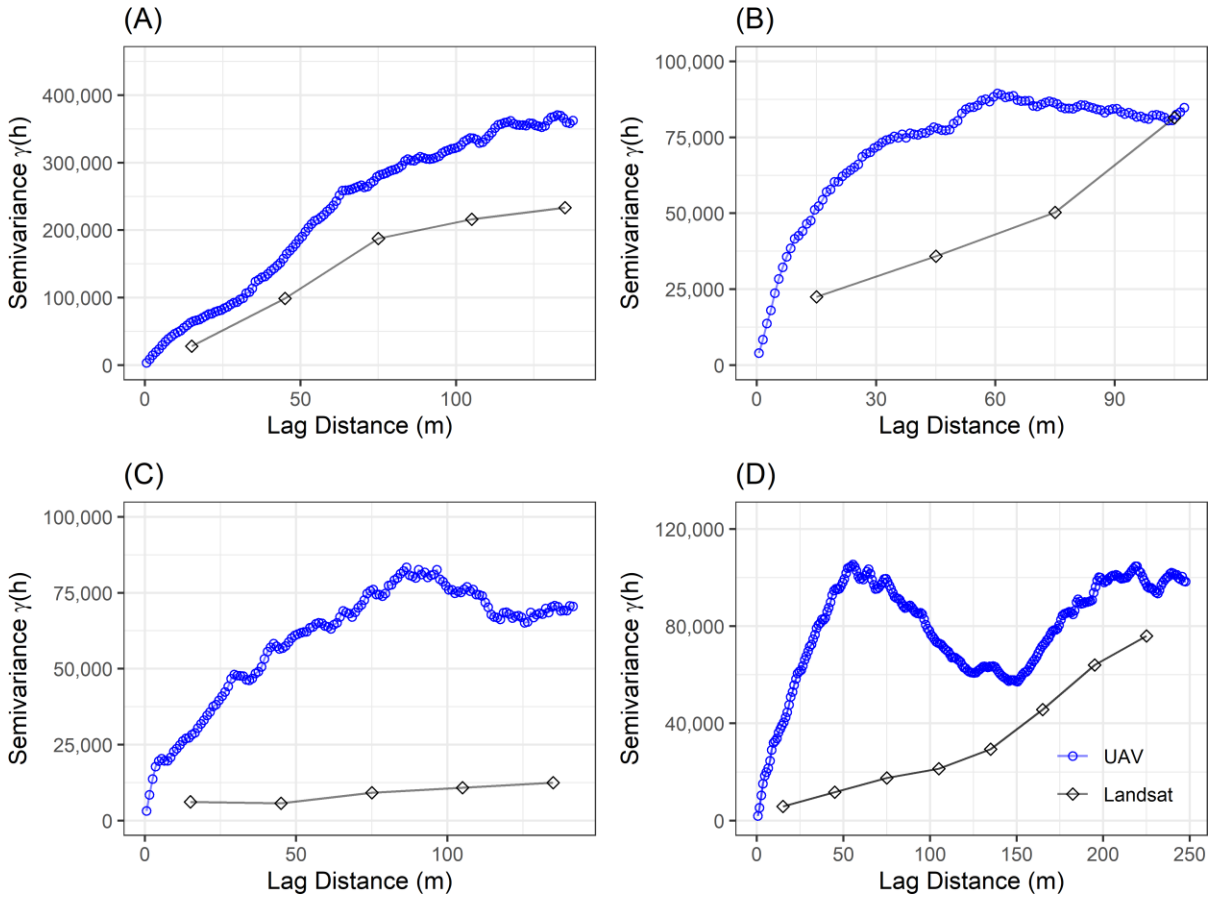


**Figure 3-7. Semivariograms showing the effect of image resolution on detectable variation in aboveground biomass for (A) Carpinteria Salt Marsh Reserve, (B) San Dieguito Lagoon, (C) Los Peñasquitos Lagoon, and (D) Kendall-Frost Mission Bay Marsh Reserve. Semivariance ($\gamma$(h)) for AGB presented as units in g2 m-4.**

CSMR exhibited the highest variability in AGB overall and both UAV and Landsat imagery presented similar semivariogram forms (Figure 3-7A). For both UAV and Landsat, semivariance levels off at ranges of ~75 m and indicates regularly repeated features. This lag distance corresponds to the average width of habitat zones observed at CSMR which are comprised predominately of the succulent *Salicornia pacifica* at low elevations, followed by the succulent *Jaumea carnosa* and a mixed zone dominated by *Distichlis littoralis* grasses at high elevations. The slight depression of the UAV semivariogram at ~30 m could also indicate smaller patch sizes

of vegetation type and canopy gaps (*i.e.* mudflats, ponds) occurring within larger elevational zonation patterns.

For the remaining sites, UAV and Landsat semivariograms exhibited different forms that signify different spatial patterns in AGB derived from the two imagery types. For example, the UAV semivariogram for SDL presents a "classic" form where semivariance quickly increases with lag distance to a range of ~30 m, but the Landsat variogram is unbounded (Curran 1988), meaning the transect length may be too short to reveal a clear pattern using Landsat (Figure 3-7B). UAV AGB maps therefore provide the only insights into wetland features occurring at scales of 30 – 50 m, which correspond to patch sizes of distinguishable cover types: vegetation (green and brown), soils (mudflats and salt flats), and water observed at the site. Slight dips at ~15 m and 25 m could indicate variation within broader cover classes due to patches of vegetation types and/or species. However, given the alternative sampling design at SDL, these patterns cannot be explicitly linked to elevational patterns like marsh zonation.

There was little variability in AGB maps derived from Landsat for LPL revealed by an aspatial relationship with variance over lag distance (Curran 1988), which would indicate a homogeneous surface of AGB at this site (Figure 3-7C). Profiles of AGB along the elevational transect also show little variation in AGB compared to those from UAVs for LPL (Figure S3-1). UAV AGB maps at LPL reveal different spatial patterns with high fine-scale variation indicated by the noisy semivariogram. For example, the UAV variogram for LPL exhibits a clear bump at a ~10 m lag, which corresponds to features occurring within canopies like patches of vegetation type or species, as well as small gaps in cover type (*i.e.*, vegetation, soil, water). High noise in the UAV semivariogram beginning at 30 – 45 m indicates broader patterns of zonation among similar vegetation or cover types discernable in UAV true-color imagery (Figure 3-3H).

Semivariograms for KFMR reveal drastically different spatial patterns in AGB. The Landsat semivariogram is also unbounded with semivariance continuing to increase over the lag distances measured, which indicates spatial dependence at broader spatial scales at this site (Figure 3-7D). The UAV variogram exhibits a periodic, multifrequency form (Curran 1988) with a large inflection at lag distances ~125 – 150 m. This inflection indicates the spatial scale at which we can discern variability within a feature and among features. Lag distances of this size correspond to wider bands of marsh zonation observed at KFMR as this was a large site with a low elevational grade. Peaks around 50 m lag distances reveal repeating patterns within marsh zones arising from patches of cover type (vegetation, soil) and vegetation type (succulents, grasses).

Ranges estimated from the initial leveling off of UAV semivariograms show clear differences in the sizes of detectable patterns at each site. Estimated ranges were ~75 m for CSMR, ~30 m for SDL, ~75 m for LPL and ~50 m for KFMR (Figure 3-7). Site-specific ranges reflect overall differences in the sizes of the largest detectable wetland habitat structures. At CSMR, LPL, and KFMR, 50 – 75 m ranges correspond to larger, intra-site patterns of marsh zonation, whereas the 30 m range detected at SDL indicates smaller intra-site patterns in cover type. SDL was the smallest site and had the smallest elevational range, which may be why cover type and not marsh zonation was the largest detectable pattern with UAVs. At spatial scales smaller than the estimated ranges, the semivariance detected at each site reflects the underlying plant-level characteristics, species composition, vegetation type, and cover type that contribute to overall wetland heterogeneity (Figure 3-1).

### 3.5 Discussion

UAVs are rapidly becoming a valuable tool for wetland ecologists to map and monitor highly dynamic coastal ecosystems. Here we compared the remote estimation of aboveground

biomass in diverse coastal saltmarshes by UAV and Landsat. We found that high-resolution UAV imagery aids biomass estimation modeling across multiple wetland sites with unique vegetation and geomorphic characteristics. UAVs allowed for improved detection of spatial heterogeneity and patterns in community composition, marsh zonation, cover and vegetation type that contribute to wetland aboveground biomass at various scales (Figure 3-1). UAVs served as a viable intermediate between field-based measures of biomass and satellite imagery to improve Landsat-based biomass estimation.

The relationship between aboveground biomass and UAV-based NDVI is site-specific and influenced by plant communities present in wetlands in the southern California region (Figure 3-5). For wetland grasses and herbs, NDVI explained more (36%) of the variability in AGB due to the sensitivity of NDVI to green photosynthetic tissue characteristic of these vegetation types (Klemas 2013a). Common perennial succulents in the region, however, exhibit a wide range of growth forms that made it difficult to model AGB, as NDVI explained only 8% of the variation in aboveground biomass for this vegetation type. Perennial succulents like *S. pacifica* (pickleweed) and *Arthrocnemum subterminale* (Parish's glasswort) can grow into low-lying subshrub forms with multi-stemmed woody plant tissues. Such non-photosynthetic vegetation (NPV) will contribute to standing biomass but will not be adequately modeled using a vegetation index sensitive to green photosynthetic tissue. Conversely, saltmarsh succulents that are primarily composed of soft green tissue, such as *J. carnosa* (fleshy jaumea), may be better suited for AGB estimation modelling using NDVI. Differences in coastal wetland community composition, vegetation types, growth forms, and species contribute uncertainty to aboveground biomass estimation using UAVs, and understanding the variability caused by these factors is essential to improving remote estimation of aboveground biomass.

The increased spatial resolution provided by UAVs in this study improved our ability to model aboveground biomass using NDVI compared to Landsat when based on field biomass data (Figure 3-6A, B). Other studies using Landsat to estimate and model AGB in wetlands based on field measures have been successful using approaches with different focal species, vegetation indices, sensor combinations, and image analyses. Gross *et al.* (1987) provides one of the earliest uses of Landsat TM images to quantify and map biomass in a large, homogenous *S. alterniflora* marsh in Delaware, USA, achieving a strong linear model to predict live AGB from NDVI ($r^2$ = 0.85). Buffington *et al.* (2018) found tassel cap greenness (TCG) to be a useful measure of aboveground biomass ($r^2$ = 0.72) in diverse, productive tidal marsh communities in the Pacific Northwest, USA. In coastal Louisiana, USA, Mo *et al.* (2018) found that it was possible to assess biomass among diverse marsh types using non-linear models combined with hyperspectral data ($r^2$ = 0.85), but not with moderate resolution Landsat. Bryd *et al.* (2014) show that spectral and spatial resolutions of various remotely sensed imagery impact predictive models of aboveground biomass for freshwater marshes in the Sacramento–San Joaquin River Delta, California, USA. They found Landsat was more successful ($r^2$ = 0.55, RMSE = 556.5 g $m^{-2}$) than World View-2 ($r^2$ = 0.45, RMSE = 659.7 g $m^{-2}$). Our study compares imagery of similar resolutions, but our 1-m resampled UAV imagery ($r^2$ = 0.40, RMSE = 534.6 g $m^{-2}$) outperformed Landsat ($r^2$ = 0.26, RMSE = 596.8 g $m^{-2}$). The varying success of biomass estimation among these case studies highlight the importance of the types of remote sensing data and approaches used in estimating biomass in site-specific wetland communities.

Aboveground biomass estimation in coastal wetlands depends largely on the scale of remotely sensed imagery and the scale of site-specific patterns in wetland biomass. For wetlands that are large and homogenous, 30-m Landsat pixels may adequately model AGB (e.g., Gross et

al. 1987; O'Donnell and Schalles 2016), but wetland communities are often heterogeneous and spatially complex (e.g., Buffington et al. 2018; Mo et al. 2018). Wetlands in southern California contain highly diverse plant communities (Table 3-1), but are relatively small and constrained by upland development (Stein et al. 2014; Zedler 1982). Our study sites also represent wetlands with differing geomorphology, elevational ranges, and management and restoration histories. Vegetation patterns that result from these factors are also shaped by additional physical drivers that are unique to this Mediterranean urban landscape, such as drought, El Niño–Southern Oscillation, disrupted river flows, and constant urban runoff. The combination of physical drivers and wetland settings unique to this region create high spatial variability and patterns in AGB that may be better captured with UAV resolutions.

UAV data can be used to scale field data to moderate resolution imagery (Figure 3-6, Table 3-3). In this study, combining UAV-derived AGB maps and Landsat NDVI imagery provided the strongest AGB estimation for the wetland sites overall. A similar "two-step approach" was conducted by O'Donnell and Schalles (2016) in a predominantly *S. alternaflora* marsh in Georgia, USA, where biomass maps derived from hyperspectral imagery (AISA Eagle, 1-m) were used to scale biomass estimation to Landsat TM and the Landsat archive. Their NDVI-based models using AISA ($r^2$ = 0.70) outperformed the combined AISA-Landsat model ($r^2$ = 0.50; O'Donnell and Schalles 2016), whereas our work did show improved model performance using a combined UAV-Landsat approach. This approach may better account for the higher variability in *in situ* AGB because UAVs provide data at the appropriate resolutions needed to capture the high diversity of wetland plant communities and plant characteristics shown through our field surveys (Table 1, 2). The size of biomass sampling plots also align better with the resolutions of UAV imagery than

with Landsat (Figure 3-8), which alleviates issues in scaling field measurements to Landsat pixels (Baccini et al. 2007).

UAVs improved detection of spatial heterogeneity and complexity in patterns of community composition, marsh zonation, cover type, and vegetation type that relate to aboveground biomass (Figure 3-7). Image resolutions determine what wetland features can be inferred from remotely sensed imagery, and increased resolution is key to understanding spatial dependence and variability in spatial datasets (Curran 1988). Higher image resolutions have helped to characterize landscape spatial heterogeneity among broad land uses like urban developments, agriculture, and forest (Garrigues et al. 2006; Silveira et al. 2017) and to detect features such as tree crowns and canopy gaps in mangrove ecosystems (Kamal et al. 2014). Understanding the presence and scale of relevant habitat characteristics is essential to mapping aboveground biomass in any ecosystem (Phinn et al. 1996). Semivariogram analysis indicated that UAVs and Landsat can reveal drastically different spatial patterns and features detectable within and among saltmarsh sites. At smaller scales (< 30 m), the dissimilarity of wetland characteristics can increase drastically (Figure 3-7B-D) and such fine-scale patterns would be undetectable using Landsat. Even at larger scales (50 – 70 m), UAVs did a better job of capturing patterns like wetland zones, features that were not evident with Landsat. Landsat variograms revealed unbounded and aspatial

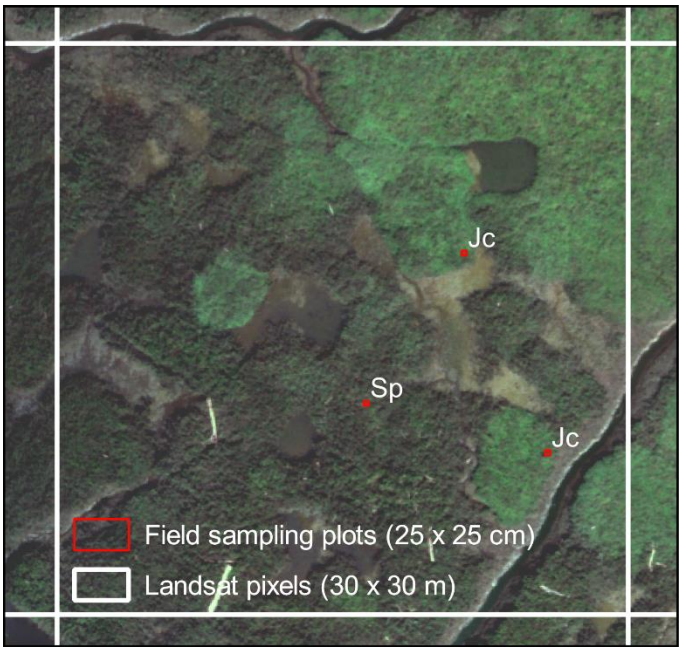


**Figure 3-8. True-color UAV imagery (6-cm resolution) showing spatial patterns in coastal wetland vegetation in relation to field sampling plots (red) and Landsat pixels (white) in the Carpinteria Salt Marsh Reserve.**

patterns at three of four study sites (Figure 3-7), despite these sites being relatively larger wetlands in the southern California region. Each type of remotely sensed imagery can provide insights into spatial variability at the appropriate spatial scales to detect patterns related to wetland AGB (Figure 3-1A). UAVs and Landsat can help describe ecological patterns in structure, zonation, and composition of wetland plant communities that occur on different spatial and temporal scales and influence our ability to model aboveground biomass.

UAVs provide high-resolution insights into wetland habitat complexity and AGB that can improve biomass estimation and serve as an intermediate between field-based measures of biomass and commonly used Landsat satellite imagery. *In situ* aboveground biomass was correlated with remotely sensed NDVI across wetland sites in southern California region that contained a diversity of wetland plant communities. Our work shows that UAV technology can help resolve variability in biomass occurring at fine scales that are inherent to salt marsh ecology and that contributes uncertainty to biomass modeling. The additional spatial information provided by UAVs can further elucidate the processes that generate patterns (Palmer 2002), as patterns in wetland biomass are largely driven by spatially and temporally complex interactions among biological and physical drivers (Figure 3-1). Overcoming tradeoffs in spatial and temporal resolution remains a major challenge to elucidating fine-scale patterns in wetland habitat function, complexity, and community composition that contribute to biomass variability. Ongoing improvements to how we remotely estimate aboveground biomass at the scales relevant to the ecological processes controlling bioproductivity and the resulting vegetative patterns in coastal wetlands can ultimately help how we monitor carbon storage, health, and vulnerability to climate change in these valuable ecosystems.

### 3.6 Acknowledgements

We would like to acknowledge the agencies that allowed us to access protected wetland areas to conduct our research. Thanks to the California State Parks San Diego Coast District for permitting access to the Los Peñasquitos Lagoon in the Torrey Pines State Natural Reserve. Thanks to the University of California Natural Reserve System, Andre Brooks (UCSB Carpinteria Salt Marsh Reserve Site Director), and Isabelle Kay (UCSD Kendall-Frost Mission Bay Marsh Reserve Administrative Director and Reserves Manager) for allowing access to CSMR and KFMR wetlands sites. Thanks to Andres Deza (UCSB Marine Science Institute - Carlsbad Field Office and S.O.N.G.S. Mitigation Monitoring Field Research Supervisor-I) for facilitating access to the San Dieguito Lagoon. Special thanks to: Kate Cavanaugh, Elizabeth Fard, Hanfeng Gu, and Madison Feldman of UCLA; Dr. Kellie Uyeda of the Tijuana River National Estuarine Research Reserve; and Andres Deza, Emily Blair, Morgan Tusa, Kendall Hines, Ross Collins, and Cynthia Coria of UCSB Marine Science Institute - Carlsbad Field Office and S.O.N.G.S. Mitigation Monitoring for their help conducting field work.

### 3.7 References

Adam, E., Mutanga, O., Rugege, D., 2010. Multispectral and hyperspectral remote sensing for identification and mapping of wetland vegetation: A review. Wetl. Ecol. Manag. 18, 281–296. https://doi.org/10.1007/s11273-009-9169-z

Anderson, K., Gaston, K.J., 2013. Lightweight unmanned aerial vehicles will revolutionize spatial ecology. Front. Ecol. Environ. 11, 138–146. https://doi.org/10.1890/120150

Atkinson, P.M., 1993. The effect of spatial resolution on the experimental variogram of airborne MSS imagery. Int. J. Remote Sens. 14, 1005–1011. https://doi.org/10.1080/01431169308904391

Baccini, A., Friedl, M.A., Woodcock, C.E., Zhu, Z., 2007. Scaling field data to calibrate and validate moderate spatial resolution remote sensing models. Photogramm. Eng. Remote Sensing 73, 945–954. https://doi.org/10.14358/PERS.73.8.945

Buffington, K.J., Dugger, B.D., Thorne, K.M., 2018. Climate-related variation in plant peak biomass and growth phenology across Pacific Northwest tidal marshes. Estuar. Coast. Shelf Sci. 202, 212–221. https://doi.org/10.1016/j.ecss.2018.01.006

Byrd, K.B., Ballanti, L., Thomas, N., Nguyen, D., Holmquist, J.R., Simard, M., Windham-Myers, L., 2018. A remote sensing-based model of tidal marsh aboveground carbon stocks for the conterminous United States. ISPRS J. Photogramm. Remote Sens. 139, 255–271. https://doi.org/10.1016/j.isprsjprs.2018.03.019

Byrd, K.B., O'Connell, J.L., Di Tommaso, S., Kelly, M., 2014. Evaluation of sensor types and environmental controls on mapping biomass of coastal marsh emergent vegetation. Remote Sens. Environ. 149, 166–180. https://doi.org/10.1016/j.rse.2014.04.003

Cahoon, D.R., Guntenspergen, G.R., 2010. Climate change, sea-level rise, and coastal wetlands. Natl. Wetl. Newsl. 32, 8–12.

Cahoon, D.R., Reed, D.J., Kolker, A.S., Brinson, M.M., Stevenson, J.C., Riggs, S., Christian, R., Reyes, E., Voss, C., Kunz, D., 2009. Coastal Wetland Sustainability, in: Titus, J.G., Anderson, K.E. (Eds.), Coastal Sensitivity to Sea-Level Rise: A Focus on the Mid-Atlantic Region. A Report by the U.S. Climate Change Science Program and the Subcommittee on Global Change Research. U.S. Environmental Protection Agency, Washington DC, pp. 57–72.

Cohen, W.B., Spies, T.A., Bradshaw, G.A., 1990. Semivariograms of digital imagery for analysis of conifer canopy structure. Remote Sens. Environ. 34, 167–178. https://doi.org/10.1016/0034-4257(90)90066-U

Curran, P.J., 1988. The semivariogram in remote sensing: An introduction. Remote Sens. Environ. 24, 493–507. https://doi.org/10.1016/0034-4257(88)90021-1

DiGiacomo, A.E., Bird, C.N., Pan, V.G., Dobroski, K., Atkins-Davis, C., Johnston, D.W., Ridge, J.T., 2020. Modeling salt marsh vegetation height using unoccupied aircraft systems and structure from motion. Remote Sens. https://doi.org/10.3390/rs12142333

Doughty, C., Cavanaugh, K., 2019. Mapping Coastal Wetland Biomass from High Resolution Unmanned Aerial Vehicle (UAV) Imagery. Remote Sens. 11, 540. https://doi.org/10.3390/rs11050540

Doughty, C.L., 2019. Batch processing Micasense images to reflectance (batch-imageprocessing), GitHub repository. [WWW Document]. URL https://github.com/cldoughty/batch-imageprocessing

Doughty, C.L., Cavanaugh, K.C., Ambrose, R.F., Stein, E.D., 2018. Evaluating regional resiliency of coastal wetlands to sea level rise through hypsometry-based modeling. Glob. Chang. Biol. 1–15. https://doi.org/10.1111/gcb.14429

Gallant, A.L., 2015. The challenges of remote monitoring of wetlands. Remote Sens. 7, 10938–10950. https://doi.org/10.3390/rs70810938

Garrigues, S., Allard, D., Baret, F., Weiss, M., 2006. Quantifying spatial heterogeneity at the landscape scale using variogram models. Remote Sens. Environ. 103, 81–96. https://doi.org/10.1016/j.rse.2006.03.013

Goodman, A.C., Thorne, K.M., Buffington, K.J., Freeman, C.M., Janousek, C.N., 2018. El Niño Increases High-Tide Flooding in Tidal Wetlands Along the U.S. Pacific Coast. J. Geophys. Res. Biogeosciences 123, 3162–3177. https://doi.org/10.1029/2018JG004677

Gray, P.C., Ridge, J.T., Poulin, S.K., Seymour, A.C., Schwantes, A.M., Swenson, J.J., Johnston,

D.W., 2018. Integrating drone imagery into high resolution satellite remote sensing assessments of estuarine environments. Remote Sens. 10. https://doi.org/10.3390/rs10081257

Gross, M.F., Hardisky, M.A., Klemas, V., Wolf, P.L., 1987. Quantification of Biomass of the Marsh Grass Spartina altfernifara Loisel Using Landsat Thematic Mapper Imagery. Photogramm. Eng. Remote Sensing 53, 1577–1583.

Hardisky, M.A., Michael Smart, R., Klemas, V., 1983. Growth response and spectral characteristics of a short Spartina alterniflora salt marsh irrigated with freshwater and sewage effluent. Remote Sens. Environ. 13, 57–67. https://doi.org/10.1016/0034-4257(83)90027-5

Janousek, C.N., Buffington, K.J., Thorne, K.M., Guntenspergen, G.R., Takekawa, J.Y., Dugger, B.D., 2016. Potential effects of sea-level rise on plant productivity: Species-specific responses in northeast Pacific tidal marshes. Mar. Ecol. Prog. Ser. 548, 111–125. https://doi.org/10.3354/meps11683

Kamal, M., Phinn, S., Johansen, K., 2014. Characterizing the spatial structure of Mangrove features for optimizing image-based mangrove mapping. Remote Sens. 6, 984–1006. https://doi.org/10.3390/rs6020984

Kearney, M.S., Stutzer, D., Turpie, K., Stevenson, J.C., 2009. The Effects of Tidal Inundation on the Reflectance Characteristics of Coastal Marsh Vegetation. J. Coast. Res. 256, 1177–1186. https://doi.org/10.2112/08-1080.1

Kennedy, R.E., Andréfouët, S., Cohen, W.B., Gómez, C., Griffiths, P., Hais, M., Healey, S.P., Helmer, E.H., Hostert, P., Lyons, M.B., Meigs, G.W., Pflugmacher, D., Phinn, S.R., Powell, S.L., Scarth, P., Sen, S., Schroeder, T.A., Schneider, A., Sonnenschein, R., Vogelmann, J.E., Wulder, M.A., Zhu, Z., 2014. Bringing an ecological view of change to Landsat-based remote sensing. Front. Ecol. Environ. 12, 339–346. https://doi.org/10.1890/130066

Kirwan, M.L., Guntenspergen, G.R., 2015. Response of plant productivity to experimental flooding in a stable and a submerging marsh. Ecosystems 18, 903–913. https://doi.org/10.1007/s10021-015-9870-0

Klemas, V., 2013a. Remote sensing of coastal wetland biomass: An overview. J. Coast. Res. 290, 1016–1028. https://doi.org/10.2112/JCOASTRES-D-12-00237.1

Klemas, V., 2013b. Airborne Remote Sensing of Coastal Features and Processes: An Overview. J. Coast. Res. 287, 239–255. https://doi.org/10.2112/JCOASTRES-D-12-00107.1

Klemas, V., 2011. Remote Sensing of Wetlands: Case Studies Comparing Practical Techniques. J. Coast. Res. 27, 418–427. https://doi.org/10.2112/JCOASTRES-D-10-00174.1

Klemas, V. V., 2015. Coastal and Environmental Remote Sensing from Unmanned Aerial Vehicles: An Overview. J. Coast. Res. 315, 1260–1267. https://doi.org/10.2112/JCOASTRES-D-15-00005.1

Manfreda, S., McCabe, M.F., Miller, P.E., Lucas, R., Madrigal, V.P., Mallinis, G., Dor, E. Ben, Helman, D., Estes, L., Ciraolo, G., Müllerová, J., Tauro, F., de Lima, M.I., de Lima, J.L.M.P., Maltese, A., Frances, F., Caylor, K., Kohv, M., Perks, M., Ruiz-Pérez, G., Su,

Z., Vico, G., Toth, B., 2018. On the use of unmanned aerial systems for environmental monitoring. Remote Sens. 10. https://doi.org/10.3390/rs10040641

Marcaccio, J. V., Markle, C.E., Chow-Fraser, P., 2015. Unmanned aerial vehicles produce high-resolution, seasonally-relevant imagery for classifying wetland vegetation. Int. Arch. Photogramm. Remote Sens. Spat. Inf. Sci. - ISPRS Arch. 40, 249–256. https://doi.org/10.5194/isprsarchives-XL-1-W4-249-2015

Mo, Y., Kearney, M.S., Riter, J.C.A., Zhao, F., Tilley, D.R., 2018. Assessing biomass of diverse coastal marsh ecosystems using statistical and machine learning models. Int. J. Appl. Earth Obs. Geoinf. 68, 189–201. https://doi.org/10.1016/j.jag.2017.12.003

Mo, Y., Momen, B., Kearney, M.S., 2015. Quantifying moderate resolution remote sensing phenology of Louisiana coastal marshes. Ecol. Modell. 312, 191–199. https://doi.org/10.1016/j.ecolmodel.2015.05.022

Morris, J.T., Sundareshwar, P. V., Nietch, C.T., Kjerfve, B.B., Cahoon, D.R., 2002. Responses of coastal wetlands to rising sea level. Ecology 83, 2869–2877. https://doi.org/10.2307/3072022

Mutanga, O., Adam, E., Cho, M.A., 2012. High density biomass estimation for wetland vegetation using worldview-2 imagery and random forest regression algorithm. Int. J. Appl. Earth Obs. Geoinf. 18, 399–406. https://doi.org/10.1016/j.jag.2012.03.012

Mutanga, O., Skidmore, A.K., 2004. Narrow band vegetation indices overcome the saturation problem in biomass estimation. Int. J. Remote Sens. 25, 3999–4014. https://doi.org/10.1080/01431160310001654923

Naimi, B., Skidmore, A.K., Groen, T.A., Hamm, N.A.S., 2011. Spatial autocorrelation in predictors reduces the impact of positional uncertainty in occurrence data on species distribution modelling. J. Biogeogr. 38, 1497–1509. https://doi.org/10.1111/j.1365-2699.2011.02523.x

Navarro, J.A., Algeet, N., Fernández-Landa, A., Esteban, J., Rodríguez-Noriega, P., Guillén-Climent, M.L., 2019. Integration of UAV, Sentinel-1, and Sentinel-2 data for mangrove plantation aboveground biomass monitoring in Senegal. Remote Sens. 11, 1–23. https://doi.org/10.3390/rs11010077

O'Donnell, J.P.R., Schalles, J.F., 2016. Examination of abiotic drivers and their influence on Spartina alterniflora biomass over a twenty-eight year period using Landsat 5 TM satellite imagery of the Central Georgia Coast. Remote Sens. 8, 477-. https://doi.org/10.3390/rs8060477

Otero, V., Van De Kerchove, R., Satyanarayana, B., Martínez-Espinosa, C., Fisol, M.A. Bin, Ibrahim, M.R. Bin, Sulong, I., Mohd-Lokman, H., Lucas, R., Dahdouh-Guebas, F., 2018. Managing mangrove forests from the sky: Forest inventory using field data and Unmanned Aerial Vehicle (UAV) imagery in the Matang Mangrove Forest Reserve, peninsular Malaysia. For. Ecol. Manage. 411, 35–45. https://doi.org/10.1016/j.foreco.2017.12.049

Ozesmi, S.L., Bauer, M.E., 2002. Satellite remote sensing of wetlands. Wetl. Ecol. Manag. 10, 381–402. https://doi.org/10.1023/A:1020908432489

Palmer, M.W., 2002. Scale detection using semivariograms and autocorrelograms, in: Learning Landscape Ecology. Springer, New York, NY, pp. 129–144.

Pasquarella, V.J., Holden, C.E., Kaufman, L., Woodcock, C.E., 2016. From imagery to ecology: leveraging time series of all available Landsat observations to map and monitor ecosystem state and dynamics. Remote Sens. Ecol. Conserv. 2, 152–170. https://doi.org/10.1002/rse2.24

Pennings, S.C., Grant, M.B., Bertness, M.D., 2005. Plant zonation in low-latitude salt marshes: Disentangling the roles of flooding, salinity and competition. J. Ecol. 93, 159–167. https://doi.org/10.1111/j.1365-2745.2004.00959.x

Pereira, E., Bencatel, R., Correia, J., Felix, L., Goncalves, G., Morgado, J., Sousa, J., 2009. Unmanned air vehicles for coastal and environmental research. J. Coast. Res. 56, 1557–1561. https://doi.org/http://www.jstor.org/stable/25738051

Pettorelli, N., Vik, J.O., Mysterud, A., Gaillard, J.M., Tucker, C.J., Stenseth, N.C., 2005. Using the satellite-derived NDVI to assess ecological responses to environmental change. Trends Ecol. Evol. 20, 503–510. https://doi.org/10.1016/j.tree.2005.05.011

Phinn, S., Franklin, J., Hope, A., Stow, D., Huenneke, L., 1996. Biomass distribution mapping using airborne digital video imagery and spatial statistics in a semi-arid environment. J. Environ. Manage. 47, 139–164. https://doi.org/10.1006/jema.1996.0042

Poley, L.G., Mcdermid, G.J., 2020. A Systematic Review of the Factors Influencing the Estimation of Vegetation Aboveground Biomass Using Unmanned Aerial Systems. https://doi.org/10.3390/rs12071052

Roy, D.P., Wulder, M.A., Loveland, T.R., C.E., W., Allen, R.G., Anderson, M.C., Helder, D., Irons, J.R., Johnson, D.M., Kennedy, R., Scambos, T.A., Schaaf, C.B., Schott, J.R., Sheng, Y., Vermote, E.F., Belward, A.S., Bindschadler, R., Cohen, W.B., Gao, F., Hipple, J.D., Hostert, P., Huntington, J., Justice, C.O., Kilic, A., Kovalskyy, V., Lee, Z.P., Lymburner, L., Masek, J.G., McCorkel, J., Shuai, Y., Trezza, R., Vogelmann, J., Wynne, R.H., Zhu, Z., 2014. Landsat-8: Science and product vision for terrestrial global change research. Remote Sens. Environ. 145, 154–172. https://doi.org/10.1016/j.rse.2014.02.001

SCWRP, 2018. Wetlands on the Edge: The Future of Southern California's Wetlands: Regional Strategy 2018 prepared by the Southern California Wetlands Recovery Project. California State Coastal Conservancy. Oakland, CA.

Silveira, E.M. de O., De Mello, J.M., Acerbi Júnior, F.W., Dos Reis, A.A., Withey, K.D., Ruiz, L.A., 2017. Characterizing Landscape Spatial Heterogeneity Using Semivariogram Parameters Derived from NDVI Images. Cerne 23, 413–422. https://doi.org/10.1590/01047760201723042370

Stein, E.D., Cayce, K., Salomon, M., Bram, D.L., Grossinger, R., Dark, S., 2014. Wetlands of the Southern California coast: Historical extent and change over time. South. Calif. Coast. Water Res. Proj. Tech. Rep. 826 1–50.

Stein, E.D., Doughty, C.L., Lowe, J., Cooper, M., Sloane, E.B., Bram, D.L., 2019. Establishing Targets for Regional Coastal Wetland Restoration Planning Using Historical Ecology and Future Scenario Analysis: The Past, Present, Future Approach. Estuaries and Coasts.

https://doi.org/https://doi.org/10.1007/s12237-019-00681-4

Tagle, X., Tagle Casapia, M.X., Tagle, X., Ximena, 2017. Study of radiometric variations in Unmanned Aerial Vehicle remote sensing imagery for vegetation mapping. Lund University. https://doi.org/10.13140/RG.2.2.16940.36485

Turner, I.L., Harley, M.D., Drummond, C.D., 2016. UAVs for coastal surveying. Coast. Eng. 114, 19–24. https://doi.org/10.1016/j.coastaleng.2016.03.011

Vousdoukas, M.I., Pennucci, G., Holman, R. a, Conley, D.C., Bartolomeo, V.S., 2011. A semi automatic technique for Rapid Environmental Assessment in the coastal zone using Small Unmanned Aerial Vehicles (SUAV). J. Coast. Res. 1755–1759. https://doi.org/https://www.jstor.org/stable/26482477

Wu, H., Li, Z.L., 2009. Scale issues in remote sensing: A review on analysis, processing and modeling. Sensors 9, 1768–1793. https://doi.org/10.3390/s90301768

Wulder, M.A., Masek, J.G., Cohen, W.B., Loveland, T.R., Woodcock, C.E., 2012. Opening the archive: How free data has enabled the science and monitoring promise of Landsat. Remote Sens. Environ. 122, 2–10. https://doi.org/10.1016/j.rse.2012.01.010

Xue, J., Su, B., 2017. Significant remote sensing vegetation indices: a review of developments and applications. J. sensors Vol.2017, 17p. https://doi.org/10.1155/2017/1353691

Zedler, J.B., 1982. The ecology of southern California coastal salt marshes: a community profile. U.S. Fish Wildl. Serv. Biol. Servces Program, Washington, D.C. FWS/OBS-81/54 110 p.

Zhang, M., Ustin, S.L., Rejmankova, E., Sanderson, E.W., 1997. Monitoring Pacific Coast Salt Marshes Using Remote Sensing. Ecol. Appl. 7, 1039–1053. https://doi.org/https://doi.org/10.1890/1051-0761(1997)007[1039:MPCSMU]2.0.CO;2

Zhou, Z., Yang, Y., Chen, B., 2018. Estimating Spartina alterniflora fractional vegetation cover and aboveground biomass in a coastal wetland using SPOT6 satellite and UAV data. Aquat. Bot. 144, 38–45. https://doi.org/10.1016/j.aquabot.2017.10.004

## 3.8 Supplemental Materials

**Table S3-1. Descriptions of remote sensing data and tidal levels during acquisition**

| | | | | Remote sensing data | | | Tidal level** (m NAVD88) | |
|---|---|---|---|---|---|---|---|---|
| Site | Archetype | UAV Flight Area ($km^2$) | Site Elevation* Mean ± S.D. and Range (m NAVD88) | Landsat Overpass Date | UAV Survey Dates | UAV Ortho Horizontal error (m) | UAV | Landsat |
| San Dieguito Lagoon | Large River Valley Estuary | 0.05 | 1.60 ± 0.29 (1.15 – 2.16) | 9/9/2018 | 9/4/2018 | 0.99 | 1.04 | 0.82 |
| Kendall-Frost Mission Bay Marsh Reserve | Intermediate estuary | 0.26 | 1.27 ± 0.53 (0.03 – 5.65) | 8/27/2019 | 8/28/2019 | 1.24 | 0.71 | 0.78 |
| Carpinteria Salt Marsh Reserve | Intermediate estuary | 0.17 | 1.85 ± 0.26 (0.61 – 3.37) | 9/26/2019 | 9/26/2019 | 1.10 | 0.70 | 0.70 |
| Los Peñasquitos Lagoon | Large River Valley Estuary | 0.14 | 1.88 ± 0.20 (0.99 – 2.44) | 9/12/2019 | 9/30/2019 | 0.96 | 1.25 | 0.75 |

*Elevation mean, standard deviation, and ranges of wetland areas and UAV survey areas (Figure 2; red outline) from NOAA-CA CC Coastal LiDAR project 2009–2013 DEM.

**Average tidal levels taken from the nearest NOAA tidal stations at the time of UAV flights and Landsat overpasses.

**Table S3-2. Linear models of aboveground biomass for all UAV vegetation indices per site (A – D) and for all sites combined (E). Vegetation indices selected based on band combinations possible for UAV or Landsat imagery.**

| **A. San Dieguito** | | | | | |
|---|---|---|---|---|---|
| **VI** | **Equation** | **$r^2$** | **RMSE (g $m^{-2}$)** | **AIC** | **p-value** |
| CIgreen | 576.9*CIgreen - 208.1 | 0.63 | 199.6 | 205.3 | < 0.005 |
| CIrededge | 3501*CIrededge - 547.9 | 0.81 | 145.3 | 195.8 | < 0.005 |
| CVI | 732.6*CVI - 1262 | 0.61 | 206.3 | 206.3 | < 0.005 |
| EVI2 | 2178.9*EVI2 + 84.4 | 0.39 | 256.7 | 212.9 | 0.012 |
| GNDVI | 3109.3*GNDVI - 649.7 | 0.64 | 199.0 | 205.2 | < 0.005 |
| NDRE | 9327.1*NDRE - 704.2 | 0.80 | 145.9 | 195.9 | < 0.005 |
| NDVI | 1838*NDVI - 63.4 | 0.48 | 220.5 | 210.4 | < 0.005 |
| **B. Kendall-Frost Mission Bay Marsh Reserve** | | | | | |
| **VI** | **Equation** | **$r^2$** | **RMSE (g $m^{-2}$)** | **AIC** | **p-value** |
| CIgreen | 920.3*CIgreen - 284.5 | 0.59 | 230.2 | 209.6 | < 0.005 |
| CIrededge | 1993.8*CIrededge + 457.5 | 0.15 | 329.3 | 220.3 | 0.15 |
| CVI | 603.7*CVI - 396.9 | 0.32 | 294.8 | 217 | 0.028 |
| EVI2 | 6137.1*EVI2 - 204.8 | 0.41 | 274.4 | 214.9 | 0.01 |
| GNDVI | 4389.8*GNDVI - 805.9 | 0.61 | 223.9 | 208.8 | < 0.005 |
| NDRE | 4557.6*NDRE + 442.8 | 0.15 | 330.2 | 220.4 | 0.16 |
| NDVI | 3153.2*NDVI - 496.2 | 0.48 | 241.1 | 213.1 | < 0.005 |
| **C. Carpinteria Salt Marsh Reserve** | | | | | |
| **VI** | **Equation** | **$r^2$** | **RMSE (g $m^{-2}$)** | **AIC** | **p-value** |
| CIgreen | 767*CIgreen + 8.3 | 0.44 | 415.4 | 272 | < 0.005 |
| CIrededge | 3400*CIrededge + 247.8 | 0.31 | 458.8 | 275.6 | 0.016 |
| CVI | 269.1*CVI + 396 | 0.07 | 533.2 | 281 | 0.28 |
| EVI2 | 5292*EVI2 + 107.4 | 0.49 | 394.6 | 270.2 | < 0.005 |
| GNDVI | 4798.3*GNDVI - 843.4 | 0.53 | 378.0 | 268.6 | < 0.005 |
| NDRE | 8862.9*NDRE + 125 | 0.33 | 453.2 | 275.2 | 0.013 |
| NDVI | 3567*NDVI - 255.9 | 0.68 | 293.8 | 261.7 | < 0.005 |
| **D. Los Peñasquitos** | | | | | |
| **VI** | **Equation** | **$r^2$** | **RMSE (g $m^{-2}$)** | **AIC** | **p-value** |
| CIgreen | 890.2*CIgreen + 227.5 | 0.66 | 537.7 | 281.3 | < 0.005 |
| CIrededge | 3193.9*CIrededge + 1015.9 | 0.58 | 593.0 | 284.8 | < 0.005 |
| CVI | 518.1*CVI + 132.1 | 0.37 | 732.6 | 292.4 | 0.008 |
| EVI2 | 6448.7*EVI2 + 521.9 | 0.65 | 540.5 | 281.5 | < 0.005 |
| GNDVI | 4702.1*GNDVI - 280.8 | 0.72 | 483.8 | 277.5 | < 0.005 |
| NDRE | 7362.7*NDRE + 1047.7 | 0.60 | 584.4 | 284.3 | < 0.005 |
| NDVI | 4351.9*NDVI + 63.9 | 0.79 | 398.0 | 272.6 | < 0.005 |
| **E. All Sites** | | | | | |
| **VI** | **Equation** | **$r^2$** | **RMSE (g $m^{-2}$)** | **AIC** | **p-value** |

| | | | | | |
|---|---|---|---|---|---|
| CIgreen | 897.8*CIgreen - 198.7 | 0.52 | 482.2 | 1008.8 | < 0.005 |
| CIrededge | 1988.2*CIrededge + 596.3 | 0.16 | 633.0 | 1044.8 | < 0.005 |
| CVI | 559.2*CVI - 346.5 | 0.34 | 564.2 | 1029.6 | < 0.005 |
| EVI2 | 3606.7*EVI2 + 376 | 0.20 | 618.0 | 1041.6 | < 0.005 |
| GNDVI | 4617.6*GNDVI - 766.1 | 0.49 | 495.4 | 1012.4 | < 0.005 |
| NDRE | 4534.3*NDRE + 603.4 | 0.16 | 636.6 | 1045.5 | < 0.005 |
| NDVI | 3368.4*NDVI - 210.2 | 0.40 | 534.6 | 1022.5 | < 0.005 |

Vegetation index descriptions: Chlorophyll Index Green Chlorophyll (CIgreen), Chlorophyll Index Rededge (CIrededge), Chlorophyll Vegetation Index (CVI), Enhanced Vegetation Index Green (EVI2), Green Normalized Difference Vegetation Index (GNDVI), Rededge Normalized Difference Vegetation Index (NDRE), and Normalized Difference Vegetation Index (NDVI).

**Table S3-3. Linear models of aboveground biomass for vegetation types and archetypes based on UAV imagery.**

**A. Vegetation Type**

| Dominant Cover Class | Equation | $r^2$ | RMSE (g $m^{-2}$) | AIC | p-value |
|---|---|---|---|---|---|
| Succulent | 1941.4*NDVI + 354.4 | 0.08 | 555.9 | 563.2 | 0.09 |
| Grass-Herb | 4760.4*NDVI - 700.1 | 0.36 | 516.7 | 343.3 | < 0.005 |
| All | 3368.4*NDVI - 210.2 | 0.40 | 534.6 | 1022.5 | < 0.005 |

**B. Wetland Type**

| Archetype | Equation | $r^2$ | RMSE (g $m^{-2}$) | AIC | p-value |
|---|---|---|---|---|---|
| Large River Valley Estuary | 3607.9*NDVI - 143.5 | 0.43 | 639.5 | 526.1 | < 0.005 |
| Intermediate Estuary | 3193.7*NDVI - 296.2 | 0.49 | 337.1 | 483.8 | < 0.005 |
| All | 3368.4*NDVI - 210.2 | 0.40 | 534.6 | 1022.5 | < 0.005 |

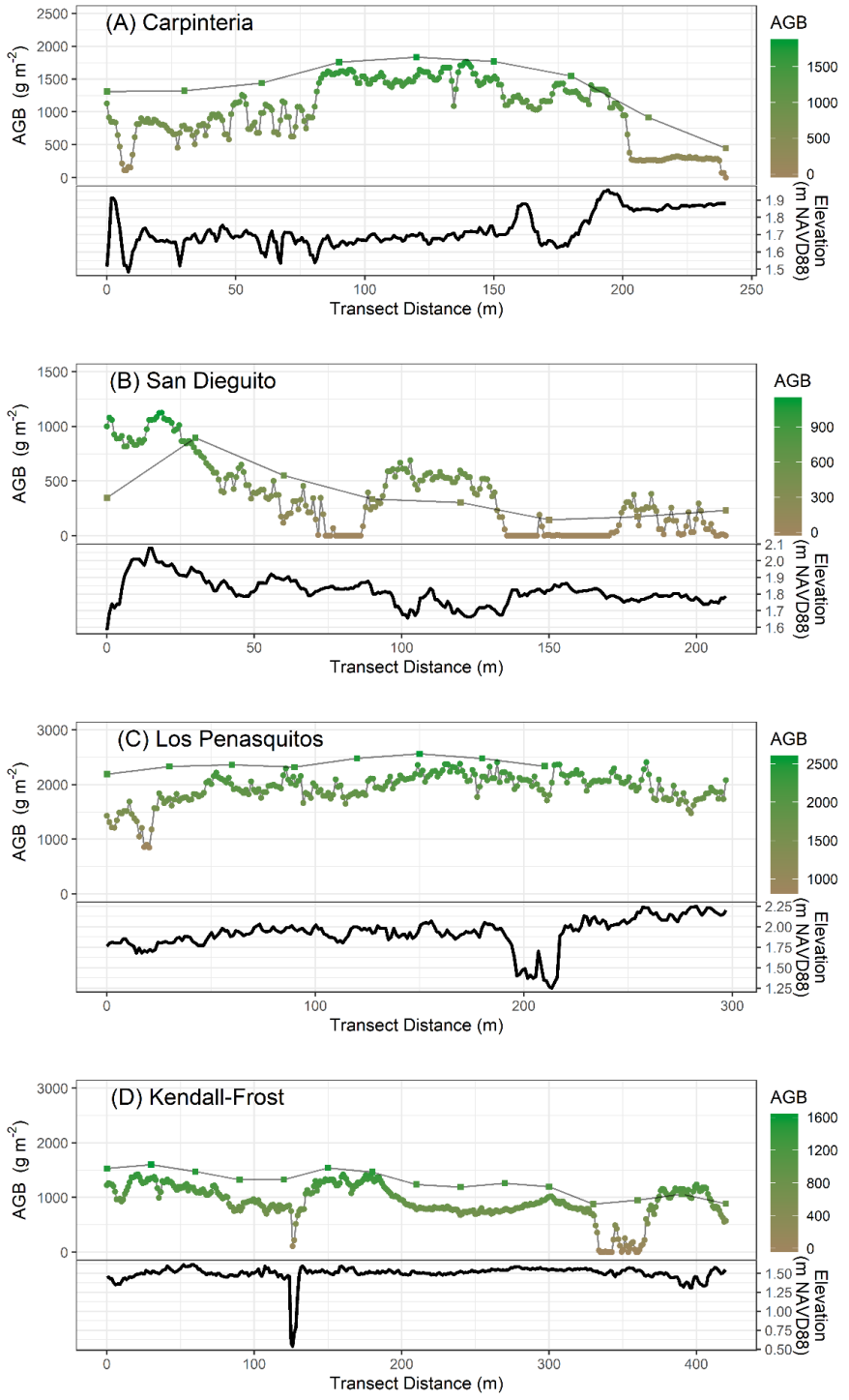


**Figure S3-1. Profiles of aboveground biomass estimated from UAV (circles) and Landsat (squares) imagery along elevational transects (black lines) for (A) Carpinteria Salt Marsh Reserve, (B) San Dieguito Lagoon, (C) Los Peñasquitos Lagoon, and (D) Kendall-Frost Mission Bay Marsh Reserve. Profiles of AGB and elevation were extracted from within the same area designated as the elevational transects used in field sampling design and semivariogram analysis for each site.**

# CHAPTER 4: High local variability in coastal wetland response to macroclimatic drivers in a region exhibiting long term greening trends

## 4.1 Abstract

The resilience of coastal wetlands will depend in part on the combined impacts of environmental drivers and human stressors. The impacts of macroclimatic drivers like sea level, precipitation, and temperature are expected to be highly spatially and temporally variable, as are human impacts and the complex responses of wetlands to environmental change. The relative influence of environmental drivers and human impacts across spatial and temporal scales therefore are important considerations in quantifying response and identifying major drivers to wetland conditions. Inferences from past wetland response to environmental change can be gained through publicly available, long-term historical observations. We use the Landsat satellite imagery archive to estimate past changes in wetland conditions using NDVI, a proxy of greenness, from 1984 – 2019 for 32 discrete wetland sites across the southern California region. We found that overall, a majority wetlands in the region exhibit significant, positive greening trends. However, our findings show that regional trends are complicated by local spatial and temporal variability in the relationship between wetland NDVI and macroclimatic drivers of temperature and precipitation. Improved understanding of long-term trends and intra-annual patterns in greening and browning, and the relative importance of environmental and human drivers across spatial scales, will be essential in managing these complex systems in a future with climate change and other anthropogenic stressors.

## 4.2 Introduction

Coastal wetlands are recognized as some of the world's most valuable ecosystems because of their ability to store carbon, protect coastlines, and provide many other ecosystem services to

humans (Barbier et al., 2011). The importance of coastal wetland ecosystems like salt marshes and mangrove forests is unsurprising given that human populations exist in higher densities along the world's coastlines (Neumann et al. 2015). Although these ecosystems are well-adapted to highly dynamic coastal environments, it is unclear how coastal wetlands may respond to changing environmental conditions and to ongoing human influence. Understanding the relative importance of environmental and human drivers to coastal wetland conditions, and how driver influence may vary over space and time, will be essential to adaptation efforts aimed at preserving these valuable ecosystems in the future (Erwin, 2009).

Coastal wetlands are sensitive to changes in macroclimatic drivers (Osland et al., 2016), with rising seas, increasing temperatures, and altered precipitation regimes causing a range of documented impacts to wetland ecosystems globally (Mckee et al., 2012; Newton et al., 2020; Wong et al., 2014). In addition to sea levels, temperature, rainfall, other important environmental drivers to coastal wetland plant communities include freshwater inflow, $CO^2$ concentration, storms, and extreme events (Langley et al., 2009; Mckee et al., 2012; Osland et al., 2016). Environmental factors relating to hydrological regimes, the availability of freshwater, and salinity can also influence wetland ecogeomorphology with consequences to wetland conditions (Day et al., 2008). In arid and semi-arid climates, wetland systems are especially susceptible to extreme drought conditions that lead to hypersalinity, which can influence plant species assemblages and health (Kelso et al., 2020; Wigginton et al., 2020). Periodic climate fluctuations, such as the El Niño Southern Oscillation (ENSO), also influence wetlands by directly altering sea temperatures, sea levels, and precipitation on intra-decadal scales (Goodman et al., 2018). Overall, impacts to coastal wetlands range greatly in scope from widespread habitat loss, degradation, or conversion,

to shifting community composition, and to changes in plant productivity and phenology (Short et al., 2016).

In addition to climatic and environmental drivers, human influence has significant impacts on the conditions of wetland ecosystems (Gedan et al., 2009; Newton et al., 2020). The urbanization of coastlines worldwide has led to wetland habitat loss and degradation, conversion to other land uses, increased development, and shoreline hardening (Gittman et al., 2015). Hardened infrastructure can increase the risk of coastal squeeze (Borchert et al., 2018), habitat loss (Gittman et al., 2015), and changes to wetland plant communities (Watson et al., 2017). Other impacts that accompany urbanization include resource extraction, species introductions and invasive species, hydrologic alteration, pollution and eutrophication, and restoration, conservation, and management (Gedan et al., 2009). Coastal management and restoration programs have arisen in recent decades to counteract negative human impacts on wetlands (Zedler and Callaway, 1999), however, even active management and restoration efforts can have direct consequences to plant communities, habitat distributions, and conditions within wetland and estuarine systems (Kennish, 2001).

Both environmental and human drivers important to coastal wetlands are naturally variable in space and time, which contributes to spatial and temporal variability in wetland conditions. Spatially, the response of wetlands to environmental change is likely to vary among individual wetland species, sites, or systems (Boesch et al., 2000; Janousek et al., 2016; Scavia et al., 2002). Similarly, human impacts are also highly contextual and variable in space (Gedan et al., 2009). Temporal variability is inherent to environmental and human drivers, and both can occur as short-term, episodic “pulse” events or gradual, long-term “press” disturbances depending on timing and

magnitude. The combined effects of spatially- and temporally-variable environmental and human drivers complicate our understanding of what drives conditions within wetland.

Changes in estuary conditions in response to environmental and human drivers can be monitored through publicly available, long-term datasets (Franklin et al., 2017). The Landsat satellite imagery archive offers global coverage and continuous, 16-day image collections dating back to 1984 with consistent, reliable data, which allows for investigation into long-term changes at broad scales (Kennedy et al., 2014; Pasquarella et al., 2016; Wulder et al., 2012). In coastal wetland application**s,** Landsat has been used in wetland ecosystems to monitor wetland habitat distributions and zonation (Bunting et al., 2018; Kearney et al., 2002; Rogers et al., 2017), identify disturbance events (Steyer et al., 2013), estimate biomass and carbon storage (Byrd et al., 2014, 2018; Klemas, 2013; Mo et al., 2018), and to identify patterns and drivers of wetland biomass, health, phenology, and overall greenness in both salt marsh and mangrove wetlands (Brooke et al., 2017; Buffington et al., 2018; Cavanaugh et al., 2018; Kearney et al., 2002; Mo et al., 2019, 2015; O'Donnell and Schalles, 2016; Wu et al., 2017).

Investigations into wetlands that use remote sensing often rely on vegetation indices to infer wetland properties. Vegetation indices summarize the spectral reflectance occurring in wetland plants (Mishra and Ghosh, 2015; Mutanga and Skidmore, 2004; Xue and Su, 2017), which can indicate characteristics ranging from biophysical plant properties to large-scale ecosystem change (Adam et al., 2010; Xue and Su, 2017). The normalized difference vegetation index (NDVI; Rouse et al., 1974) and the enhanced vegetation index (EVI; Jiang et al., 2008) are commonly used indices that convey "greenness" of vegetation. Satellite-based measures of NDVI over time can reveal trends in greening or browning that are indicative of biological (plant productivity and growth) and physical (cover composition) changes to vegetated ecosystems (e.g.,

Myers-Smith et al., 2020). Greening trends in coastal wetlands, therefore, likely refect in situ increases to plant productivity, aboveground biomass, or vegetated cover in a wetland, whereas browning trends may indicate habitat loss, conversion to mudflat or subtidal, or reductions in plant productivity or biomass. Using greenness as a proxy for estuaries conditions over time facilitates the testing of relative effects that human and environmental drivers have on coastal wetlands.

The wetlands of southern California offer an interesting opportunity to investigate the effects of environmental and human drivers to wetland conditions, i.e., greenness. The southern California region is home to a diverse network of coastal and estuarine wetlands that range in size, setting, ecology and wetland typology (SCWRP, 2018). Wetlands in the region are relatively small and discrete wetland remnants (Grossinger et al., 2011; Stein et al., 2019, 2014), compared to other regions containing large, heterogeneous wetlands such as the Sacramento–San Joaquin River Delta, California, USA, or the Mississippi River Delta, Louisiana, USA. In southern California, wetlands are structurally and functionally diverse due to coastal setting and exposure (Jacobs et al., 2011). A typology framework was developed to classify southern California's many diverse wetlands into groups that represent systems with similar physical structure, processes, and plant community composition (Stein, 2015), which are expected to function similarly and respond to physical drivers and external stressors in a similar manner (Stein et al., 2019). Wetland types used in this study, hereafter referred to as wetland "archetypes", include small creeks and lagoon, intermediate (i.e., opening and closing) estuaries, large lagoons, large river valley estuaries, and fragmented river valley estuaries (for detailed descriptions, see SCWRP, 2018).

Southern California's diverse wetlands are threatened by sea level rise (SCWRP, 2018; Thorne et al., 2018, 2016), but impacts are predicted to be highly variable among wetland sites (Doughty et al., 2018), and how they will respond to future changes in other environmental factors

are unclear. Furthermore, there is not a regional baseline for wetland conditions or how they have changed with recent environmental changes. The semi-arid, Mediterranean climate of this region is marked by wet winters and dry summers with highly variable precipitation (Dettinger et al., 2011), which has led to recent droughts in the absence of rainfall and high potential evaporation (MacDonald, 2007). Precipitation regimes in this region are also influenced by phases in the interannual El Nino-Southern Oscillation (ENSO) climate mode and the multidecadal Pacific Decadal Oscillation (PDO) mode (Dettinger et al., 2011). Site-based studies indicate that increased rainfall and flooding decrease soil salinity, which can cause increases in biomass and lead to changes in marsh species composition (Callaway and Sabraw, 1994; Zedler, 1983). Altered precipitation and streams flows also have resulted in plant stress (Zedler et al., 1986). Much work has been done in this region to manage and restore coastal wetlands (e.g., Zedler et al. 1996; SCWRP, 2018). Therefore, a holistic perspective of how wetlands across this region are impacted by interacting environmental and human drivers can aid future management efforts.

In this study, we use the Landsat archive to track changes in greenness, an indicator of the biological and physical conditions relating to vegetation within wetlands, for 32 wetlands in the southern California region from 1984 – 2019. Using Landsat to monitor southern California's wetlands, we aim to 1) quantify long-term trends of wetland greenness over 35 years and 2) characterize intra-annual patterns in greening for the region. Using unique wetland time series, our goals were to 3) identify the relative importance of drivers controlling greenness at wetlands across a region and 4) identify the spatial and temporal variability in the relationship between greenness and environmental or human factors. We predict that the dominant environmental controls to past changes in wetland NDVI will be related to water availability as this represents a major environmental constraint in Mediterranean climates. Furthermore, we test the hypothesis that

wetland archetypes should exhibit similar trends and intra-annual patterns in greenness caused by similar sensitivity to environmental drivers. This novel application in a region facing a combination of climate and human stressors can uncover potential spatial and temporal variability in future wetland response to environmental change.

## 4.3 Methods

### *4.3.1 Study Region and Wetland Site Description*

There are approximately 105 discrete wetlands that have been identified and mapped within the southern California region (Stein et al., 2019). These wetland areas were previously delineated for regional adaptation planning and management efforts based on 2016 National Wetland Inventory (NWI) data by the Southern California Coastal Water Research Project (SCCWRP). Delineated wetland areas in this region range greatly in size and function, from vernal pools occupying a few tenths of a hectare to large estuaries and lagoons over 250 hectares in size (Stein et al., 2019). The wetland archetype typology was developed to classify wetlands of similar setting, structure, and function, and to provide a framework to predict future response to SLR and aid ongoing regional restoration planning efforts (Doughty et al., 2018; Stein et al., 2019). We selected 32 wetland sites for this study based on wetland archetype, size, habitat composition, management and restoration history, and the availability of environmental data sources. Size was a limiting factor in using Landsat imagery to estimate wetland greenness (described below). Overall, selected wetlands represented a range of sizes and archetype classifications in the region to the best of our ability.

For the 32 representative sites, we used the SCCWRP wetland boundaries to define the areas for developing Landsat time series (described below). We used these boundaries as they have been relatively stable over 1984 – 2019 in many of the region's wetlands due to the confines

of adjacent, upland development, for which the wetland-urban bounds are unlikely to change in the future without active restoration. Therefore, these boundaries offer a constant area to investigate changes in greenness within each wetland that represent overall health and shifting habitat composition. Habitats mapped within wetland bounds include vegetated marsh, unvegetated mudflats and salt flats, and subtidal habitats.

#### 4.3.2 Landsat Time Series

Landsat time series were developed for 32 focal wetland sites using Google Earth Engine (EE; https://earthengine.google.com/). EE provides a cloud-based platform for storing and analyzing geospatial and remotely sensed data (Gorelick et al., 2017). Using EE, we accessed and preprocessed Landsat Tier 1 Surface Reflectance scene data from 1984 – 2019 collected with Landsat 5 TM, Landsat 7 ETM, and Landsat 8 OLI sensors. Landsat scenes refer to individual multispectral optical images taken every 16 days at a specific path/row locations, and containing pixels with 30 x 30-m ground spatial resolutions (Wulder et al., 2019). Landsat scenes were preprocessed to remove edge pixels and pixels containing clouds and water using the pixel quality assessment product ("Pixel_QA"; formerly "CFmask") that accompanies each Landsat scene (Zhu and Woodcock, 2012). Resulting images contain only pixels with clear land within each wetland boundary. We used this approach to remove continually subtidal areas from each Landsat scene per site, and to allow flexibility if habitat distributions (vegetated marsh, unvegetated mudflat, and subtidal habitats) change over time within wetland areas. Counts of clear land pixels for each scene were converted to area in order to identify potential changes in wetland areas (vegetated marsh, unvegetated mudflat) over 1984 – 2019 at each site.

From the Landsat pixels of clear land, we also calculated NDVI as a metric of wetland greenness and health. Our previous work in the region shows NDVI is positively correlated to

aboveground biomass (AGB) in simple vegetation canopies and AGB does not saturated with NDVI (Doughty and Cavanaugh, 2019; Doughty et al., *submitted*). Landsat NDVI time series were then corrected for differences among Landsat sensors to improve continuity in the 35-year NDVI time series (Vogelmann et al., 2016). Landsat 8 OLI data was corrected to align with Landsat 7 ETM+, as the ETM+ sensor has been shown to be consistent with Landsat 5 TM (Flood, 2014). Correction factors developed specifically for surface NDVI were applied to all Landsat 8 data (Roy et al., 2016).

We performed additional quality control (QC) measures to account for tides and errors in masking cloudy and water pixels in GEE. First, we compared local tide data from the nearest NOAA tide gauge (described below) to each Landsat scene and flagged scenes taken when tides were greater than the mean high water (MHW) designated by the same NOAA tide gauge. Similar time series analyses in coastal wetlands have filtered images for tide effects (Buffington et al., 2018; O'Donnell and Schalles, 2016), while others place no tidal restrictions (Brooke et al., 2017), or rely on the Landsat pixel quality ("Pixel_QA" or "CFmask") data to remove tidally-inundated pixels (Mo et al., 2019). We flagged Landsat scenes for manual inspection if average site NDVI was below 0.2 as these usually correspond to soil or water, and if scenes were detected as time series outliers. To detect outliers, we used the R package 'tsoutlier', which implements the Chen and Liu (1993) iterative weighted moving average filter to account for negatively-biased noise in NDVI time series (Hird and McDermid, 2009). Scenes that were flagged for high tides, low NDVI, low pixel counts, and as additive outliers were then visually inspected in EE and were removed from analysis when the impacts of clouds and tides were clear. Buffington et al. (2018) compared the effects of similar QC measures against unfiltered time series and found that subsequent analyses of marsh phenology were not significantly impacted by the manual removal of poor

quality scenes. We created an interactive EE application to allow users to inspect uncorrected NDVI time series for wetland sites in southern California (https://cheryldoughty.users.earthengine.app/view/socalwetlandtimeseriesviewerv3). Note that time series displayed in EE have not undergone the corrections and QC measures as the time series used in the following analyses.

Following manual removal of poor-quality scenes, cleaned time series containing all Landsat scenes per site were aggregated to monthly and annual time series of mean NDVI. Due to the small size of wetlands in the region, Landsat pixels within the predefined estuary boundaries may contain a mix of vegetated marsh, unvegetated mudflat, and subtidal habitats. Although precautions were taken to mask water pixels during imagery processing and QC (Figure S4-2), the Landsat-derived time series are reflective of "whole estuary" conditions and not solely vegetated marsh areas. Therefore, we refrain from inferring marsh productivity and biomass from NDVI time series and instead use NDVI as a proxy for overall estuary greenness.

### *4.3.3 Environmental and Climatic Datasets*

To investigate the drivers of wetland greenness over time, we acquired time series of environmental conditions from 1984 – 2019 falling into 6 categories: sea levels, stream discharge, precipitation, temperature, drought, and climate oscillations (Figure 4-1). Monthly time series of temperature, precipitation, and vapor pressure deficit (VPD) for each site were acquired from gridded (4-km) PRISM data (https://prism.oregonstate.edu; Daly et al., 2008). Using monthly PRISM temperature and precipitation data, we calculated the Self-Calibrating Palmer Drought Severity Index (PDSI) using the R package 'scPDSi' (Wells et al., 2004) and the monthly Standardized Precipitation Evapotranspiration Index (SPEI) and the Standardized Precipitation Index (SPI) using the R package 'SPEI' (Vicente-Serrano et al., 2010). To calculate PDSI, SPEI,

and SPI, estimates of potential evaporation were also estimated from precipitation data and site latitude using the Thornthwait (1948) equation to accounts for seasonal changes in sunlight hours.

NOAA sea level data were available for 5 stations in the region: Santa Barbara, San Diego, La Jolla, Los Angeles, Santa Monica (https://tidesandcurrents.noaa.gov). Daily sea level data for each site were taken from the nearest NOAA station (Figure S4-1).Data on daily stream discharge were taken from USGS Stream Gauges available for 11 of the 32 study sites (https://waterdata.usgs.gov). For sites without USGS Stream Gauges stream discharge data was not considered in regression analyses. More work is needed in order to incorporate modeled runoff, and associated nutrient inputs, for each of the wetland sites in the region. Furthermore, additional data on the frequency and duration of estuary mouth closures in this region would aid our understanding the impacts to intermediate, or opening and closing, estuaries.

We also considered climatic fluctuations using monthly data on the Oceanic Nino Index (ONI; NOAA Climate Prediction Center; https://www.cpc.ncep.noaa.gov), the Pacific Decadal Oscillation (PDO) index (NOAA National Centers for Environmental Information; https://www.ncdc.noaa.gov), and the multivariate ENSO index (MEI; NOAA physical Sciences Laboratory; https://psl.noaa.gov/enso/mei). Environmental data specific to each wetland site were aggregated to monthly and annual time series to be analyzed with the corresponding Landsat NDVI time series for each site. All environmental and climatic variables were summarized using the mean, except for precipitation and stream discharge, which were summed according to calendar year (January to December) and to water year (October to September). Water year summaries accounted for precipitation beginning in October of the preceding year and were compared to estimated wetland NDVI of the subsequent calendar year. We also summarized temperature and precipitation for the wet season (October - March) and dry season (April - September) for each

year. Overall, 24 explanatory variables were initially tested for correlations of NDVI and environmental drivers.

### *4.3.4 Human Impact Datasets*

To investigate human-related impacts to wetland NDVI in the region, we quantified urban development and restoration activities for each wetland. Urban development was quantified as the percent developed areas in 2016 using the Landsat-derived National Land Cover Database (NLCD; Yang et al., 2018). Unfortunately, these data are not available as a dynamic time series, as 2001 is the only comparable NLCD baseline. Developed areas included NLCD classes "Developed, open space", "Developed, low intensity", "Developed, med intensity", and "Developed, high intensity", which represent residential and commercial development with impervious surfaces ranging from 20 – 100%. We summarized developed areas contained in the watersheds associated with each wetland. Watersheds for each site were acquired from the USGS StreamStats Application (https://streamstats.usgs.gov/ss/). The 2016 NLCD was accessed and analyzed using EE.

We used publicly available records from the California State Coastal Conservancy (CA CC) to estimate the number of restoration projects that have occurred at each wetland (http://www.mapcollaborator.org/sccpv/prod/). We acquired the names and dates for projects that described impacts to wetland areas. Dates reported in this dataset reflect the date that projects were authorized by the CA CC, not the exact dates and duration that projects were implemented at sites. Therefore, this data was excluded from any temporal analyses. Rather, we used the total number of restoration projects and the percent change in developed areas as metrics of human impacts to compare against long-term trends in NDVI. More work is needed to build in-depth timelines of the duration, intensity, and ownership of restoration efforts within the wetlands in the region.

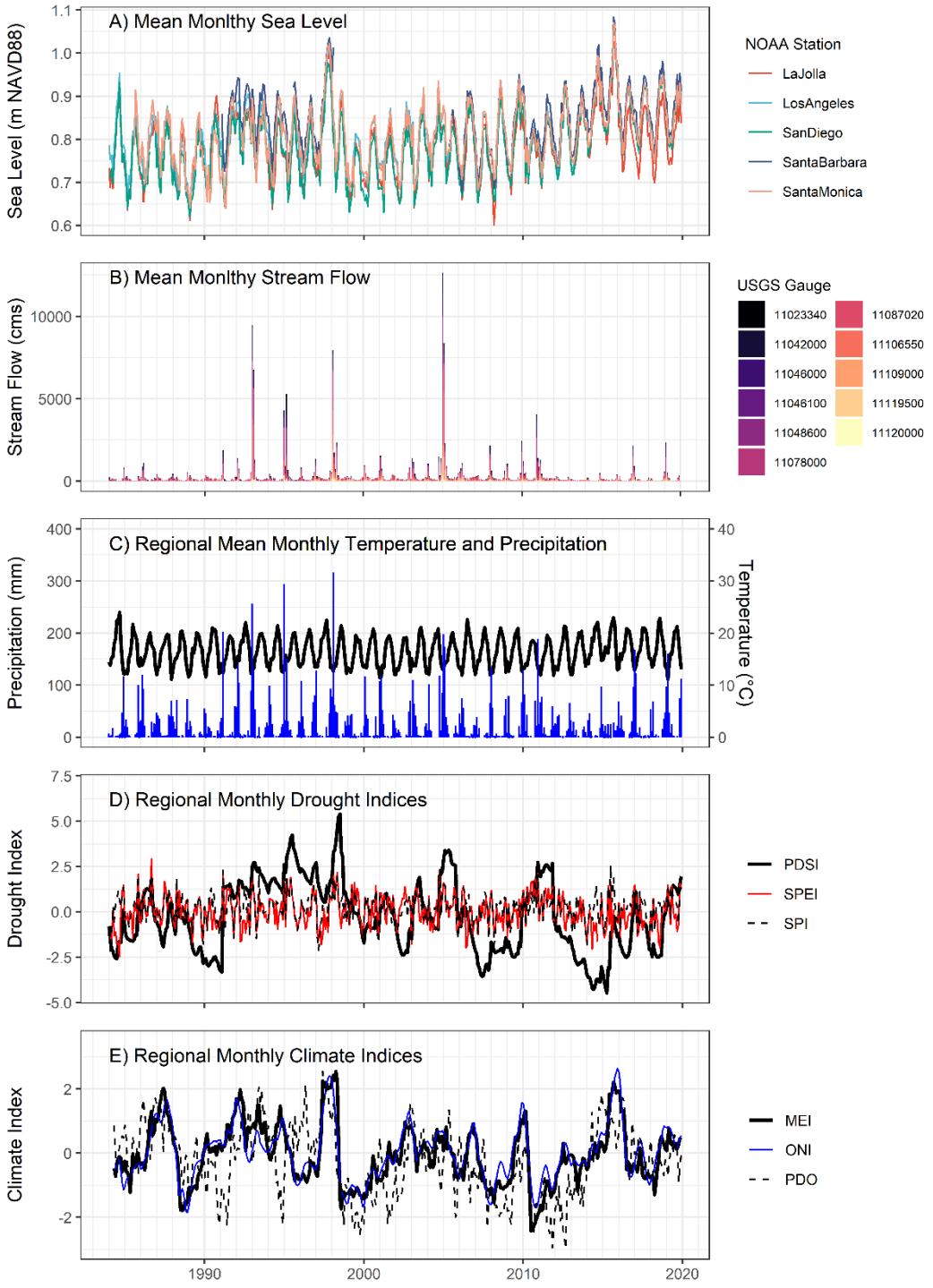


**Figure 4-1. Monthly time series (1984 – 2019) of A) mean sea level for 5 regional NOAA Stations, B) mean stream discharge for 11 regional USGS gauges C) regional means of temperature (black) and precipitation (blue), D) regional means of drought indices, and E) regional means of climate indices. Note dual axes for temperature and precipitation data (C).**

### *4.3.5 Time Series Analysis*

#### *4.3.5.1 Long-term Trends*

We estimated trends in NDVI for individual wetlands over the study period (1984 – 2019) using Sen's slope. Sen's slope estimates trend as the median slope from a set of local regressions fit to portions of the time series and is more suitable for investigating trends in nonparametric data (Sen, 1968). Sen's slope was calculated using the R package 'trend' (Pohlert, 2020). We compared NDVI trends to site characteristics including latitude, size, archetype classification, habitat composition, urban development, and restoration activities in order to test non-environmental factors that may explain long-term changes in NDVI.

#### *4.3.5.2 Intra-annual Patterns*

We used monthly NDVI time series to characterize seasonal patterns in wetland greening and browning in southern California. We performed an unsupervised clustering technique on time series of mean monthly NDVI (1984 – 2019) from each site to identify wetland sites that exhibit similar intra-annual trends. We used k-means clustering to partition the observations (i.e., sites) into k clusters with the goal of minimizing the sum of squares between each observation and the assigned cluster centers (Hartigan and Wong, 1979). Distances among observations were calculated using dynamic time warping (DTW), which accounts for local compression and stretch in the time dimension when comparing time series (Giorgino, 2009). We tested the number of clusters (k) ranging from 2 – 7 and selected a k of 5 that minimized total within-cluster sum of square. Resulting clusters were compared to site wetland archetype classifications. To inspect intra-annual patterns for each site, mean monthly NDVI was summarized for all years and fit with a smoothing linear regression model for visualization.

**Table 4-1. Regional summary of environmental conditions over the 1984 – 2019 study period.**

| Environmental Category | Environmental Variable (unit) | 1986 5-yr Average (mean ± SD) | 2016 5-yr Average (mean ± SD) | Trend (unit $yr^{-1}$) |
|---|---|---|---|---|
| Sea Level | Sea Level (m NAVD88) | 0.76 ± 0.07 | 0.87 ± 0.07 | 0.002*** |
| Stream Discharge | Stream Discharge (cms) | 23.86 ± 52.79 | 17.86 ± 64.45 | -97.41 |
| Precipitation | Precipitation (mm) | 19.1 ± 27.58 | 23.6 ± 36.53 | 158.4 |
| Temperature | Minimum Temperature (°C) | 11.88 ± 3.69 | 13.31 ± 3.55 | 0.025* |
| | Mean Temperature (°C) | 16.47 ± 2.94 | 17.38 ± 2.95 | 0.009 |
| | Maximum Temperature (°C) | 21.05 ± 2.41 | 21.44 ± 2.62 | -0.003 |
| | Dew Point Temperature (°C) | 9.12 ± 4.11 | 10.05 ± 4.18 | 0.012 |
| Drought | Min. Vapor Pressure Deficit (kPa) | 2.16 ± 0.48 | 2.28 ± 0.71 | 0.001 |
| | Max. Vapor Pressure Deficit (kPa) | 12.18 ± 2.75 | 12.41 ± 3.41 | -0.001 |
| | Palmer Drought Severity (PDSI) | -0.87 ± 1.1 | -1.57 ± 1.76 | -0.040 |
| | Standardized Precipitation Index (SPI) | 0.15 ± 0.8 | 0.24 ± 0.83 | 0.000 |
| | Standardised Precipitation-Evapotranspiration Index (SPEI) | -0.04 ± 0.98 | -0.3 ± 0.93 | -0.009 |
| Climate | Oceanic Niño Index (ONI) | -0.15 ± 0.91 | 0.4 ± 0.86 | 0.002 |
| | Pacific Decadal Oscillation (PDO) | 0.32 ± 0.79 | 0.28 ± 0.74 | -0.028 |
| | Multivariate ENSO Index (MEI) | -0.12 ± 0.96 | 0.23 ± 0.84 | -0.013 |

Asterisks indicate significance level of trend: * $p < 0.05$, ** $p < 0.005$, *** $p < 0.0001$

#### *4.3.5.3 Environmental Correlations with Annual NDVI*

We compared annual NDVI time series of 32 focal wetlands to time series of 24 environmental variables corresponding to each site using correlation techniques for nonparametric and nonstationary time series. Mean NDVI and environmental datasets did not all meet normality assumptions and trends in some datasets indicate nonstationary over the 1984 – 2019 period of study (Figure 4-2; Table 4-1). Environmental datasets were significantly correlated (Table 4-2). We tested for spatial autocorrelation using the multivariate, nonparametric covariance function in the R package 'sncf' (Bjørnstad and Falck, 2001), which showed that NDVI and environmental datasets were spatially autocorrelated in the region. NDVI time series were also temporally

autocorrelated. With these data considerations, we opted for regression and spatiotemporal statistical approaches suitable for nonparametric time series.

We investigated environmental controls on annual NDVI in the region using a two-step approach. First, we tested correlations among NDVI and all (24) environmental variables for individual wetland sites using Spearman's ranked correlation. These site-based correlations were used to identify the top environmental variables and potentially redundant variables within driver categories of sea level, temperature, precipitation, stream discharge, drought, and climate. Inferences from this first correlation analysis were used to highlight spatial variability in driver importance and to guide independent variable selection for more robust spatiotemporal regression techniques at the regional scale.

To estimate a global model that relates NDVI to environmental variables in the region, we implemented the spatiotemporal statistical analysis termed Geographically and Temporally Weighted Regression (GTWR; Fotheringham et al., 2015). Geographically Weighted Regression (GWR) offers a spatial statistical method for modeling heterogeneous processes and considers how the correlation of responses and covariates may vary across geographic space (Brunsdon et al., 1996). Geographically weighted models are suitable when spatial data are not well described by a single global model (i.e., at the So Cal regional scale), and localized models calibrated to spatial regions (i.e., wetland sites) may improve description (Gollini et al., 2015). Geographically and Temporally Weighted Regression (GTWR) modelling techniques go further to account for both spatial and temporal heterogeneity, which are more applicable to datasets with spatial and temporal heterogeneity and nonstationary (Gollini et al., 2015).

**Table 4-2. Spearman's ranked correlation coefficients among environmental data. Bold numbers indicate significance levels of $p < 0.05$.**

| | Sea Level | Stream Discharge | Stream Discharge (Wtr Yr) | Precip | Precip (Wtr Yr) | Precip (Dry Seas.) | Precip (Wet Seas.) | Temp Min | Temp Mean | Temp Max | Dew Point | Temp Mean (Dry Seas.) | Temp Mean (Wet Seas.) | Temp Max (Dry Seas.) | Temp Max (Wet Seas.) | VPD Min | VPD Max | PDSI | SPI | SPEI | ONI | PDO |
|---|---|---|---|---|---|---|---|---|---|---|---|---|---|---|---|---|---|---|---|---|---|---|
| Stream Discharge | 0.0 | | | | | | | | | | | | | | | | | | | | | |
| Stream Discharge (Wtr Yr) | 0.0 | **1.0** | | | | | | | | | | | | | | | | | | | | |
| Precip | **0.4** | **0.3** | **0.3** | | | | | | | | | | | | | | | | | | | |
| Precip (Water Yr) | **0.3** | **0.3** | **0.4** | **0.9** | | | | | | | | | | | | | | | | | | |
| Precip (Dry Seas.) | **0.1** | 0.1 | **0.1** | **0.3** | **0.4** | | | | | | | | | | | | | | | | | |
| Precip (Wet Seas.) | **0.2** | **0.3** | **0.2** | **0.8** | **0.6** | **0.1** | | | | | | | | | | | | | | | | |
| Temp Min | **0.1** | 0.0 | 0.0 | **-0.4** | **-0.3** | 0.0 | **-0.3** | | | | | | | | | | | | | | | |
| Temp Mean | **0.2** | -0.1 | **-0.1** | **-0.4** | **-0.4** | **-0.1** | **-0.3** | **0.9** | | | | | | | | | | | | | | |
| Temp Max | **0.2** | **-0.2** | **-0.3** | **-0.4** | **-0.4** | **-0.1** | **-0.4** | **0.7** | **0.9** | | | | | | | | | | | | | |
| Dew Point | **-0.1** | **0.2** | **0.2** | **-0.3** | **-0.3** | 0.0 | **-0.2** | **0.7** | **0.6** | **0.5** | | | | | | | | | | | | |
| Temp Mean (Dry Seas.) | **0.2** | -0.1 | -0.1 | **-0.2** | **-0.2** | **-0.2** | **-0.3** | **0.7** | **0.8** | **0.8** | **0.4** | | | | | | | | | | | |
| Temp Mean (Wet Seas.) | **0.3** | -0.1 | -0.1 | **-0.2** | **-0.2** | 0.1 | **-0.3** | **0.7** | **0.8** | **0.7** | **0.4** | **0.5** | | | | | | | | | | |
| Temp Max (Dry Seas.) | **0.2** | **-0.2** | **-0.2** | **-0.2** | **-0.3** | **-0.2** | **-0.2** | **0.5** | **0.7** | **0.9** | **0.3** | **0.9** | **0.4** | | | | | | | | | |
| Temp Max (Wet Seas) | **0.2** | **-0.3** | **-0.3** | **-0.3** | **-0.3** | 0.0 | **-0.5** | **0.5** | **0.7** | **0.8** | **0.3** | **0.5** | **0.8** | **0.5** | | | | | | | | |
| VPD Min | **0.2** | **-0.3** | **-0.3** | **-0.3** | **-0.3** | **-0.1** | **-0.2** | **0.6** | **0.6** | **0.4** | 0.0 | **0.4** | **0.5** | **0.4** | **0.4** | | | | | | | |
| VPD Max | **0.3** | **-0.3** | **-0.3** | **-0.2** | **-0.2** | **-0.1** | **-0.3** | **0.2** | **0.5** | **0.7** | **-0.2** | **0.6** | **0.5** | **0.7** | **0.6** | **0.5** | | | | | | |
| PDSI | 0.0 | **0.4** | **0.4** | **0.4** | **0.4** | **0.2** | **0.5** | **-0.1** | **-0.2** | **-0.2** | **0.1** | **-0.3** | **-0.1** | **-0.3** | **-0.2** | **-0.2** | **-0.4** | | | | | |
| SPI | **0.2** | **0.4** | **0.4** | **0.4** | **0.4** | **0.6** | **0.5** | **0.1** | 0.0 | **-0.1** | **0.2** | **-0.1** | 0.0 | **-0.1** | **-0.2** | **-0.1** | **-0.2** | **0.5** | | | | |
| SPEI | **-0.3** | **0.3** | **0.3** | **0.3** | **0.3** | **0.3** | **0.4** | **-0.3** | **-0.4** | **-0.5** | 0.0 | **-0.5** | **-0.3** | **-0.5** | **-0.4** | **-0.4** | **-0.5** | **0.5** | **0.6** | | | |
| ONI | **0.4** | 0.0 | 0.0 | **0.1** | **0.1** | 0.0 | 0.1 | **0.1** | **0.1** | **0.1** | **0.1** | **0.1** | **0.1** | **0.1** | **0.1** | **0.1** | 0.0 | **0.1** | **0.1** | **-0.1** | | |
| PDO | **0.3** | 0.0 | -0.1 | 0.0 | **-0.1** | **0.1** | **0.2** | **0.3** | **0.3** | **0.4** | **0.3** | **0.2** | **0.3** | **0.2** | **0.3** | **0.2** | **0.2** | **0.2** | **0.2** | **-0.2** | **0.5** | |
| MEI | **0.4** | 0.0 | 0.0 | 0.0 | 0.1 | 0.1 | 0.1 | **0.1** | **0.1** | **0.1** | **0.1** | **0.1** | **0.1** | **0.1** | **0.2** | **0.1** | 0.0 | **0.2** | **0.1** | **-0.1** | **0.9** | **0.6** |

We applied GTWR to test the correlation of annual NDVI time series to environmental drivers for each site used the R package 'GWmodel' (Gollini et al., 2015). The weights matrix used in GTWR analyses incorporate both temporal and spatial information on distance using a spatiotemporal kernel function and a bandwidth parameter of the kernel function (Crespo, 2007; Fotheringham et al., 2015; Gollini et al., 2015). We opted for a gaussian kernel function that weighs observations closer in space and time more heavily, and continuously decreases assigned weights as observations grow farther in space and time. The kernel bandwidth controls the spatiotemporal distance over which the kernel function is applied. An adaptive kernel bandwidth ensures sufficient local information is used in determining the appropriate number of observations nearest in space and time to a given observation in an irregularly configured dataset. We selected optimal adaptive bandwidths that minimized model Akaike information criterion (AIC).

We limited our GTWR analysis to include only complete, regularly-intervaled environmental time series from this analysis. Fourteen environmental variables remained that include the top environmental drivers identified in the site-based correlations above (Table 4-3). We opted to remove incomplete datasets rather than introduce uncertainty by gap-filling missing data and because environmental variables within each driver category were strongly correlated with one another (Table 4-2). To further reduce redundancies in independent variable selection for GTWR models, we used principal components analysis (PCA) to reduce collinearity in environmental variables. PCA was performed on a standardized datasets of environmental variables and showed that the variables with highest absolute loadings accounting for 68% of total variance in the first 3 components. Top loading variables were max temperature ($Temp_{max}$), mean temperature ($Temp_{mean}$), and precipitation (PPT) for component 1, Oceanic Nino Index (ONI), multivariate ENSO index (MEI) and sea levels for component 2, and Standardized Precipitation

Index (SPI), dew point temperature ($Temp_{DewPt}$), and Oceanic Nino Index (ONI) for component 3. Ultimately, we tested seven models using the focal environmental variables from each environmental category based on Spearman's correlation, PCA, and stepwise AIC model rankings (Figure S4-3). We use GTWR to examine the spatial-temporal heterogeneity of the effect of these environmental drivers on wetland NDVI across a region.

**Table 4-3. Geographically weighted local summary statistics for environmental variables used in Geographically and Temporally Weighted Regression (GTWR)**

| Environmental Variable | Local Mean | Local Standard Deviation | Local Skewness | Local Variance | Localized coefficient of variation |
|---|---|---|---|---|---|
| Sea Level | 0.79 | 0.04 | 0.63 | 0.00 | 0.05 |
| Precip | 176.27 | 120.25 | 0.81 | 14459.79 | 0.68 |
| Precip (Water Yr) | 171.42 | 132.19 | 1.09 | 17474.94 | 0.77 |
| Temp Min | 12.87 | 1.37 | 0.25 | 1.88 | 0.11 |
| Temp Mean | 17.00 | 1.14 | 0.45 | 1.30 | 0.07 |
| Temp Max | 21.12 | 1.14 | 0.30 | 1.31 | 0.05 |
| Dew Point | 10.24 | 1.29 | 0.56 | 1.66 | 0.13 |
| VPD Min | 2.12 | 0.60 | 0.12 | 0.36 | 0.28 |
| VPD Max | 11.57 | 1.83 | 0.11 | 3.34 | 0.16 |
| PDSI | -0.34 | 2.02 | 0.33 | 4.06 | -5.68 |
| SPI | 0.19 | 0.33 | 0.02 | 0.11 | 1.79 |
| SPEI | 0.00 | 0.62 | 0.29 | 0.38 | NA |
| ONI | -0.22 | 0.91 | -0.07 | 0.83 | -4.10 |
| PDO | -0.07 | 0.72 | 0.31 | 0.52 | -10.47 |

## 4.4 Results

### 4.4.1 Long-term Greening Trends and Changing Environmental Conditions

Long-term NDVI trends from 1984 – 2019 ranged from -0.00062 – 0.0026 NDVI year$^{-1}$ for individual wetlands in the region (Figure 4-2, Figure 4-3). The majority of wetlands (24 out of 32) exhibited significant positive trends in NDVI, while two wetlands exhibited significant negative trends and six wetlands had nonsignificant trends in NDVI. Trends were not significantly correlated with site characteristics like latitude, size, archetype, habitat composition, watershed development, or restoration activities (Figure 4-4). However, there are differences in the variability of trends within archetypes, suggesting that some wetland types, such as intermediate estuaries, can exhibit a range of responses to similar drivers.

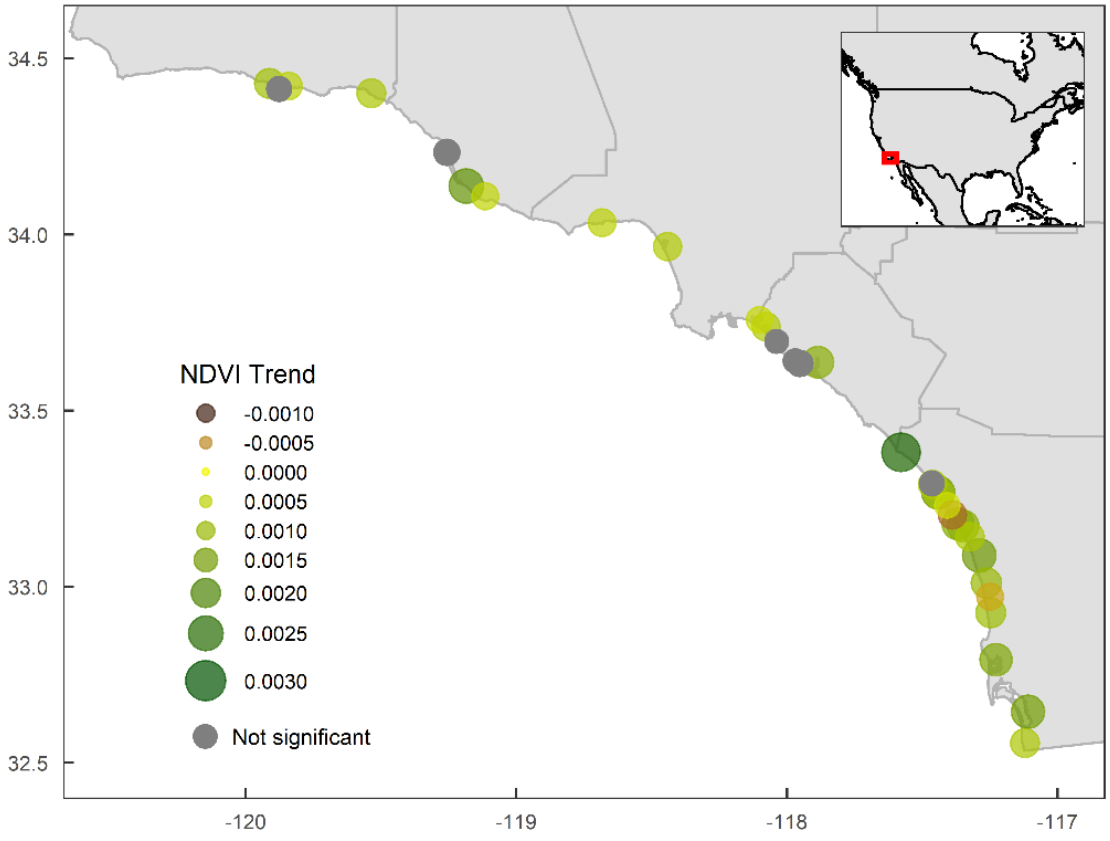


**Figure 4-2. Long-term trends in NDVI of wetland sites in southern California. Trend direction (color) and magnitude (size) are indicated for significant trends. Nonsignificant trends are shown in gray.**

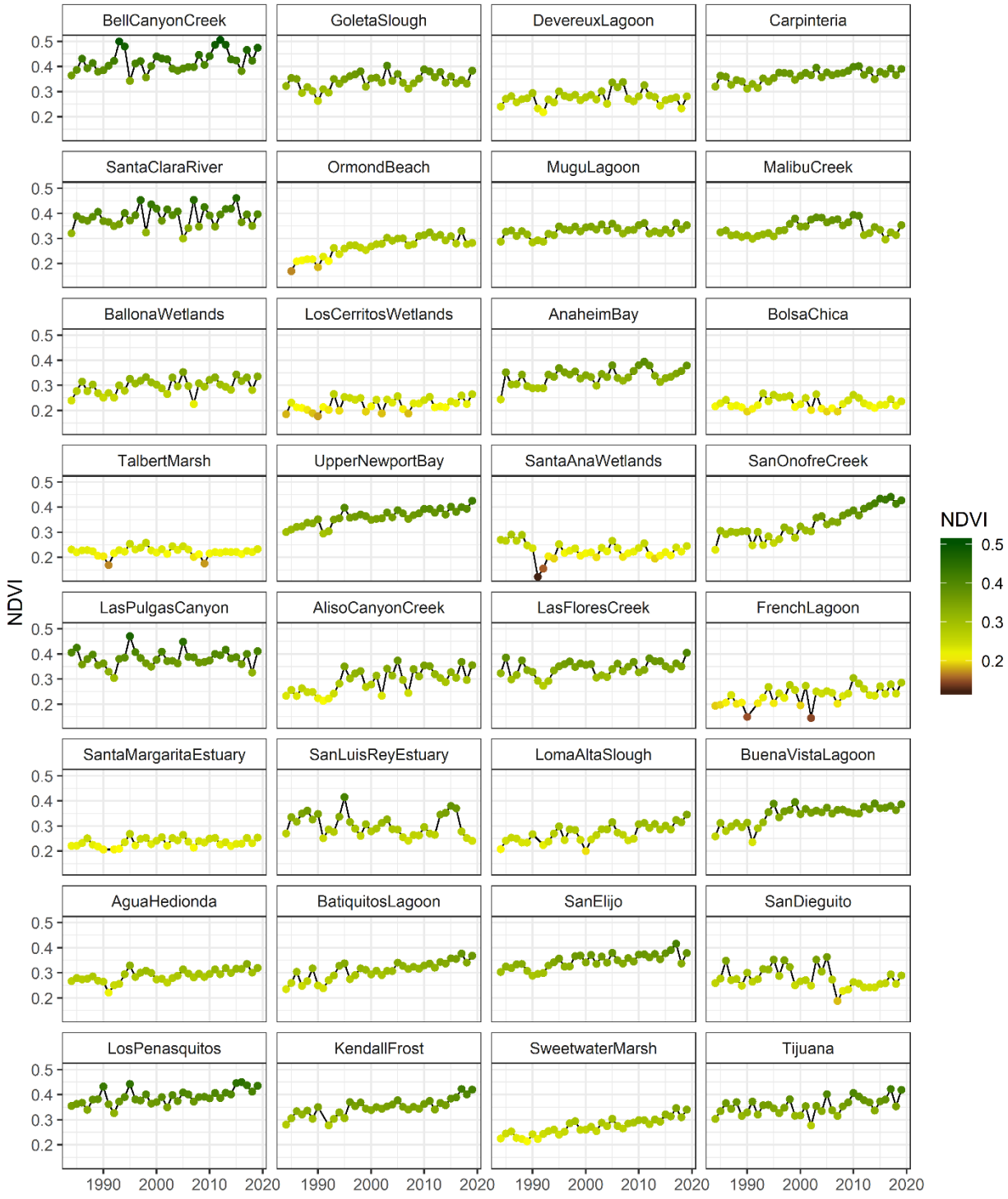


**Figure 4-3. Time series of annual NDVI for focal wetland sites in southern California. Sites are ordered latitudinally from North to South.**

Over the period of study, significant changes also occurred in environmental conditions in the region. Sea level and minimum annual temperature exhibited significant positive trends (Table 4-1). Sea levels in the region increased at a rate of 2.0 mm $yr^{-1}$ ($p < 0.0001$) and minimum temperatures increased at a rate of 0.025 °C $yr^{-1}$ ($p < 0.05$). No other significant trends in other environmental drivers were found.

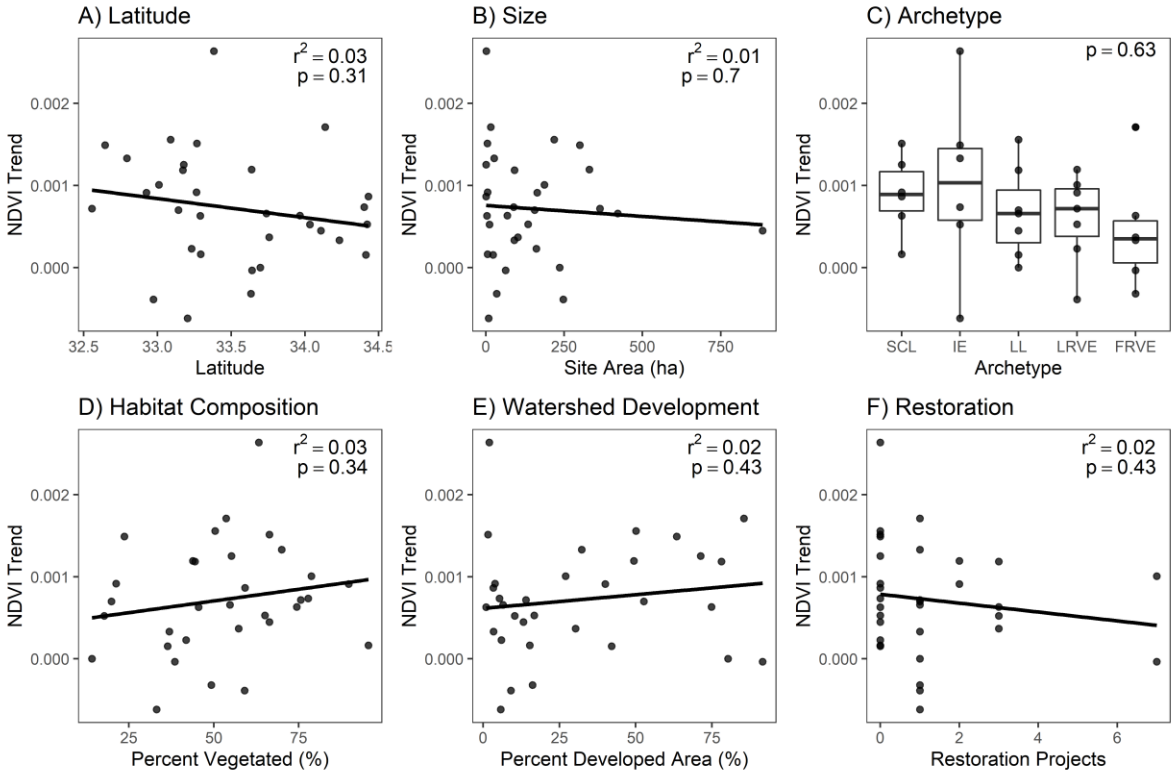


**Figure 4-4. Trends related to site characteristics of A) latitude, B) size, C) archetype classification, D) habitat, E) percent area of watershed development, and F) number of restoration projects. Archetypes include Small Creeks and Lagoons (SCL), Intermediate Estuaries (IE), Large Lagoons (LL), Large River Valley Estuaries (LRVE), and Fragmented River Valley Estuaries (FRVE).**

### 4.4.2 Variability in Intra-Annual NDVI Patterns Among Wetland Types

Intra-annual patterns in NDVI were characterized from monthly NDVI time series per wetland site and grouped according to archetype (Figure 4-5). Five clusters emerged from the k-means clustering that reflect differences in the overall magnitude of intra-annual NDVI and the shape of seasonal greening and browning patterns. Intra-annual patterns varied greatly among sites

within each archetype, indicating that there are not typical or singular seasonal patterns in NDVI that describe each archetype. However, the majority of large river valley sites were grouped according to intra-annual trends, suggested less variability within this archetype compared to others. The cluster analysis does indicate five general intra-annual patterns for wetlands in the region (Figure 4-5): high NDVI overall with peak NDVI occurring from April to September (green); intermediate NDVI with peaks in late summer, early fall (orange); intermediate NDVI with peaks in spring (light orange); low NDVI with variability in spring (blue); and low NDVI with little intra-annual variability (red).

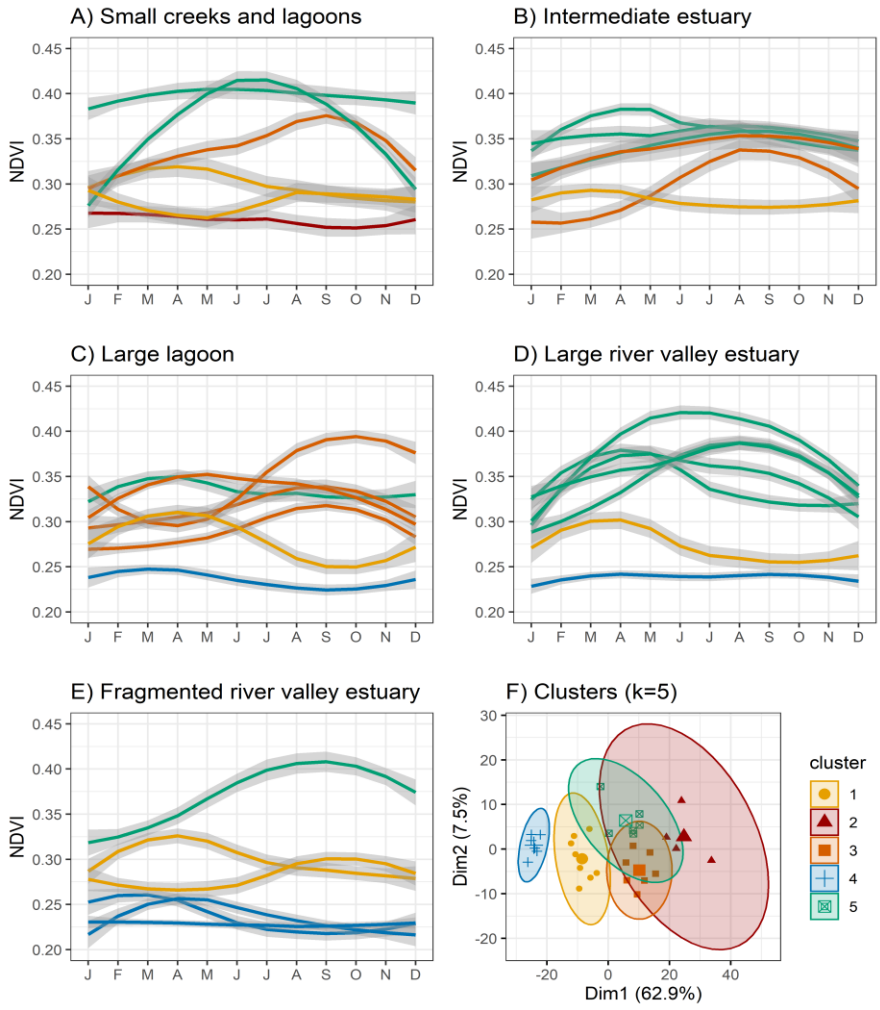


**Figure 4-5. Intra-annual NDVI patterns according to wetland archetypes and assigned k-means clusters.**

### 4.4.3 Site-Based Correlations Show Spatial Variability in Key Drivers of Wetland NDVI

Univariate regressions among NDVI and each environmental variable performed on individual sites show variability in the importance of factors controlling NDVI across the region (Figure 4-6). Sea levels were significantly positively correlated with NDVI in southern sites. For sites with available USGS stream discharge data, six show positive significant correlations with NDVI and 2 sites showed negative significant trends. Annual estimates of stream discharge summarized for calendar year and water year were similarly correlated with NDVI. Precipitation variables were overwhelmingly positively correlated with NDVI, with annual summaries of precipitation for the calendar year and water year showing more significant correlations than precipitation estimates for the dry and wet seasons. Two sites, the Santa Clara River Estuary and the San Luis Rey Estuary, showed significant negative correlations with both precipitation and stream discharge. Overall, precipitation variables exhibited the highest correlations with NDVI in the region.

Temperature variables did not show a clear relationship with NDVI for wetlands across the region (Figure 4-6). Five sites in the south indicated a significant positive relationship with temperature, while 2 sites to the north showed significant negative relationships. Correlations with drought indices were variable but indicate overall positive correlations for PDSI, SPEI and SPI and negative correlations with estimates of vapor pressure deficit (VPD) across the region. Significant correlations among climate indices MEI and PDO and NDVI were only apparent for 5 sites.

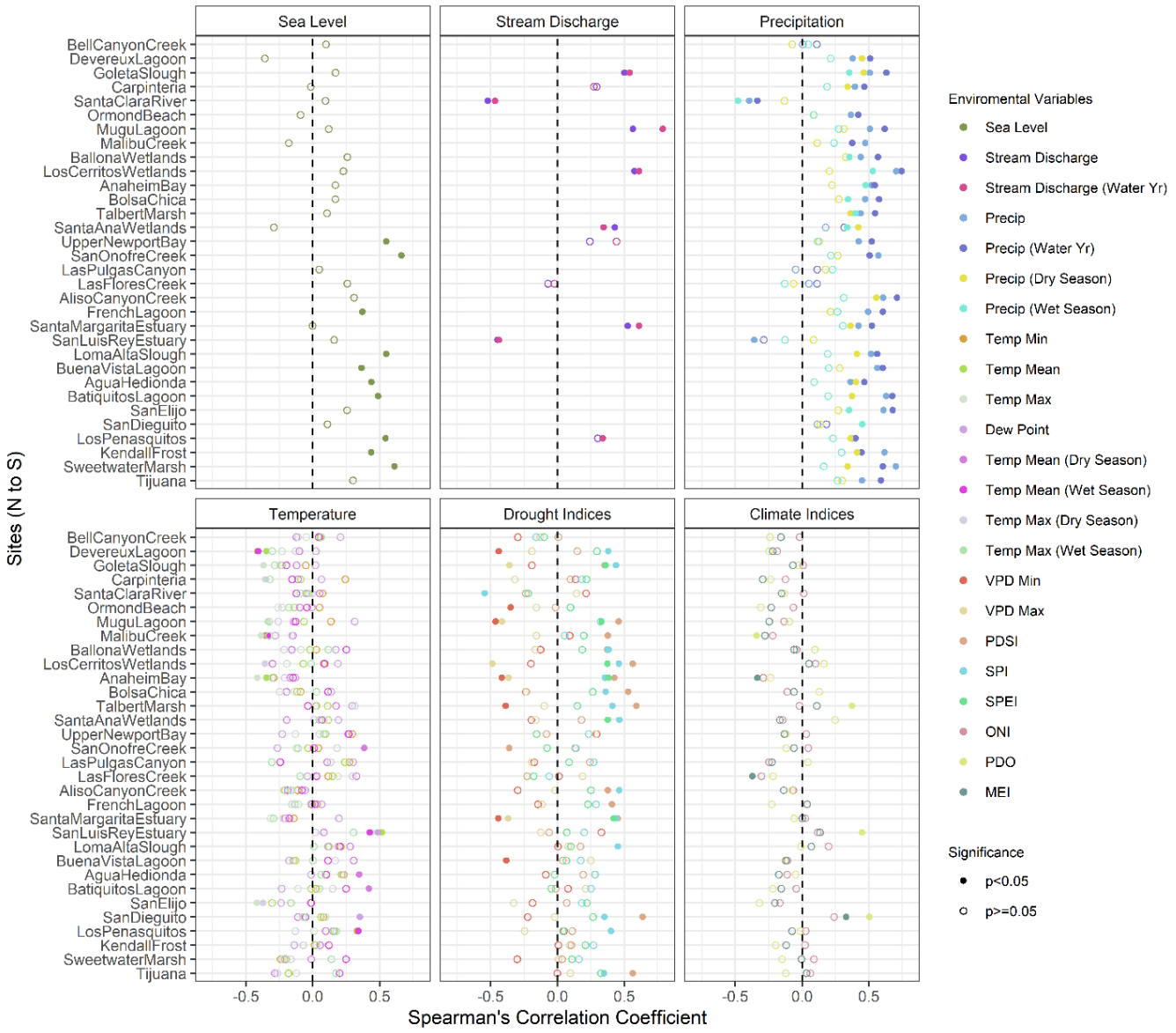


**Figure 4-6. Top explanatory variables per site determined from univariate regression analyses.**

### 4.4.4 The Influence of Regional Controls on Wetland Greenness Vary in Space and Time

Global regression analyses for the region indicate that there are spatial and temporal relationships among environmental factors and NDVI. Geographically and temporally weighted regressions explained regional variability in NDVI for the several models tested (Table 4-4). GTWR models that address spatial and temporal heterogeneity explained up 55% of the variation

in NDVI (AIC = -3854). The GTWR model that explained the highest variance in NDVI included environmental parameters of maximum temperature, water year precipitation, dew point temperature, sea level, and maximum vapor pressure deficit (Model 1; Table 4-4). Less complex models were also tested using combinations of the top performing variables within each environmental category and showed that the simpler models were also comparable to Model 1 in terms of explaining NDVI.

**Table 4-4. Comparison of multivariate models used to explain NDVI using geographically and temporally weighted regression (GTWR).**

| | | GTWR | |
|---|---|---|---|
| | **Model** | **$r^2$** | **AIC** |
| 1 | NDVI ~ $Temp_{max}$ + $PPT_{WaterYear}$ + $Temp_{DewPt}$ + SeaLevel + $VPD_{max}$ | 0.55 | -3854 |
| 2 | NDVI ~ $Temp_{max}$ + $PPT_{WaterYear}$ + $Temp_{mean}$ | 0.53 | -3836 |
| 3 | NDVI ~ $Temp_{max}$ + $PPT_{WaterYear}$ + $Temp_{DewPt}$ + SeaLevel | 0.52 | -3799 |
| 4 | NDVI ~ SeaLevel + $PPT_{WaterYear}$ + $Temp_{max}$ + $VPD_{max}$ + MEI | 0.51 | -3765 |
| 5 | NDVI ~ $Temp_{max}$ + $PPT_{WaterYear}$ | 0.47 | -3715 |
| 6 | NDVI ~ $Temp_{max}$ + $PPT_{WaterYear}$ + ONI | 0.45 | -3667 |
| 7 | NDVI ~ $Temp_{max}$ + MEI | 0.44 | -3657 |

## 4.5 Discussion

The majority of wetlands in the southern California region exhibited greening trends from 1984 – 2019. From the regional regression analysis, the two highly correlated environmental variables with wetland NDVI over this time period were found to be maximum annual temperature and total precipitation summed for the previous water year. We expected that regional controls to the health of southern California's wetlands would be impacted by water availability, namely precipitation and drought, which is typical of many other Mediterranean ecosystems worldwide (Allen, 2003). A study of tidal marshes in the Pacific Norwest, USA found that peak biomass was positively correlated to total annual precipitation and the timing of peak biomass was negatively correlated to average growing season temperature based on 31 years of data (Buffington et al.,

2018). This region is under similar high influence of ENSO, which causes intra-decadal variability in temperature in precipitation (Gershunov and Barnett, 1998). An example from Georgia, USA, also shows a positive, significant relationship between wetland aboveground biomass and river discharge, total precipitation, minimum temperature, and mean sea level over a 28-year period (O'Donnell and Schalles, 2016). In another region facing different environmental and human stressors, the wetlands of coastal Louisiana, USA, have been exhibiting longer growing seasons from 1984 – 2014 that are attributed mainly to increasing atmospheric $CO_2$, while areas of brackish and saline marshes have declined over the study period (Mo et al., 2019). Greening trends in southern California could reflect longer, amplified growing seasons caused by the interaction of warming temperatures and available water resources. Findings from these case studies emphasize that location plays an important role modelling wetland characteristics (Buffington et al., 2018), that long-term response can vary among wetland types within a larger wetland complex (Mo et al., 2019), and that wetland response can varied across seasons (O'Donnell and Schalles, 2016).

In our study of southern California's wetlands, spatial and temporal variability exists in the relationship among wetland greenness and environmental drivers. Results from GTWR regressions reveal the spatiotemporal characteristic of the correlations among wetland NDVI and environmental drivers that may be missed with global regression techniques. For example, the importance of maximum temperature was less evident in site-based regression but was identified as a top explanatory variable using PCA and step-wise comparison for AIC for GTWR models (Figure S4-3). Conversely, precipitation variables (annual sum, water year sum, and wet season sum) were the most significantly and highly correlated variables with NDVI for many sites (Figure 4-6), but only water-year precipitation was also identified in GTWR techniques as the second top explanatory variable. Temperature variables exhibited less local variability than precipitation

(Table 4-3), suggesting that temperature is a regional control while precipitation may be more variable at sub-regional scales. Surprisingly, mean annual dew point temperature was also identified as a top predictor variable in modelling NDVI using GTWR. To our knowledge, dew point temperature has not been specified previously as a control to wetland health, but dew point temperature was significantly positively correlated to other temperature variables (Table 4-2). Mean annual sea level and maximum annual vapor pressure deficit were the remaining environmental variables in the model with the highest explanatory power (Table 4-4). These variables were similar to maximum annual temperature in that they appear to have little local standard deviation compared to precipitation (Table 4-3).

Site-based inferences do help reveal spatial variability and patterns in the importance of environmental drivers, human influences, and other characteristics on long-term patterns in NDVI. Sea levels were significantly positively correlated with NDVI in several sites ranging in size and archetype in the south (Figure 4-6), where sea level rise rates are on average 0.93 mm $yr^{-1}$ higher than rates from NOAA stations to the north (https://tidesandcurrents.noaa.gov/sltrends). For sites with available USGS stream discharge data, six wetlands showed positive significant correlations with NDVI and two wetlands showed negative significant correlations. Differential response to streamflow may indicate two contrasting responses wetland plants have to rainfall, such as increased productivity from decreased soil salinity (Callaway and Sabraw, 1994; Zedler, 1983), or water stress from altered precipitation and streams flows (Zedler et al., 1986). Although stream discharge data were only available for a subset sites with USGS stream gauges (Figure S4-1), other archetypes throughout the region have associated rivers and creeks (SCWRP, 2018), and stream discharge would likely have an impact on these systems as well.

Trends in NDVI were not well explained by the amount of watershed development, restoration projects or site characteristics like size, habitat composition, or archetype classification (Figure 4-4). Wetland archetypes represent systems with similar form and structure that are expected to function similarly and respond to physical drivers and external stressors in a similar manner (Stein et al., 2019). However, each archetype is designed to represent a broad range in diversity of sites, and therefore responses may also be variable. This was true in using the archetype framework to predict future habitat response to SLR, where sites within archetypes displayed high variability in estimated wetland habitat loss (Doughty et al., 2018). Therefore, the diversity of intra-annual patterns in NDVI within archetypes, most notably in intermediate estuaries, is valid and highlights intra-annual phenology as another diverse quality of the wetlands in the southern California region. Five clusters of similar intra-annual patterns emerged based on the timing and magnitude of peak annual NDVI, which indicates variable phenological response of systems to different environmental factors. Therefore, there are not typical phenological patterns characteristic to certain archetypes, or a singular phenological model that describes all sites in the region. Intra-annual patterns in wetland NDVI may be less straightforward in this region's wetlands compared to other regions were large, vegetated wetland systems can be described by typical annual phenology curves (Mo et al., 2015).

Our work provides important insights into the spatial and temporal variability in drivers and responses in long-term greenness and health of coastal wetlands across a region. The freely available, historical datasets used as the foundation for this study can also aid investigations into other important patterns in southern California's wetlands and other regions with a diversity of wetlands. More work is needed to consider the full range of human impacts to wetland health, like eutrophication, dredging, and watershed management (Kennish, 2001) if long-term datasets are

available. In addition, satellite imagery can also aid in identifying pulse disturbances occurring from episodic events like fires and subsequently track recovery (Brown, 2019). These applications would be of interest to regional wetland management and adaptation efforts in monitoring impacts into the future using remotely sensed imagery.

### 4.6 References


Adam, E., Mutanga, O., Rugege, D., 2010. Multispectral and hyperspectral remote sensing for identification and mapping of wetland vegetation: A review. Wetl. Ecol. Manag. 18, 281–296.

Allen, H.D., 2003. Response of past and present Mediterranean ecosystems to environmental change. Prog. Phys. Geogr. 27, 359–377.

Barbier, E.B., Hacker, S.D., Kennedy, C.J., Koch, E.W., Stier, A.C., Silliman, B.R., 2011. The value of estuarine and coastal ecosystem services. Ecol. Monogr. 81, 169–193.

Bjørnstad, O.N., Falck, W., 2001. Nonparametric spatial covariance functions: Estimation and testing. Environ. Ecol. Stat. 8, 53–70.

Boesch, D.F., Field, J.C., Scavia (Eds), D., 2000. The Potential Consequences of Climate Variability and Change on Coastal Areas and Marine Resources: Report of the Coastal Areas and Marine Reseources Sector Team, U.S. National Assessment of the Potential Consequences of Climate Variability and Change, U., NOAA Coastal Ocean Program Decision Analysis Series No. #21. NOAA Coastal Ocean Program, Silver Spring, MD. 163 pp.

Borchert SM, Osland MJ, Enwright NM, Griffith KT. 2018. Coastal wetland adaptation to sea level rise: Quantifying potential for landward migration and coastal squeeze. J Appl Ecol. 55, 2876–2887.

Brooke, B., Lymburner, L., Lewis, A., 2017. Coastal dynamics of Northern Australia – Insights from the Landsat Data Cube. Remote Sens. Appl. Soc. Environ. 8, 94–98.

Brown, L.N., 2019. Multiple Stressors Influence Salt Marsh Recovery after a Spring Fire at Mugu Lagoon, CA. Wetlands. 40, 757–769.

Brunsdon, C., Fotheringham, A.S., Charlton, M.E., 1996. Geographically Weighted Regression: A Method for Exploring Spatial Nonstationarity. Geogr. Anal. 28, 407–414.

Buffington, K.J., Dugger, B.D., Thorne, K.M., 2018. Climate-related variation in plant peak biomass and growth phenology across Pacific Northwest tidal marshes. Estuar. Coast. Shelf Sci. 202, 212–221.

Bunting, P., Rosenqvist, A., Lucas, R.M., Rebelo, L.M., Hilarides, L., Thomas, N., Hardy, A., Itoh, T., Shimada, M., Finlayson, C.M., 2018. The global mangrove watch - A new 2010 global baseline of mangrove extent. Remote Sens. 10.

Byrd, K.B., Ballanti, L., Thomas, N., Nguyen, D., Holmquist, J.R., Simard, M., Windham-

Myers, L., 2018. A remote sensing-based model of tidal marsh aboveground carbon stocks for the conterminous United States. ISPRS J. Photogramm. Remote Sens. 139, 255–271.

Byrd, K.B., O'Connell, J.L., Di Tommaso, S., Kelly, M., 2014. Evaluation of sensor types and environmental controls on mapping biomass of coastal marsh emergent vegetation. Remote Sens. Environ. 149, 166–180.

Callaway, R.M., Sabraw, C.S., 1994. Effects of Variable Precipitation on the Structure and Diversity of A California Salt-Marsh Community. J. Veg. Sci. 5, 433–438.

Cavanaugh, K.C., Osland, M.J., Bardou, R., Hinojosa-Arango, G., López-Vivas, J.M., Parker, J.D., Rovai, A.S., 2018. Sensitivity of mangrove range limits to climate variability. Glob. Ecol. Biogeogr. 27, 925–935.

Chen, C., Liu, L.-M., 1993. Joint Estimation of Model Parameters and Outlier Effects in Time Series. J. Am. Stat. Assoc. 88, 284–297.

Crespo, R., 2007. Application of geographically weighted regression to a 19-year set of house price data in London to calibrate local hedonic price models. Proc. 9th Int. Conf. Geocomputation. Natl. Univ. Irel. Maynooth.

Daly, C., Halbleib, M., Smith, J.I., Gibson, W.P., Doggett, M.K., Taylor, G.H., Curtis, J., Pasteris, P.P., 2008. Physiographically sensitive mapping of climatological temperature and precipitation across the conterminous United States. Int. J. Climatol. 2011–2029.

Day, J.W., Christian, R.R., Boesch, D.M., Yáñez-Arancibia, A., Morris, J., Twilley, R.R., Naylor, L., Schaffner, L., Stevenson, C., 2008. Consequences of climate change on the ecogeomorphology of coastal wetlands. Estuaries and Coasts 31, 477–491.

Dettinger, M.D., Ralph, F.M., Das, T., Neiman, P.J., Cayan, D.R., 2011. Atmospheric Rivers, Floods and the Water Resources of California. Water 3, 445–478.

Doughty, C., Cavanaugh, K., 2019. Mapping Coastal Wetland Biomass from High Resolution Unmanned Aerial Vehicle (UAV) Imagery. Remote Sens. 11, 540.

Doughty, C.L., Ambrose, R.F., Okin, G.S., Cavanaugh, K.C., n.d. Characterizing spatial variability in coastal wetland biomass across multiple scales using UAV and satellite imagery. Remote Sens. Ecol. Conserv.

Doughty, C.L., Cavanaugh, K.C., Ambrose, R.F., Stein, E.D., 2018. Evaluating regional resiliency of coastal wetlands to sea level rise through hypsometry-based modeling. Glob. Chang. Biol. 25, 78–92.

Erwin, K.L., 2009. Wetlands and global climate change: The role of wetland restoration in a changing world. Wetl. Ecol. Manag. 17, 71–84.

Flood, N., 2014. Continuity of reflectance data between landsat-7 ETM+ and landsat-8 OLI, for both top-of-atmosphere and surface reflectance: A study in the australian landscape. Remote Sens. 6, 7952–7970.

Fotheringham, A.S., Crespo, R., Yao, J., 2015. Geographical and Temporal Weighted Regression (GTWR). Geogr. Anal. 47, 431–452.

Franklin, J., Serra-Diaz, J.M., Syphard, A.D., Regan, H.M., 2017. Big data for forecasting the

impacts of global change on plant communities. Glob. Ecol. Biogeogr. 26, 6–17.

Gedan KB, Silliman BR, Bertness MD., 2009. Centuries of Human-Driven Change in Salt Marsh Ecosystems. Ann Rev Mar Sci. 2009; 1:117–141.

Gershunov, A., Barnett, T.P., 1998. ENSO Influence on Intraseasonal Extreme Rainfall and Temperature Frequencies in the Contiguous United States: Observations and Model Results. J. Clim. 11, 1575–1586.

Giorgino, T., 2009. Computing and visualizing dynamic time warping alignments in R: The dtw package. J. Stat. Softw. 31, 1–24.

Gittman RK, Fodrie FJ, Popowich AM, Keller DA, Bruno JF, Currin CA, Peterson CH, Piehler MF., 2015. Engineering away our natural defenses: An analysis of shoreline hardening in the US. Front Ecol Environ. 13, 301–7.

Gollini, I., Lu, B., Charlton, M., Brunsdon, C., Harris, P., 2015. GWmodel : an R package for exploring spatial heterogeneity. J. Stat. Softw. 63, 1–50.

Goodman, A.C., Thorne, K.M., Buffington, K.J., Freeman, C.M., Janousek, C.N., 2018. El Niño Increases High-Tide Flooding in Tidal Wetlands Along the U.S. Pacific Coast. J. Geophys. Res. Biogeosciences 123, 3162–3177.

Gorelick, N., Hancher, M., Dixon, M., Ilyushchenko, S., Thau, D., Moore, R., 2017. Google Earth Engine: Planetary-scale geospatial analysis for everyone. Remote Sens. Environ. 202, 18–27.

Grossinger, R., Stein, E.D., Cayce, K., Askevoid, R., Dark, S., Whipple, A., 2011. Historical Wetlands of the Southern California Coast: An Atlas of US Coast Survey T-Sheets, 1851-1889, Wetlands.

Hartigan, J.A., Wong, M.A., 1979. Algorithm AS 136: A K-Means Clustering Algorithm Author ( s ): J . A . Hartigan and M . A . Wong Published by : Blackwell Publishing for the Royal Statistical Society Stable URL : http://www.jstor.org/stable/2346830. J. R. Stat. Soc. Ser. C (Applied Stat. 28, 100–108.

Hird, J.N., McDermid, G.J., 2009. Noise reduction of NDVI time series: An empirical comparison of selected techniques. Remote Sens. Environ. 113, 248–258.

Jacobs, D.K., Stein, E.D., Longcore, T., 2011. Classification of California Estuaries Based on Natural Closure Patterns: Templates for Restoration and Management Management, Southern California Coastal Water Research Project Technical Report 619.a.

Janousek, C.N., Buffington, K.J., Thorne, K.M., Guntenspergen, G.R., Takekawa, J.Y., Dugger, B.D., 2016. Potential effects of sea-level rise on plant productivity: Species-specific responses in northeast Pacific tidal marshes. Mar. Ecol. Prog. Ser. 548, 111–125.

Jiang, Z., Huete, A.R., Didan, K., Miura, T., 2008. Development of a two-band enhanced vegetation index without a blue band. Remote Sens. Environ. 112, 3833–3845.

Kauth, R.J., Thomas, G.S., 1976. The tasselled cap - A graphic description of the spectral-temporal development of agricultural crops as seen by Landsat. Proc. Symp. Mach. Process. Remote. Sensed Data, West Lafayette, Indiana, U.S.A, 29 June-1 July 1976 41–51.

Kearney, M.S., Rogers, A.S., Townshend, J.R.G., Rizzo, E., Stutzer, D., Stevenson, J.C., Sundborg, K., 2002. Landsat imagery shows decline of coastal marshes in Chesapeake and Delaware Bays. Eos, Trans. Am. Geophys. Union 83, 173.

Kelso, M.A., Wigginton, R.D., Grosholz, E.D., 2020. Nutrients mitigate the impacts of extreme drought on plant invasions. Ecology 101, 1–10.

Kennedy, R.E., Andréfouët, S., Cohen, W.B., Gómez, C., Griffiths, P., Hais, M., Healey, S.P., Helmer, E.H., Hostert, P., Lyons, M.B., Meigs, G.W., Pflugmacher, D., Phinn, S.R., Powell, S.L., Scarth, P., Sen, S., Schroeder, T.A., Schneider, A., Sonnenschein, R., Vogelmann, J.E., Wulder, M.A., Zhu, Z., 2014. Bringing an ecological view of change to Landsat-based remote sensing. Front. Ecol. Environ. 12, 339–346.

Kennish, M.J., 2001. Coastal Salt Marsh Systems in the U.S.: A Review of Anthropogenic Impacts. J. Coast. Res. 17, 731–748.

Klemas, V., 2013. Remote sensing of coastal wetland biomass: An overview. J. Coast. Res. 290, 1016–1028.

Langley, J.A., McKee, K.L., Cahoon, D.R., Cherry, J.A., Megonigal, J.P., 2009. Elevated CO2 stimulates marsh elevation gain, counterbalancing sea-level rise. Proc. Natl. Acad. Sci. U. S. A. 106, 6182–6186.

MacDonald, G.M., 2007. Severe and sustained drought in southern California and the West: Present conditions and insights from the past on causes and impacts. Quat. Int. 173–174, 87–100.

Mckee, K., Rogers, K., Saintilan, N., 2012. Global Change and the Function and Distribution of Wetlands, Global Change and the Function and Distribution of Wetlands.

Mishra, D.R., Ghosh, S., 2015. Using Moderate-Resolution Satellite Sensors for Monitoring the Biophysical Parameters and Phenology of Tidal Marshes. In: Remote Sensing of Wetlands: Applications and Advances. CRC Press, pp. 300–331.

Mo, Y., Kearney, M.S., Riter, J.C.A., Zhao, F., Tilley, D.R., 2018. Assessing biomass of diverse coastal marsh ecosystems using statistical and machine learning models. Int. J. Appl. Earth Obs. Geoinf. 68, 189–201.

Mo, Y., Kearney, M.S., Turner, R.E., 2019. Feedback of coastal marshes to climate change: Long-term phenological shifts. Ecol. Evol. 1–13.

Mo, Y., Momen, B., Kearney, M.S., 2015. Quantifying moderate resolution remote sensing phenology of Louisiana coastal marshes. Ecol. Modell. 312, 191–199.

Myers-Smith, I.H., Jeffrey T.K., Gareth K.P., Jarle W.B., Howard E.E., Jakob J.A., Christian J. et al., 2020. Complexity revealed in the greening of the Arctic. Nature Climate Change. 10, 106–117.

Mutanga, O., Skidmore, A.K., 2004. Narrow band vegetation indices overcome the saturation problem in biomass estimation. Int. J. Remote Sens. 25, 3999–4014.

Neumann B, Vafeidis AT, Zimmermann J, Nicholls RJ., 2015. Future coastal population growth and exposure to sea-level rise and coastal flooding - A global assessment. PLoS One. 10, e0118571.

Newton, A., Icely, J., Cristina, S., Perillo, G.M.E., Turner, R.E., Ashan, D., Cragg, S., Luo, Y., Tu, C., Li, Y., Zhang, H., Ramesh, R., Forbes, D.L., Solidoro, C., Béjaoui, B., Gao, S., Pastres, R., Kelsey, H., Taillie, D., Nhan, N., Brito, A.C., de Lima, R., Kuenzer, C., 2020. Anthropogenic, Direct Pressures on Coastal Wetlands. Front. Ecol. Evol. 8, 1–29.

O'Donnell, J.P.R., Schalles, J.F., 2016. Examination of abiotic drivers and their influence on Spartina alterniflora biomass over a twenty-eight year period using Landsat 5 TM satellite imagery of the Central Georgia Coast. Remote Sens. 8, 477-.

Osland, M.J., Enwright, N.M., Day, R.H., Gabler, C.A., Stagg, C.L., Grace, J.B., 2016. Beyond just sea-level rise: considering macroclimatic drivers within coastal wetland vulnerability assessments to climate change. Glob. Chang. Biol. 22, 1–11.

Pasquarella, V.J., Holden, C.E., Kaufman, L., Woodcock, C.E., 2016. From imagery to ecology: leveraging time series of all available Landsat observations to map and monitor ecosystem state and dynamics. Remote Sens. Ecol. Conserv. 2, 152–170.

Pohlert, T., 2020. trend: Non-Parametric Trend Tests and Change-Point Detection. R package version 1.1.2.

Rogers, K., Lymburner, L., Salum, R., Brooke, B.P., Woodroffe, C.D., 2017. Mapping of mangrove extent and zonation using high and low tide composites of Landsat data. Hydrobiologia 803, 49–68.

Rouse, J., Haas, R., Schell, J., Deering, D., 1974. Monitoring vegetation systems in the Great Plains with ERTS. NASA Spec. Publ. 351, 309.

Roy, D.P., Kovalskyy, V., Zhang, H.K., Vermote, E.F., Yan, L., Kumar, S.S., Egorov, A., 2016. Characterization of Landsat-7 to Landsat-8 reflective wavelength and normalized difference vegetation index continuity. Remote Sens. Environ. 185, 57–70.

Scavia, D., Field, J.C., Boesch, D.F., Buddemeier, R.W., Cayan, D.R., Fogarty, M., Harwell, M.A., Howarth, R.W., Reed, D.J., Royer, T.C., Sallenger, A.H., Titus, J.G., Town, C., Virginia, W., 2002. Climate Change Impacts on U. S. Coastal and Marine Ecosystems. Estuaries 25, 149–164.

Southern California Wetlands Recovery Project (SCWRP), 2018. Wetlands on the Edge: The Future of Southern California's Wetlands: Regional Strategy 2018 prepared by the Southern California Wetlands Recovery Project. California State Coastal Conservancy. Oakland, CA.

Sen, P.K., 1968. Estimates of the Regression Coefficient Based on Kendall's Tau. J. Am. Stat. Assoc. 63, 1379–1389.

Short, F.T., Kosten, S., Morgan, P.A., Malone, S., Moore, G.E., 2016. Impacts of climate change on submerged and emergent wetland plants. Aquat. Bot. 135, 3–17.

Stein, E.D., 2015. Development of Regional Coastal Wetland Archetypes.

Stein, E.D., Cayce, K., Salomon, M., Bram, D.L., Grossinger, R., Dark, S., 2014. Wetlands of the Southern California coast: Historical extent and change over time. South. Calif. Coast. Water Res. Proj. Tech. Rep. 826 1–50.

Stein, E.D., Doughty, C.L., Lowe, J., Cooper, M., Sloane, E.B., Bram, D.L., 2019. Establishing

Targets for Regional Coastal Wetland Restoration Planning Using Historical Ecology and Future Scenario Analysis: The Past, Present, Future Approach. Estuaries and Coasts.

Steyer, G.D., Couvillion, B.R., Barras, J.A., 2013. Monitoring vegetation response to episodic disturbance events by using multitemporal vegetation indices. J. Coast. Res. 63, 118–130.

Thorne, K., Macdonald, G., Guntenspergen, G., Ambrose, R., Buffington, K., Dugger, B., Freeman, C., Janousek, C., Brown, L., Rosencranz, J., Holmquist, J., Smol, J., Hargan, K., Takekawa, J., 2018. U. S. Pacific coastal wetland resilience and vulnerability to sea-level rise. Sci. Adv. 4, 1–11.

Thorne, K., MacDonald, G.M., Takekawa, J.Y., Ambrose, R.A., Barnard, P., Guntenspergen, G.R., Hall, A., Ganju, N., Janousek, C., Freeman, C., Brown, L., Buffington, K., Holmquist, J., Powelson, K., 2016. Climate change effects on tidal marshes along a latitudinal gradient in California. U.S. Geol. Surv. Open-File Rep. 2016-1125 75 p.

Vicente-Serrano, S.M., Beguería, S., López-Moreno, J.I., 2010. A multiscalar drought index sensitive to global warming: The standardized precipitation evapotranspiration index. J. Clim. 23, 1696–1718.

Vogelmann, J.E., Gallant, A.L., Shi, H., Zhu, Z., 2016. Perspectives on monitoring gradual change across the continuity of Landsat sensors using time-series data. Remote Sens. Environ. 185, 258–270.

Watson E.B., Raposa K.B., Carey J.C., Wigand C., Warren R.S., 2017. Anthropocene Survival of Southern New England's Salt Marshes. Estuaries and Coasts. 40:617–625.

Wells, N., Goddard, S., Hayes, M.J., 2004. A self-calibrating Palmer Drought Severity Index. J. Clim. 17, 2335–2351.

Wigginton, R.D., Kelso, M.A., Grosholz, E.D., 2020. Time-lagged impacts of extreme, multi-year drought on tidal salt marsh plant invasion. Ecosphere 11.

Wong, P.P., Losada, I.J., Gattuso, J.P., Hinkel, J., Khattabi, A., McInnes, K.L., Saito, Y., Sallenger, A., 2014. Coastal Systems and Low-Lying Areas. In: Field, C.B., Barros, V.R., Dokken, D.J., Mach, K.J., Mastrandrea, M.D., Bilir, T.E., Chatterjee, M., Ebi, K.L., Estrada, Y.O., Genova, R.C., Girma, B., Kissel, E.S., Levy, A.N., MacCracken, S., Mastrandrea, P.R., White, L.L. (Eds.), Climate Change 2014: Impacts, Adaptation, and Vulnerability. Report of the Intergovernmental Panel on Climate Change. Cambridge University Press, Cambridge, United Kingdom and New York, NY, USA., pp. 361–409.

Wu, W., Zhou, Y., Tian, B., 2017. Coastal wetlands facing climate change and anthropogenic activities: A remote sensing analysis and modelling application. Ocean Coast. Manag. 138, 1–10.

Wulder, M.A., Loveland, T.R., Roy, D.P., Crawford, C.J., Masek, J.G., Woodcock, C.E., Allen, R.G., Anderson, M.C., Belward, A.S., Cohen, W.B., Dwyer, J., Erb, A., Gao, F., Griffiths, P., Helder, D., Hermosilla, T., Hipple, J.D., Hostert, P., Hughes, M.J., Huntington, J., Johnson, D.M., Kennedy, R., Kilic, A., Li, Z., Lymburner, L., McCorkel, J., Pahlevan, N., Scambos, T.A., Schaaf, C., Schott, J.R., Sheng, Y., Storey, J., Vermote, E., Vogelmann, J., White, J.C., Wynne, R.H., Zhu, Z., 2019. Current status of Landsat program, science, and applications. Remote Sens. Environ. 225, 127–147.

Wulder, M.A., Masek, J.G., Cohen, W.B., Loveland, T.R., Woodcock, C.E., 2012. Opening the archive: How free data has enabled the science and monitoring promise of Landsat. Remote Sens. Environ. 122, 2–10.

Xue, J., Su, B., 2017. Significant remote sensing vegetation indices: a review of developments and applications. J. sensors Vol.2017, 17p.

Yang, L., Jin, S., Danielson, P., Homer, C., Gass, L., Bender, S.M., Case, A., Costello, C., Dewitz, J., Fry, J., Funk, M., Granneman, B., Liknes, G.C., Rigge, M., Xian, G., 2018. A new generation of the United States National Land Cover Database: Requirements, research priorities, design, and implementation strategies. ISPRS J. Photogramm. Remote Sens. 146, 108–123.

Zedler, J.B., 1983. Freshwater Impacts in Normally Hypersaline Marshes. Estuaries 6, 346–355.

Zedler, J.B., 1996. Coastal mitigation in Southern California: The need for a regional restoration strategy. Ecological Applications. 6, 84 – 93.

Zedler J.B., Callaway J.C., 1999. Tracking wetland restoration: Do mitigation sites follow desired trajectories? Restor Ecol. 7, 69–73.

Zedler, J.B., Covin, J., Nordby, C., Williams, P., Boland, J., 1986. Catastrophic events reveal the dynamic nature of salt-marsh vegetation in Southern California. Estuaries 9, 75–80.

Zhu, Z., Woodcock, C.E., 2012. Object-based cloud and cloud shadow detection in Landsat imagery. Remote Sens. Environ. 118, 83–94.

## 4.7 Supplemental Materials

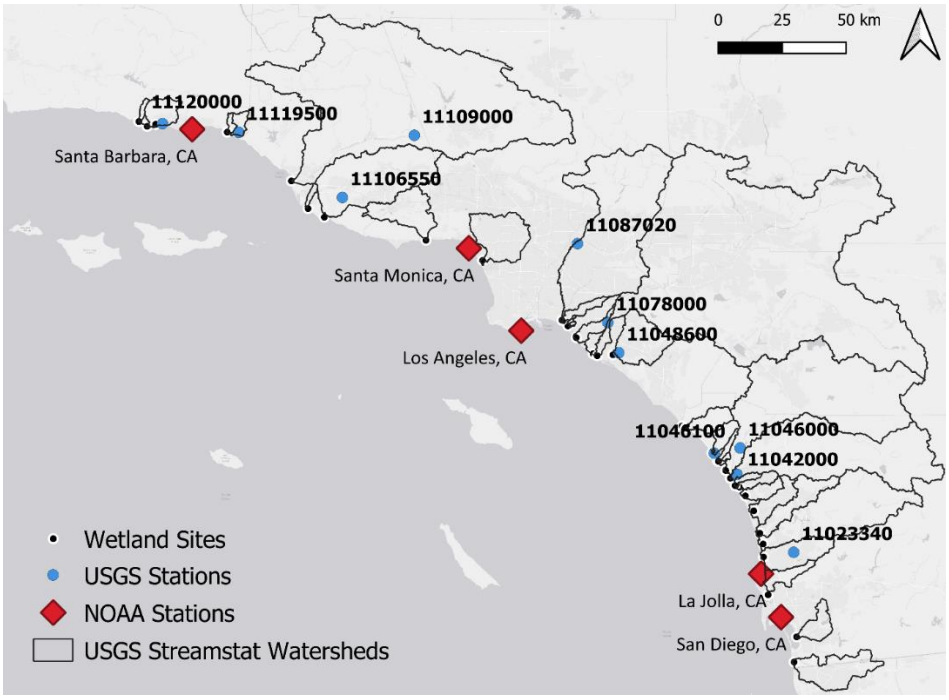


**Figure S4-1. Sources of environmental datasets on NOAA sea levels (red diamonds) and USGS stream discharge (blue circles).**

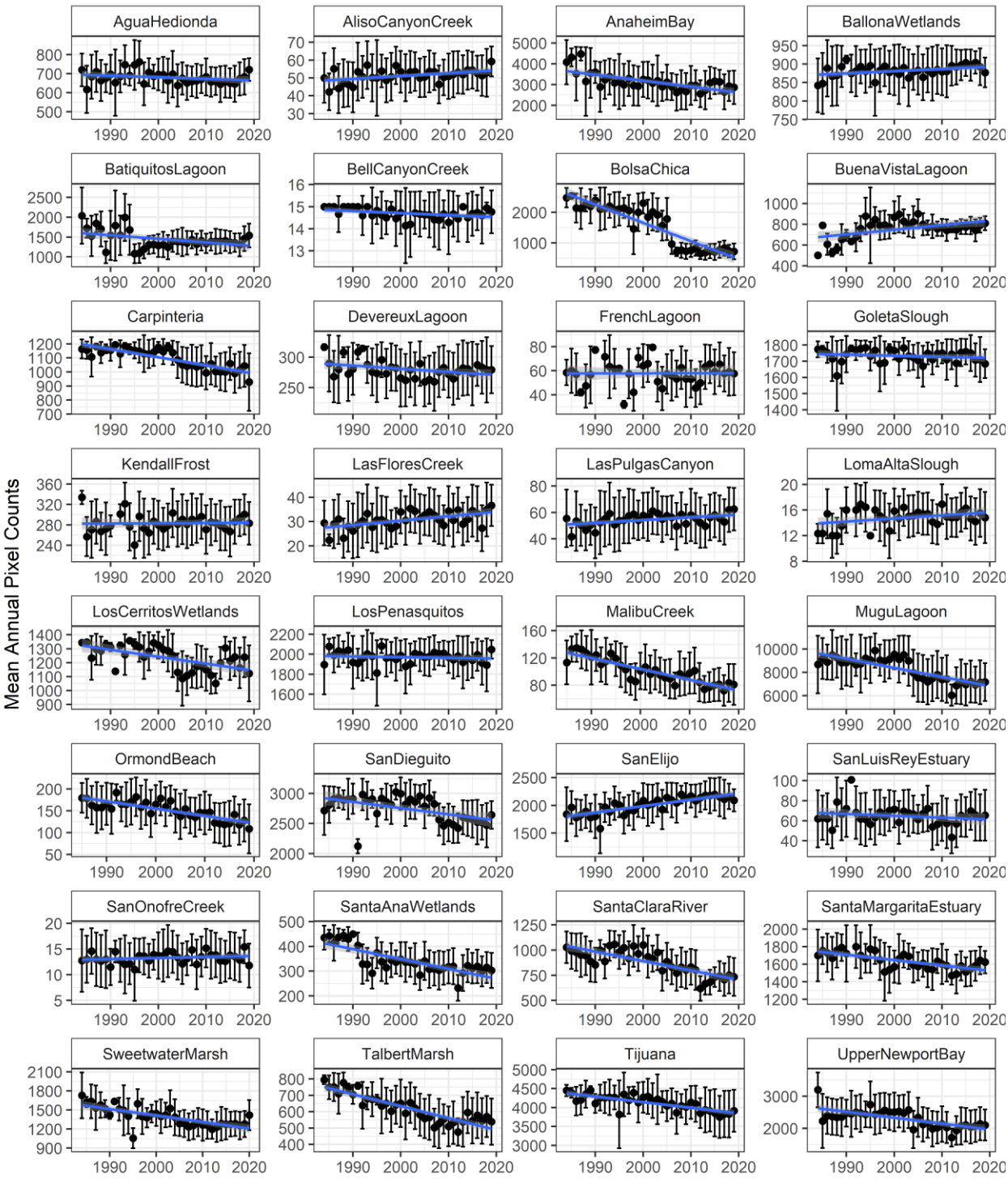


**Figure S4-2. Average count of clear land pixels per year (mean ± standard deviation). Simple linear trends over the study period are shown in blue. Note that y-axis varies per panel.**

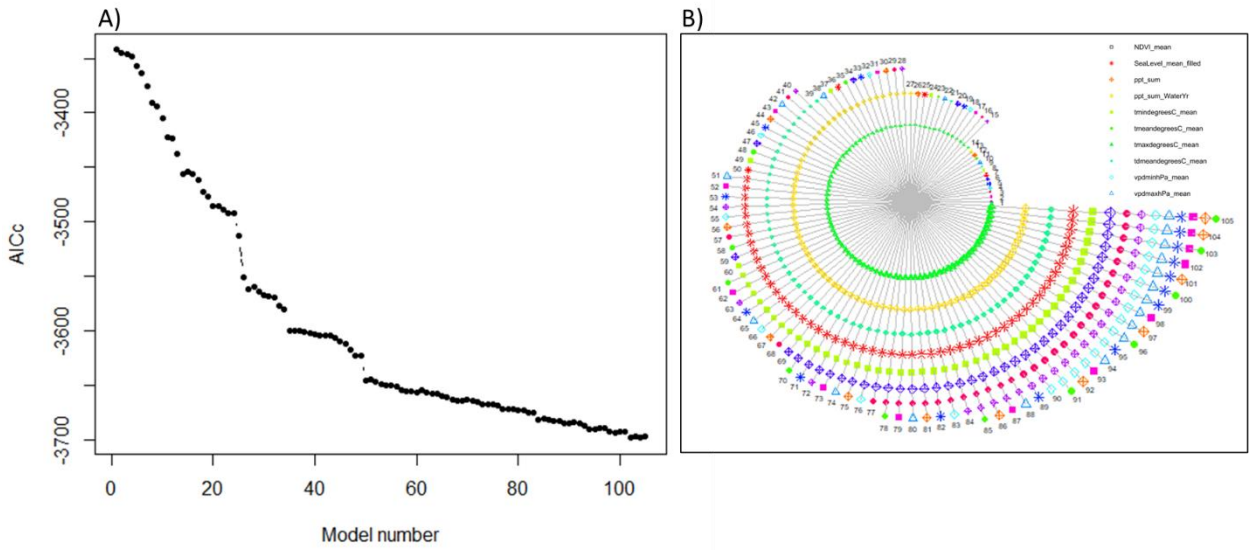


**Figure S4-3. GTWR model selection based on A) corrected AIC and B) a stepwise procedure ranking model variable combinations (colors, symbols, combinations joined by lines) by AIC.**

## CONCLUSION

In my dissertation, I pursued questions pertaining to wetland resilience and vulnerability in ecosystems that are at high risk of climate change and other human impacts. Despite being regarded as some of the world's most important ecosystems (Barbier et al. 2011), they have continually been lost and degraded globally and their fate remains uncertain (Spencer et al. 2016). This is also true of wetlands in the southern California region. Through the work conducted in this dissertation, I focus on uncovering the spatial and temporal variability at play in some of the wetland properties and processes that have controlled past responses, current status, and future predictions in light of environmental change.

Predictions of future regional response to sea level rise must account for all wetlands in a region regardless of size, and despite data availability. This is essential for seeing a full picture of regional vulnerability that also accounts for site-based estimates of habitat change and loss (Doughty et al. 2019). I focus on site-based measures so that the drivers investigated will be catered to ecology and function specific to sites, and so that habitat response is viewed at the appropriate scales for coordinated regional management efforts.

For a more detailed look at the wetland plant features that will ultimately contribute to resilience, I developed and tested a UAV approach to remotely estimating aboveground biomass. I used UAVs to map seasonal biomass in a single marsh in southern California and found that UAVs can provide high resolution insights to aboveground biomass, but that models were influenced significantly by season (Doughty and Cavanaugh 2019). To expand upon this work, I then applied the UAV approach to three additional wetlands in the region and tested UAV imagery verses Landsat imagery in how well they are able to estimate end-of-season aboveground biomass and detect ecologically important spatial patterns in wetland vegetation (Doughty et al., *submitted*).

While the resolutions of each imagery type make them suitable for investigating different ecological patterns, the high-resolution imagery provided by UAVs revealed what Landsat could not in the relatively small and constricted wetlands of southern California. Therefore, UAVs could be an essential tool for remotely quantifying aboveground biomass and provide important insights into indicators of wetland health.

Finally, I capitalized on decade's worth of Landsat satellite imagery and environmental conditions to characterize recent patterns in wetland greenness and uncover how greenness is related to drivers like temperature and precipitation. Given everything we now know about southern California's wetlands, it is not surprising that past responses to environmental change have also been highly spatially and temporally variable among unique wetlands sites in this region. However, overall trends suggest that the majority of wetlands are greening, but more work must be done to uncouple the human and climate interactions at play in the southern California region. The high spatial and temporal variability inherent to the past, present, and future of southern California's wetlands is yet another challenge to ensuring these ecosystems are preserved in the future.

**References**

Barbier, Edward B, Sally D Hacker, Chris J Kennedy, Evamaria W Koch, Adrian C Stier, and Brian R Silliman. 2011. The value of estuarine and coastal ecosystem services. *Ecological Monographs* 81: 169–193.

Doughty, Cheryl, and Kyle Cavanaugh. 2019. Mapping Coastal Wetland Biomass from High Resolution Unmanned Aerial Vehicle (UAV) Imagery. *Remote Sensing* 11: 540. https://doi.org/10.3390/rs11050540.

Doughty, Cheryl L., Richard F. Ambrose, Gregory S. Okin, and Kyle C. Cavanaugh. Characterizing spatial variability in coastal wetland biomass across multiple scales using UAV and satellite imagery. *Remote Sensing in Ecology and Conservation*.

Doughty, Cheryl L., Kyle C. Cavanaugh, Richard F. Ambrose, and Eric D. Stein. 2019. Evaluating regional resiliency of coastal wetlands to sea level rise through hypsometry-

based modeling. *Global Change Biology* 25: 78–92. https://doi.org/10.1111/gcb.14429.

Spencer, Thomas, Mark Schürch, Robert J. Nicholls, Jochen Hinkel, Daniel Lincke, A.T. T. Vafeidis, Ruth Reef, et al. 2016. Global coastal wetland change under sea-level rise and related stresses: The DIVA Wetland Change Model. *Global and Planetary Change* 139. Elsevier B.V.: 15–30. https://doi.org/10.1016/j.gloplacha.2015.12.018.